# Resolution and Calibration Studies based on measured Hybrid Data of the Pierre Auger Observatory

Nicole Krohm

# Diplomarbeit

Fachbereich Physik
Universität Wuppertal

Betreuender Professor: Prof. Karl-Heinz Kampert
Zweitkorrektor: Prof. Markus Risse (Uni Siegen)

# Zusammenfassung

Das übergeordnete Thema dieser Arbeit ist es, einen Beitrag zum Verständnis der Detektoren und ihres systematischen Einflusses auf die Energierekonstruktion, sowie dem Verständnis der statistischen und systematischen Rekonstruktionsunsicherheiten zu leisten.

Ausgedehnte Luftschauer von Milliarden unsichtbarer, hochenergetischer Teilchen durchdringen uns ständig, ohne dass wir sie wahrnehmen. Die Existenz der sogenannten *Kosmischen Strahlung* wurde 1912 von Victor F. Hess enthüllt. Die grundsätzlichen Fragen zur Natur der kosmischen Strahlung sind nach fast 100 Jahren immer noch dieselben:

- Woraus besteht die Strahlung?

- Woher kommt sie?

- Wie wird sie beschleunigt?

- Wie genau läuft die Propagation von der Quelle zur Erde ab?

Während Messungen mit Ballon- oder Satelliten-Experimenten eine direkte Detektion der kosmischen Strahlung mit niedrigen oder mittleren Energien ermöglichen, werfen höchstenergetische Energiebereich der kosmischen Strahlung (UHECR genannt) weiterhin viele Fragen auf. Dies hat unter anderem den Grund, dass mit wachsender Energie der Teilchenfluss kosmischer Strahlung immer geringer wird. Die geringe Wahrscheinlichkeit, höchstenergetische Primärteilchen zu detektieren, macht eine andere Messstrategie nötig: Indirekte Messungen, die auf den ausgedehnten Teilchenschauern (EAS genannt) basieren, die von Primärteilchen durch Wechselwirkungen mit der Atmosphäre erzeugt werden. Ein Experiment, welches den ultra-hochenergetischen Bereich der kosmischen Strahlung indirekt misst, ist das Pierre Auger Observatorium. Es umfasst eine Fläche von ungefähr 3000 km$^2$ in der argentinischen Pampa Amarilla. Eine Besonderheit des Observatoriums ist die zu Grunde liegende Hybrid-Messanordnung von 27 Fluoreszenzteleskopen (FD) und etwa 1660 Wasser-Cherenkov-Detektoren (SD). In klaren, mondlosen Nächten messen die beiden komplementären Detektorsysteme die Luftschauer gleichzeitig. Ein wesentlicher Vorteil von Hybridmessungen sind simulationsunabhängige Kreuzkalibrationen beider Systeme. Während der restlichen Zeit werden ausschließlich SD-Messungen durchgeführt. Der erste Cherenkov-Detektor wurde 2002 aufgestellt und im Juni 2008 wurde die Konstruktion des gesamten Detektorfeldes abgeschlossen. Die Hybrid-Datennahme[1] wurde 2004 aufgenommen und das erste Quadrupol[2]-Ereignis am 21. Mai 2007 gemessen. Jedes Detektorsystem misst Signalstärken und schreibt darüber hinaus GPS Zeitstempel und die geographischen Koordinaten der Detektoren mit. Für Hybrid-Messungen liegen die entsprechenden Messdaten für beide Detektorsysteme vor. Darüber hinaus werden die atmosphärischen Bedingungen gemessen, um den Einfluss der Atmosphäre auf die Messung zu korrigieren. Anhand dieser Informationen werden schließlich die Geometrie und Energie der Ereignisse sukzessive rekonstruiert.

In jedem Experiment ist es unumgänglich, die Messgrößen zusammen mit den statistischen und systematischen Unsicherheiten anzugeben, da die Resultate sonst nicht aussagekräftig sind. Üblicherweise werden mit Hilfe von Simulationen die Unsicherheiten abgeschätzt. Diese Methode

---

[1]Hybrid bedeutet, dass ein Ereignis von mindestens einem Teleskop und einem Cherenkov-Detektor gleichzeitig gemessen worden ist.

[2]Quadrupol heißt, dass ein Ereignis von allen vier Teleskopstationen gleichzeitig gemessen worden ist.

bietet den Vorteil, dass auch für sehr spezielle und beschränkte Datensätze eine große Statistik simuliert werden kann. Allerdings sind die Ergebnisse nicht unabhängig von den entsprechenden Simulationen. Zudem können die Ergebnisse keine Detektorfehler aufzeigen. Sie geben Aufschluss über statistische und systematische, modell- und simulationsabhängige Unsicherheiten. Da es mittlerweile eine hinreichende Menge an hochqualitativen Hybrid- und Mehrteleskop-Messdaten für systematische Studien gibt, ist es Ziel dieser Arbeit, die Rekonstruktionsgenauigkeit allein auf der Basis von Messdaten zu untersuchen. Mit dieser Methode ist es möglich, Detektorfehler in der Gestalt von beispielsweise fehlerhaften Messperioden, fehlerhaften Verkabelungen der Kamera-Pixel oder zeitlichen Trends in der Skala der Messgrößen aufzudecken. Der Einfluss dieser Unsicherheiten und Fehler auf die Rekonstruktion einzelner Größen kann anhand des Auflösevermögens dieser Größen untersucht werden. Ein wichtige Daten-Untergruppe für die experimentelle Bestimmung des Auflösevermögens von FD- oder Hybrid-rekonstruierten Messgrößen sind Mehrteleskop-Ereignisse. Ein Nachteil dieser Methode sind Verfälschungen der Ergebnisse durch stark beschränkte Datensätze und damit verbundene Einschränkungen des betrachteten Bereichs verschiedener Größen.

In dieser Arbeit werden Analysen zur Genauigkeit der Rekonstruktion der Schauerrichtung und deren zeitlicher Konstanz, zur zeitlichen Konstanz der Energiekalibration zwischen beiden Detektorsystemen und zur relativen Unsicherheit der Energiemessung aufgrund eines statistischen und systematischen Rekonstruktionsfehlers vorgestellt, die auf Golden Hybrid[3]- und Mehrteleskop-Messdaten basieren. Die Reihenfolge der Darstellung folgt der Reihenfolge der Datenrekonstruktionen. Zunächst wird eine Analyse der zeitlichen Entwicklung der Winkelauflösung und eine Abschätzung der Hybrid- und SD-Winkelauflösung anhand von Golden Hybrid Mehrteleskop-Messdaten erläutert. Darüber hinaus wird ein erster Ansatz zur Analyse der Rekonstruktionsgenauigkeit des Aufftreffpunktes der Schauerachse auf dem Boden vorgestellt. Die Genauigkeit der Rekonstruktion der Schauerachse hinsichtlich des Winkels und Auftreffpunktes ist von großer Bedeutung für die Genauigkeit der Analyse von Korrelationen zwischen rekonstruierter Schauerrichtung und Quell-Kandidaten der kosmischen Strahlung. Unter Verwendung von Golden Hybrid-Messdaten wird die SD-Energieskala mit der FD-Energieskala unabhängig von Simulationen geeicht. Die zeitliche Konstanz dieser Energiekalibration ist das Thema eines weiteren Kapitels. Eine Fehlabschätzung der Energie hätte einen starken Einfluss auf Messungen des Flusses kosmischer Strahlung. Zuletzt werden eine Analyse verschiedener Abhängigkeiten der Energieauflösung aufgrund der statistischen und systematischen Energie-Rekonstruktionunsicherheit und eine Bewertung der Abschätzung der Energieunsicherheit vorgestellt.

---

[3]Golden Hybrid bedeutet eine Hybrid-Rekonstruktion zusammen mit einer vollständigen, unabhängigen SD-Rekonstruktion.

# Contents

# Chapter 1

# Introduction

The overall aim of this thesis is to provide further information that help to understand
the detector and its systematic influence on the event reconstruction, as well as the un-
derstanding of statistical and systematic reconstruction uncertainties.
Extensive showers of millions of high energy particles strike the earth constantly while we
can neither see nor feel them. Cosmic rays (CR) were discovered by Victor F. Hess 1912.
The basic questions today are still the same as 100 years before, such as

- What is this radiation made of?

- Where does it come from?

- How is it accelerated?

- What happens during its propagation from the source to the earth?

Cosmic rays of low and moderate energies can be measured directly using balloon- or
satellite-experiments. The low flux of ultrahigh energy cosmic rays (UHECR) makes it
necessary to detect the primary particles indirectly by measuring the extensive air showers
(EAS) they produce when they strike the atmosphere. Chapter 3 outlines the knowledge
we have so far about CR. One experiment that deals with the ultra-high energy range
of CR is the Pierre Auger Observatory in Argentina. Covering an area of 3000 km$^2$ in
the Pampa Amarilla, it measures UHECR indirectly. A special feature of the observatory
is its hybrid detection technique, using 27 fluorescence telescopes (FD) and 1660 surface
detectors (SD). In clear, moonless nights both detector systems measure the air showers
simultaneously. A clear advantage of Hybrid measurements are simulation-independent
cross-calibrations between the complementary detector systems. All day only the SD
are in operation. Chapter 4 describes the observatory. The first surface detector was
deployed in 2002 and the construction of the whole array was finished in June 2008. Hy-
brid data have been taken since 2004 and the first quadrupole[1] event has been detected

---

[1]Quadrupole means that the event has been detected by all four telescope stations simultaneously.

on May 21st, 2007. Each detector system measures signal strengths and, in order to reconstruct the shower geometry, it records GPS timestamps and the geographical detector coordinates. Operating in the hybrid mode, those information are available for both detector systems. Moreover, the atmospheric conditions are recorded. Based on these information the events are reconstructed from the measured data. In general a reconstruction means performing a step-by-step procedure to reconstruct the shower geometry and the shower energy. Chapter 5 describes the reconstuctions for the different operation modes. The software used for the reconstruction is described in Section 5.5.

In every experiment it is indispensable to know the uncertainties and the accuracy of the measurements and to state them together with the results. Without this evaluation the results are meaningless. Usually estimations on these quantities are made using simulations. A clear advantage of simulations is that even for very special and restricted sets of events high statistics can be produced. But the results depend on these simulations and, furthermore, cannot shed light on detector errors. They yield statistical and systematic, model-specific uncertainties. As there is a sufficient amount of high-quality Hybrid and multi-eye[2] data available for systematic studies, after more than five years of data-taking, the topic of this thesis is an analysis of the reconstruction accuracy by means of statistical and systematic uncertainties related to experimental data only. Beyond those uncertainties, it is possible to discover detector errors, i.e. in the form of bad periods, of miscabled pixels of the telescope cameras or in the form of shifts of the scales of measured quantities as a function of time. The influence of those uncertainties and errors on reconstructed quantities can be analysed by studying their resolution. Multi-eye events are essential for the estimation of resolutions related to the Hybrid- or FD-reconstuction uncertainty. A disadvantage of using only experimental data is that restricted datasets have several biases, i.e. an energy or a distance bias. Before the analyses are presented, a short overview over the evaluation of fit results is given in Chapter 6.

In this thesis, analyses of the reconstruction acuracy of the shower axis and its variation with time, of the variation of the energy calibration between both detector systems with time and of the relative uncertainties of the energy measurement due to a statistical and systematic reconstruction error are presented (Chapters 7-9). These analyses are based on measured Golden[3] Hybrid data. The order of the presentation follows the order of the reconstruction-chain. Chapter 7 contains studies of the variation of the angular resolution with time and an estimation of the Hybrid and SD angular resolution based on Golden Hybrid multi-eye data. Moreover, a first approach to estimate the reconstruction accuracy of the shower axis intersection point with the ground is presented. The accuracy of the shower axis has a strong effect on the accuracy of analyses of the correlations between the reconstructed shower direction and UHECR source candidates. Using Golden Hybrid data, the SD energy scale is calibrated by the FD energy scale, providing a simulation-independent calibration. The variation of the energy calibration with time is topic of Chapter 8. Chapter 9 presents studies of dependences of the energy

---

[2]Multi-eye events have been detected simultaneously by two or more telescopes.
[3]Golden Hybrid means a Hybrid reconstruction together with a full, independent SD reconstruction.

resolution due to a statistical and systematic reconstruction error and an evaluation of the estimation of the SD and FD energy uncertainty.

# Chapter 2

# Energy and Length Scale

The energy in the context of particle physics is commonly expressed in units of electron volts (eV). One electron volt is defined as the energy that a particle with a charge of 1 e gains covering a distance of 1 m in a vacuum, passing through a potential difference of 1 V:

$$1 \text{ eV} \doteq 1.602 \cdot 10^{-19} \text{ J}$$

The distance between two objects in the context of astrophysics is commonly given in astronomical units (au) or parallax seconds (parsec). One astronomical unit is defined as the mean distance between earth and sun. From a distance of one parallax second, one astronomical unit covers an angle of one arc second (1").

$$1 \text{ au} \doteq 149.6 \cdot 10^9 \text{ m}$$

$$1 \text{ parsec} \doteq \frac{1 \text{ au}}{\tan 1''} = 206264.806 \text{ au} = 30.857 \cdot 10^{15} \text{ m}$$

The magnitudes of these scales are expressed in terms of:

- Kilo (k) $= 10^3$

- Mega (M) $= 10^6$

- Giga (G) $= 10^9$

- Tera (T) $= 10^{12}$

- Peta (P) $= 10^{15}$

- Exa (E) $= 10^{18}$

# Chapter 3

# Cosmic Rays

Today we know that cosmic rays (CR) are highly energetic, ionized nuclei of all elements known from the periodic system, entering the earth's atmosphere from above. But it was a long way to come to this and further knowledge. The following historical overview is mainly based on [2].

A crucial day was August 7, 1912 when the Austrian physicist Viktor F. Hess started a remarkable flight with a hydrogen-filled balloon. It was the last flight of a series of seven flights. He ascended up to over 5 km, equipped with three hermetically sealed electroscopes. In those days electroscopes, also called "Wulf radiation apparatuses", were standard devices for measuring ionizing radiation [4]. Hess wanted to show a discharge of the electroscopes with increasing altitudes due to the reduction of radioactive substances in the earth, which was a common explanation of the appearing spontaneus ionization at that time. In the end he made a perplexing finding: The first 1000 m showed an expected discharge. But from that point on the ionization increased continually and above approximately 3 km exceeded the ionization on the ground. These results were observed simultaneously in all three electroscopes.

Hess published his results in the same year [5] and suggested a powerful and penetrating radiation, entering the earth's atmosphere from above. He discovered what the American physicist Robert Millikan called *cosmic rays* later on. In 1936, Hess was awarded the Nobel Price for this discovery, sharing it with Carl D. Anderson who had discovered the positron. This nobel price, besides, is one of many indications for the close and permanent connection between particle physics and astroparticle physics. In the aftermath, Werner Kohlhörster confirmed an increasing ionization rate in further balloon flights up to altitudes of 9 km [6].

Four basic questions arised with the discovery of CR:

- What is this radiation made of?

- Where does it come from?

- How is it accelerated?

- What happens during its propagation from the source to the earth?

7

In the following decades several experiments unveiled the nature of CR to some extent. Almost 80 years ago, Walther Bothe and Werner Kohlhörster analysed the absorption characteristics of CR indicating a corpuscular nature [7]. As J. Clay observed a dependence of the intensity of CR on the magnetic latitude, a large fraction of the CR must be charged particles [8]. During the following decade, further coincidence measurements at ground level (Werner Kohlhörster, [9]) and in 3500 m (Pierre Auger, [10]) showed that the observed CR particles are not primary particles but more or less extensive air showers that have been initiated in the atmosphere. This poses a big experimental challenge: How can we gain knowledge about the primary particles as they burst into millions of fragments after striking the earth's atmosphere?

The general underlying concepts of the detection methods emerging since 1940 can be split up into direct measurements above the atmosphere and indirect measurements on the ground. First direct measurements were performed using balloons that ascended up into the stratosphere, equipped with cloud chambers and photographic plates. They yielded information about the chemical composition and the velocity of CR: The posivitely charged primary particles turned out to be mainly protons [11], but even various heavier, fully ionized nuclei of the periodic table were detected. Furthermore, the velocity of CR was measured to be close to light velocity [12]. Until today various balloon- and satellite-experiments provided important knowledge about the composition of CR up to energies of several PeV, just to name some of them ([13, 14]): AMS, ATIC, BESS, CAPRICE, HEAT, ISOMAX, JACEE, RUNJOB.

For the low and medium energy range direct detection methods worked and still work fine, but for energies above several PeV the energy spectrum of CR, first measured in the 1940s using a ground detector, shows that the flux of the highest energetic particles is too low for direct measurements due to their small detection areas. Thus, for high energies ground detectors become essential. Technical developments provided scintillation counters and Cherenkov detectors that are still used for indirect measurements today. A series of air shower experiments was started with the air shower array at Volcano Ranch [15] in the 1960s, followed by SUGAR [16], Haverah Park [17], Yakutsk [18] and AGASA [19]. The detection areas increased from one experiment to another.

In 1981 an experiment called Fly's eye was started, applying a completely new detection method that utilizes the atmosphere as a calorimeter and measures the fluorescence light produced by air showers in the atmosphere. With Fly's Eye a basement for hybrid ground detectors with two complementary detector systems was built. In 1992 Jim Cronin and Alan Watson first proposed the hybrid detector Pierre Auger Observatory that was inaugurated 16 years later. The name was chosen after Pierre Auger who discovered the existence of air showers in 1938.

A big challenge concerning indirect measurements is the reconstruction of the primary particle type together with its kinetic conditions (energy, direction). Today the features of the energy spectrum, such as the *knee* (first observation 1958 [21]), a possible *second knee* (suggested in [38]), the *ankle* (first observation 1980 [22]) and the *GZK-cutoff* (predicted 1966 [23], confirmed 2007 [24]), combined with the knowledge about the composition serve as key observables to test different source and acceleration models of the

high energy range. Unfortunately, measurements of these observables are complicated by their strong dependance on hadronic interaction models. Another method to find possible UHECR sources is analysing the correlations between the reconstructed directions of the highest energetic CR with catalogues of various galactic objects (i.e. the catalogue of quasars and active nuclei by Veron-Cetty and Veron [25]). This last method is possible because of a decreasing effect of magnetic deviations for energies above $10^{19}$ eV.

While the last century brought a lot of progress in the understanding of the low and moderate energy range based on direct measurements, UHECR remain comparatively mysterious. The following paragraphs outline the status of our knowledge about UHECR at present in an order tracing back the propagation of cosmic rays, for we have to understand the closest (i.p. hadronic interactions in the atmosphere) to reconstruct the farthest precisely. The focussed ultra-high energy range reaches from $10^{18}$ eV to more than $10^{20}$ eV.

## 3.1   Extensive Air Showers

Cosmic ray particles strike the earth's atmosphere and initiate extensive air showers (EAS) of secondary particles cascading down to the ground with nearly light velocity. The principal EAS cascade process is sketched in Fig. 3.1.

If the primary cosmic ray particle is a nucleon or a nucleus, the first interaction in the atmosphere is a hadronic interaction with mainly nitrogen molecules ($N_2$) that are predominant in air with more than 75%. This interaction produces mostly charged or neutral pions, kaons and nucleons. Rapid decays of neutral pions ($\pi^0$) feed the electromagnetic shower component that dominates the shower. Charged pions ($\pi^\pm$) and kaons ($K^\pm$) reinteract with air nuclei or decay into muons. For photon-, electron- or positron-induced showers the muonic and hadronic components are almost negligible. We are obviously dealing with three shower components that evolve differently through the atmosphere:

- *Hadronic component*,
  consisting of nuclei, baryons (i.e. protons and neutrons) and mesons (i.e. pions and kaons).

- *Muonic component*,
  feeded by decays of charged mesons.

- *Electromagnetic component*,
  consisting of photons, electrons and positrons.

Positrons will not be treated separately from now on.

All secondary particles scatter away from the shower axis, but to a different extent. Muons perform much less scattering than electrons or photons. Moreover, the earlier a paricle is initiated during the shower evolution, the further from the shower axis it will arive. The showerfront itself resembles a cone.

Although muons are unstable with typical lifetimes of $\tau_\mu \approx 2.2$ $\mu$s, most of them reach
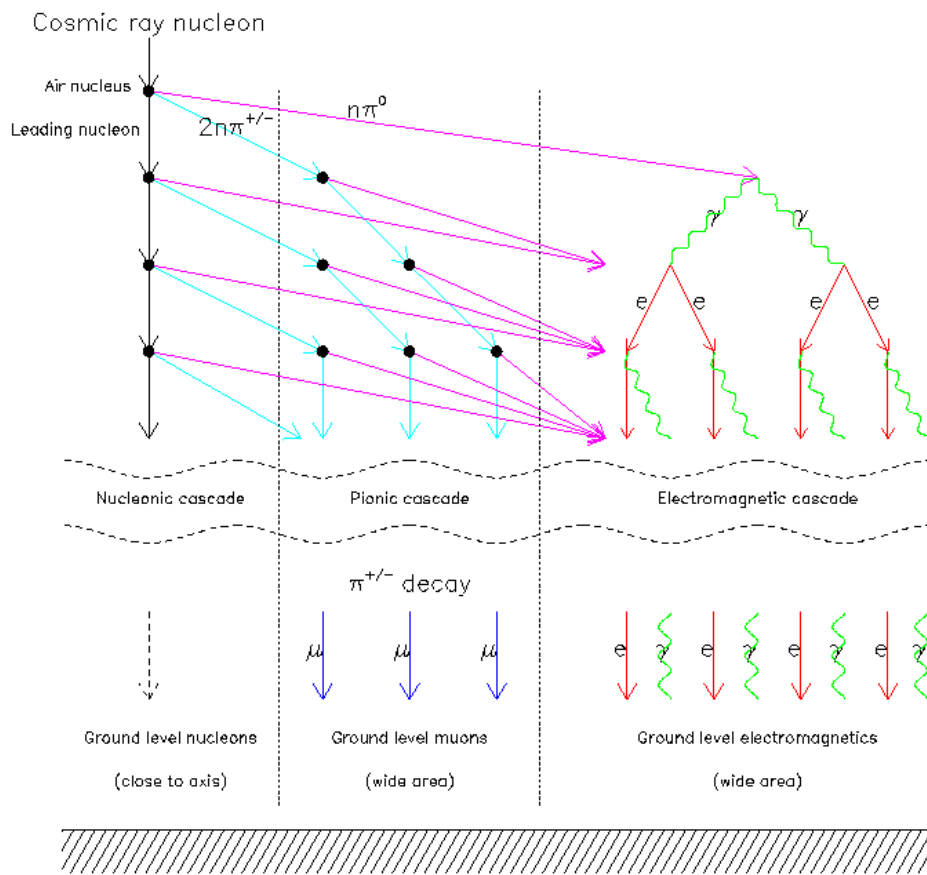
**Figure 3.1:** Simplified diagram of the principal EAS cascade process and the shower components, assuming an incident primary nucleon (from [3]).
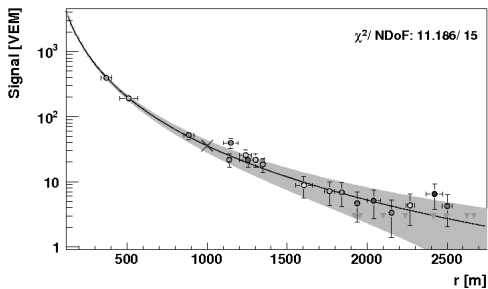
**Figure 3.2:** Example lateral density function (LDF) measured by the surface detector array.
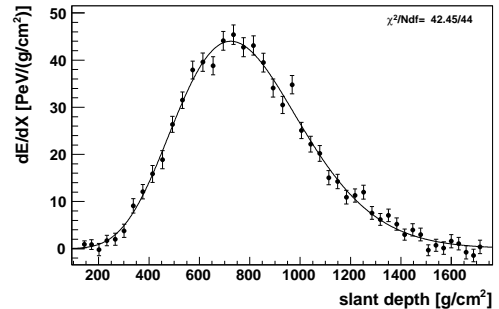


**Figure 3.3:** Example longitudinal shower profile measured by a fluorecence telescope.

the ground due to a relativistic time dilatation.

After this brief description of EAS the detectors come into play. The Pierre Auger Observatory uses fluorescence telescopes (FD) and surface detectors (SD). It measures a shower as a spot moving along the shower axis, producing near-UV light and particles. The SD array measures the charged particles and the relative timing of the shower arriving at the triggered tanks. The cameras of the fluorescence telescopes consist of a matrix of photomultiplier tubes (PMT). They perform a calorimetric measurement of the fluorescence light emitted during the shower development in the atmosphere, resulting in a quick series of triggered PMT that form a trace. Various data reconstructions can be performed, based on the signal strengths, the relative timing and the coordinates of the triggered detectors. A detailed description of the Pierre Auger Observatory can be found in Chapter 4. Details about the reconstructions are given in Chapter 5.

An essential, SD-related quantity is the signal strength as a function of the distance from the shower core, called "Lateral Density Function". Figure 3.2 shows a lateral density function. The signal strength decreases with increasing distances to the core. The particular shape of that function depends on the primary particle, primary energy and the zenith angle.

The total muon number at ground level is an important quantity to distinguish between different primary particles and for a correct energy estimation. Simulations predict [26] an energy-dependent increase of the muon number with approximately $E^{0.85}$ for proton-induced air showers. As we may describe a highly energetic nucleus with the atomic number $A$ and the total energy $E$ as a superposition of $A$ independent nucleons that carry an energy $E/A$, we obtain a relation between its muon number $N_\mu^A$ and the muon number $N_\mu^p$ of a proton-induced air shower via:

$$N_\mu^A = A^{0.15} \cdot N_\mu^p \tag{3.1}$$

That means a muon abundance of about 80% for iron showers, compared to proton showers.

Unfortunately, SD measurements are not capable of differentiating between muons and electrons of EAS efficiently, necessitating simulations. But a muon detector array is being built within the SD array to provide direct measurements of muon numbers.

Moreover, various methods have been developed to distinguish between primary particles using FD measurements. A fluorescence telescope observes the energy deposit or the size of the EAS along its path (called *longitudinal profile*), using the atmosphere as a calorimeter with an absorber thickness of 30 radiation lengths or 11 hadronic interaction lengths [1]. As the density of the air is not a constant, it makes sense to introduce a new quantity to describe the distance traversed by a shower since its initiation in the atmosphere: the *atmospheric slant depth* $X$ [g/cm$^2$]. It measures the length in equidistant intercepts of traversed matter density instead of meters. To explain the longitudinal profile correctly again, it describes the shower size $N$ or the energy deposit $dE/dX$ in the atmosphere as a function of atmospheric slant depth $X$, parametrized by the Gaisser-Hillas function [27]:

$$N(X) = N_{max} \left( \frac{X - X_0}{X_{\max} - X_0} \right)^{(X_{\max} - X)/\Lambda} \exp \left( \frac{X_{\max} - X}{\Lambda} \right) \tag{3.2}$$

where $N_{\max}$ is the maximum shower size, located at a depth $X_{\max}$. $X_0$ and $\Lambda$ are shape parameters.

The basic properties of the dominant electromagnetic cascade have been simplified in the *Heitler model* [28]. In this model it is assumed that, after travelling a distance $\lambda_{\mathrm{em}}$ called *free path length*, each photon and electron produces a pair of new particles with each particle gaining half of its energy. A series of $n$ iterations would yield $2^n$ particles carrying an energy $E_0/2^n$. This cascade production process stops when the particle energy reaches a critical energy $E_c$. Below this energy ionization processes take place. Thus the maximum shower size $N_{\max}^{\mathrm{em}} = E_0/E_c$ can be approximately found at a position $X_{\max}^{\mathrm{em}}$:

$$X_{\max}^{\mathrm{em}}(E_0) \approx \lambda_{\mathrm{em}} \cdot \log_2 \left( \frac{E_0}{E_c} \right) = X_{\mathrm{R}} \cdot \ln \left( \frac{E_0}{E_c} \right) \tag{3.3}$$

where $X_{\mathrm{R}}$ is the radiation length in air.

This formula does only estimate the depth of the shower maximum for photon- or electron-induced showers. For primary hadrons all shower components have to be taken into account. A simplified model assumes that the hadronic interaction of a particle with energy $E_0$ produces $n_{\mathrm{tot}}$ new particles with energy $E_0/n_{\mathrm{tot}}$, assuming two thirds to be $\pi^{\pm}$ and one third to be $\pi^0$. Neutral pions decay into photons ($\pi^0 \rightarrow 2\gamma$) and thus carry about 30% of the energy to the electromagnetic component. Depending on their energy, charged pions or kaons either re-interact with air nuclei or decay, producing approximately one muon per decay.

After $n$ generations the energies of the hadronic and electromagnetic component are:

$$E_{\mathrm{had}} = \left( \frac{2}{3} \right)^n E_0, \qquad E_{\mathrm{em}} = E_0 - E_{\mathrm{had}} = E_0 \left( 1 - \left( \frac{2}{3} \right)^n \right) \tag{3.4}$$

Assuming that the first hadronic interaction produces electromagnetic particles that have an energy $E_0/n_{\mathrm{tot}}$ each, a lowest order approximation of the shower maximum of a hadron-

induced air shower yields

$$X_{\max}(E_0) \approx \lambda_{\text{had}} + X_{\max}^{\text{em}}(E_0/n_{\text{tot}}) = \lambda_{\text{had}} + X_{\text{R}} \cdot \ln\left(\frac{E_0}{n_{\text{tot}} E_{\text{c}}}\right) \tag{3.5}$$

where $\lambda_{\text{had}}$ is the hadronic interaction length. The shower maximum is shifted up to higher altitudes above ground for primary hadrons compared to photons or electrons.

In order to reveal intrinsic properties of primary protons and nuclei of the atomic number $A$, a *superposition model* can be applied for UHECR, describing a nucleus with energy $E_0$ as a superposition of its $A$ nucleons. Each nucleon carries an energy fraction $E_0/A$. This model leads to the following relations for size $N_{\max}$ and depth $X_{\max}$ of the shower maximum of protons (index $p$) and nuclei (index $A$), carrying an energy $E_0$:

$$N_{\max}^{\text{A}} \approx A \cdot \frac{E_0/A}{E_{\text{c}}} = \frac{E_0}{E_{\text{c}}} = N_{\max} = N_{\max}^{\text{p}} \tag{3.6}$$

$$X_{\max}^{\text{A}} \approx X_{\max}(E_0/A) = X_{\max}^{\text{p}} - X_{\text{R}} \cdot \ln A < X_{\max}^{\text{p}} \tag{3.7}$$

$X_{\max}^{\text{A}}$ is shifted to a lower depth for larger atomic numbers $A$. Its size $N_{\max}^{\text{A}}$ is similar for all primary hadrons. Moreover, a nucleus has a larger cross section than a proton due to its size and thus interacts even higher in the atmosphere.

An experimental observable for the shift of the depth of the shower maximum with the energy is the elongation rate $D$. It is defined as the change of the average depth of the shower maximum per energy decade [29], obeying $D = d\langle X_{\max}\rangle / d(\ln E)$. This derivation can be calculated for the different primaries:

$$D^{\text{em}} = X_{\text{R}} \tag{3.8}$$

$$D^{\text{p}} = \frac{d\lambda_{\text{had}}}{d\ln E} + X_{\text{R}} \cdot \left(1 - \frac{d\ln n_{\text{tot}}}{d\ln E}\right) \tag{3.9}$$

$$D^{\text{A}} = D^{\text{p}} - X_{\text{R}} \cdot \frac{d\langle\ln A\rangle}{d\ln E} \tag{3.10}$$

The elongation rate is an essential quantity for composition studies (see Section 3.3). A further, essential issue are shower fluctuations. Fluctuations in the shower development are mainly caused by fluctuations in the atmospheric depth, in the characteristics of the first few interactions and in the ratio of charged and neutral pions within the first generations. The magnitude of shower fluctuations ranges from 5% for the electromagnetic component to 15% for the muonic component [3].

The following quotation emphasizes the importance of FD measurements for composition studies (J. Bellido, [30]): "The analysis of the characteristics of the detected longitudinal profile is currently the most reliable way for extracting some information about the primary cosmic ray mass composition."
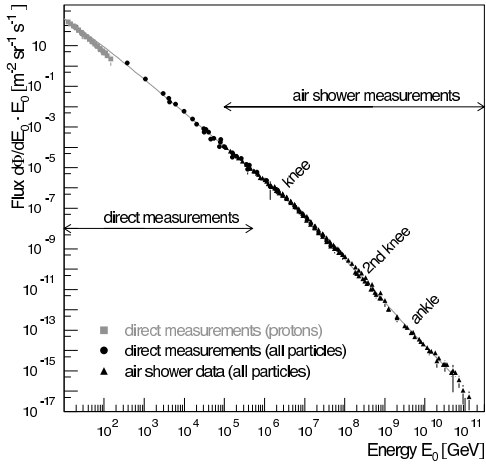
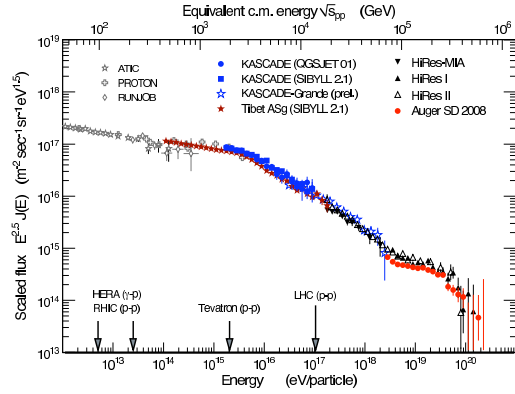**Figure 3.4:** All-particle energy spectrum of CR (from [2]).



**Figure 3.5:** All-particle energy spectrum of CR, weighted by $E^{2.5}$ (from [2]).

## 3.2 The Energy Spectrum

The energy spectrum given in Fig. 3.4 and 3.5 extends over a remarkably wide energy range from a few hundreds MeV to beyond $10^{20}$ eV. It illustrates the average differential flux of non-thermal origin for all types of primary particles as a function of energy.
The flux approximately follows a power law, where $\gamma$ is the spectral index (see also [2]):

$$\frac{dN}{dE} \propto E^{-\gamma} \tag{3.11}$$

It decreases from about 1000 particles per second and $m^2$ at GeV energies to about one particle per $m^2$ and year in the PeV range and to just about one particle per $km^2$ and century for the highest energies above 100 EeV. As mentioned before, the strong decrease of the flux energies above several PeV requires a large exposure[1] of a detector to obtain a sufficient observation rate. Appropriate exposures are available in ground-based air shower arrays. The eposures of various ground experiments are given in Fig. 3.6.

A weighting of the spectrum by $E^{2.5}$, depicted in Fig. 3.5, resolves slight structures that can merely be guessed with the naked eye from the unweighted spectrum. The kink around $\sim 4 \cdot 10^{15}$ eV called *knee* causes an increase of the spectral index $\gamma$ from 2.7 to 3.1. A *second knee*, which is not commonly agreed on up to now, is located at approximately $4 \cdot 10^{17}$ eV. The *ankle* is located at about $4 \cdot 10^{18}$ eV. A further feature is a cutoff at $6 \cdot 10^{19}$ eV, called Greisen - Zatsepin - Kuzmin (GZK) cutoff. After a long puzzle about the existence of the GZK effect due to contrary results of AGASA and HiRes, Auger measurements finally confirmed the findings of HiRes in 2007. Both results support a GZK-like cutoff with a significance of more than 6 standard deviations (HiRes 4.5

---

[1]The concept of exposure, as known from photography can be applied on the terms used to describe detectors. Its dimension in this context is $km r \cdot sr \cdot year$. The flux times the exposure equals the number of particles within the time, area and angular section given by the exposure.
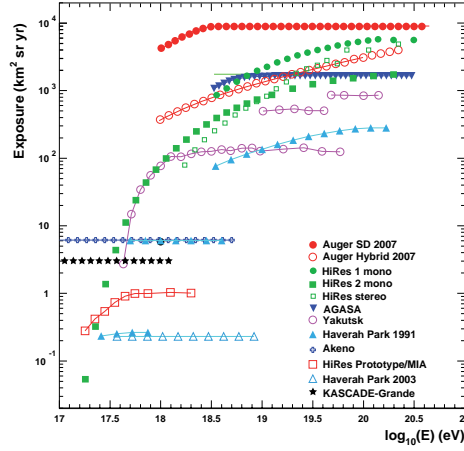
**Figure 3.6:** The exposures of various ground experiments (from [1]). An increase of the exposure with the energy results from increasing detection volumes of fluorescence detectors. A constant exposure is typical for surface detectors.
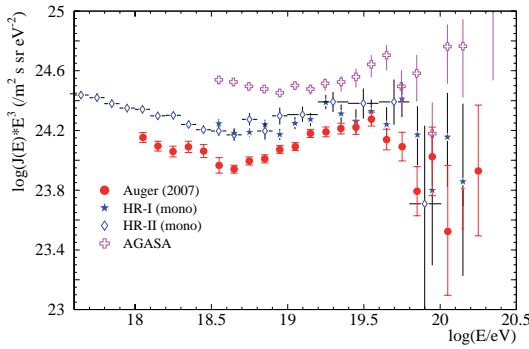


**Figure 3.7:** CR flux measurements (scaled by $E^3$) from AGASA, HiRes and Auger (from [1]).
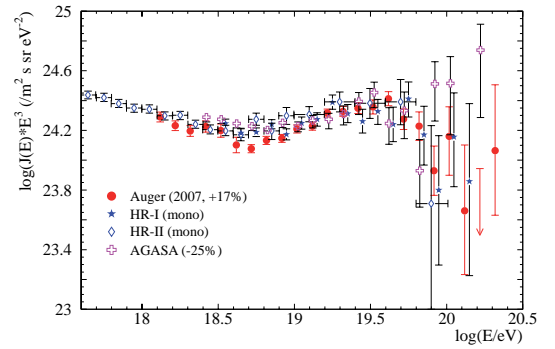


**Figure 3.8:** Same plot as Fig.3.7 but with shifted energy scales (Auger +17%, AGASA -25%). (From [1])

standard deviations). Interactions between UHECR ($E \geq 10^{20}$ eV) and photons of the cosmic microwave background (CMB, discovered 1965 [31]) reversely confine the possible sources of CR to lie within a maximum distance (i.e. a few tens of Mpc for protons with $\sim 10^{20}$ eV [32]). The interactions are mainly photo-pion productions in case of primary protons ($p + \gamma_{CMB} \rightarrow \Delta^+(1232) \rightarrow p + \pi^0 \rightarrow p + \gamma\gamma$) and photodisintegration in case of primary nuclei.

The interpretation of these spectrum features regarding the origin and acceleration of CR is discussed in Chapter 3.4.

An issue concerning the absolute measured values in the spectrum arises in a comparison of results of three experiments with an overlapping energy range: Auger, AGASA and HiRes. Figure 3.7 shows the $E^3$-weighted CR fluxes without a shift of the energy

scale of Auger and AGASA, obviously differing in overall flux and shape.

As the experiments employ different detector types, it is urgent to compare the results within their statistical and systematic uncertainties in order to check if the results are compatible within their uncertainties. AGASA uses scintillation detectors and HiRes fluorescence detectors, while Auger combines Cherenkov and fluorescence detectors.

Beyond statistical uncertainties, there are several kinds of systematic energy uncertainties depending on the particular detection method, as each method is coupled with different sorts of implied models. An estimate of a typical energy scale uncertainty yields 20-25%. Energy measurements of surface detector arrays base entirely on simulations of EAS that underlie hadronic interaction models. Our incomplete knowledge about hadronic interaction models, in particular total inelastic cross sections and particle multiplicities, causes large uncertainties of the predicted muon density on ground level from the different models up to 30% [1]. As fluorescence detectors observe a large fraction of the longitudinal shower profile, their measurements depend mainly on the fluorescence yield model. The fluorescence yield is given via

$$Fl.yield_\lambda = \epsilon_\lambda(p,T) \cdot \frac{\lambda}{hc} \cdot \frac{dE}{dX} \cdot \rho_{air} \left[ \frac{photons}{m} \right] \tag{3.12}$$

where $\epsilon_\lambda(p,T)$ is the fluorescence efficiency (energy out of photons per energy deposit in medium), $h$ the Planck constant, $c$ the speed of light, $\lambda$ the wavelength and $\rho_{air}$ the air density.

The Auger Collaboration uses the Nagano model of (2004, [33]), while the HiRes Collaboration uses the older Kakimoto model (1996, [34]). The relative shift of the resulting energy scales of both experiments due to the different models is up to 10%. Factoring all this into the measurements of the flux, a shift of the Auger energy scale by +17% and a shift of the HiRes energy scale by -25%, as shown in Fig. 3.8, yields a quite consistent result within the discussed uncertainties. Detailed remeasurements of the fluorescence yield for various external conditions are an ongoing issue to minimize the related uncertainties.

## 3.3 Chemical Composition

In principle, cosmic ray particles cover the whole range from protons to iron nuclei. For the low energy range up to the *knee* the composition can be measured directly (Fig. 3.13), yielding a mass spectrum similar to the abundance of elements in the solar system.

Indirect composition studies in the ultra-high energy range pose a big experimental and analytical challenge on one hand and an important tool on the other hand. The analysis of the composition of CR is essential to rule out or to confirm acceleration models and to explain the features of the energy spectrum, for every model predicts an intrinsic composition. The key observable for composition studies in ground-based air shower experiments is the position of the longitudinal shower maximum, $X_{max}$. It can either be measured directly by fluorescence telescopes or inferred from measurements with Cherenkov detectors.
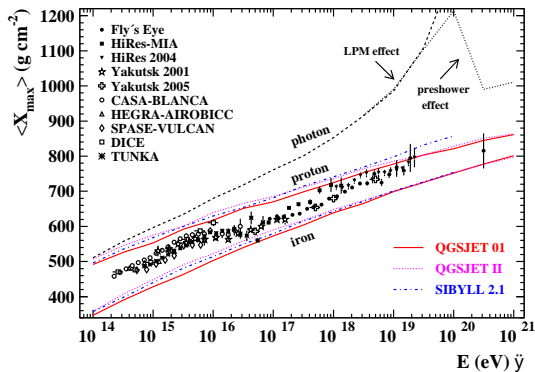
**Figure 3.9:** $\langle X_{\max} \rangle$ as a function of energy (called *elongation rate*), comparing measured data to the results for simulated primary photons, protons and iron nuclei (from [35] and references therein).
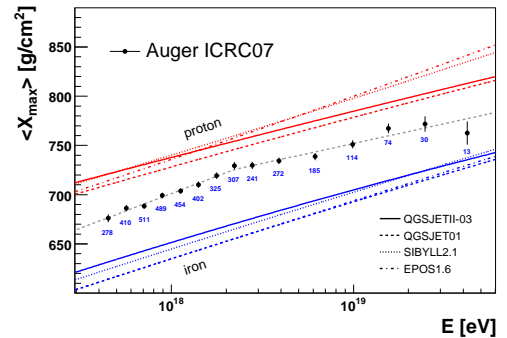


**Figure 3.10:** $\langle X_{\max} \rangle$ as a function of energy (called *elongation rate*), compared to proton- and iron-predictions of various hadronic interaction models. The dashed line represents a broken line fit of Auger Hybrid data with two constant elongation rates (from [36]).

For a reasonable shower reconstruction quality the shower maximum has to lie within the field-of-view of the telescopes.

In section 3.1 it was already mentioned that the position of the shower maximum, $X_{\max}$, depends on the primary particle and its energy, as illustrated in Fig. 3.9. The average depth of the shower maximum, $\langle X_{\max} \rangle$, and its spread decrease with increasing atomic numbers $A$. Those features provide an important basis for composition studies.

As we neither have enough statistics to apply unfolding methods nor enough efficiency for a separation of muons and electrons, the UHECR composition for different energies is estimated by a comparison of measured and different simulated elongation rate[2] spectra. The measured elongation rates and simulations using various models are given in Fig. 3.10. For a pure composition the expected elongation rate is about 50 g/cm$^2$/decade, depending on the particular model. The data have been fitted with a broken line fit that yields the best probability of 63%. At $\sim 2$ EeV the elongation rate changes from $71 \pm 5$ g/cm$^2$ below to $40 \pm 4$ g/cm$^2$ above the break [30]. Assuming entirely correct hadron models, we would conclude a mixed composition with a trend to lighter nuclei up to 2 EeV and a trend to heavier nuclei above the breaking point. Instead of a change in the composition, the reason for the sudden change in the elongation rate could be a hadronic interaction property in the high energy range. An interesting feature is the fact that also the energy spectrum shows an intrinsic structure at an energy of 2 EeV, the ankle, though it is not yet clear if there is a connection between those structures [30].

Further SD- and FD-related methods for composition studies have been and will be developed. In addition to the absolute value of the position of the shower maximum, $X_{\max}$, its spread can be analysed to extract information about the composition as well. As men-

---

[2]The elongation rate was introduced in Section 3.1.

tioned in section 3.1, an iron nucleus shows a smaller RMS than a proton since the nucleus can be described as a superposition of 56 nuclei, each carrying the 56th part of the total energy. An advantage of this method is a less strong dependence on hadronic interaction models, but it depends strongly on the cuts applied on the dataset. Common SD-related quantities for analyses of the UHECR composition are the *rise-time* of a detector signal and the signal shape, the *bumpiness*, that differ for muons and electromagnetic particles and thus for different primary particles. Moreover, the variation of the rise-time around the shower core and the ratio between the early signal within the first 600 ns and the late signal after 600 ns both contain information about the ratio of muons and electromagnetic particles.

If all these parameters were extracted from common events, a multiparameter analysis could be performed as a powerful combination of all these approaches.

So far, photons as possible primary particles have not been explained yet. Photon-induced showers can be clearly distinguished from showers of charged primary particles by means of a much larger depth of the shower maximum and a dominant electromagnetic shower component, as mentioned in Section 3.1. As ultra-high energetic (UHE) primary photons have not been detected up to now, while some models predict certain photon fractions, an important issue consists in constraining the UHE photon as a function of energy. Figure 3.11 shows upper limits on the UHE photon fraction for different experiments, compared to predictions of various models and the GZK effect. The highest energetic photons measured so far were of the TeV range.

Another primary particle candidate has not been mentioned yet: UHE cosmic neutrinos. All UHECR models predict a different flux of neutrinos either produced in hadronic interactions at the sources or during the propagation of cosmic ray particles in background fields. Thus UHE neutrinos serve as further indicators for particular models, similarly to UHE photons. An important property of neutrinos are flavour oscillations, leading to equal numbers of $\nu_e$, $\nu_\mu$ and $\nu_\tau$ for any initial ratio. Earth-skimming UHE tau neutrinos $\nu_\tau$ can be measured indirectly at the Pierre Auger Observatory with horizontal showers. The other neutrino flavours are absorbed in the earth for energies exceeding $10^{15}$ eV. Those $\nu_\tau$ can produce their charged partner $\tau$ in the earth that eventually initiates a nearly horizontal air shower. Up to now no UHE neutrino has been measured yet, leading to upper limits on a diffuse flux of $\nu_\tau$, as given in Fig. 3.12. This plot shows predicted limits of different experiments and the predicted number of GZK-neutrinos. As for photons, top-down models have already been constrained [1].

Composition studies represent a basis for discriminating UHECR origin models and might solve the question about the transition from galatic to extragalactic CRs [1]. New detector components will be or have been built at the Pierre Auger Obervatory to expand the energy range to lower energies and providing muon detection.
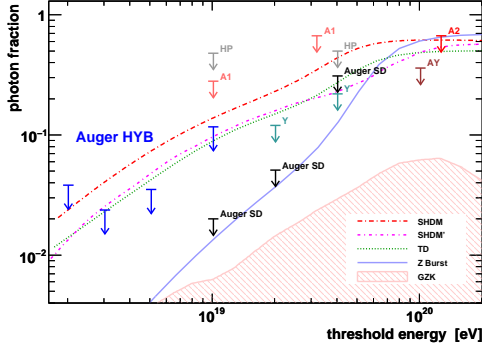
**Figure 3.11:** Upper limits on the photon fraction from the integral CR flux, compared to predictions of different EHECR origin models and to the fraction of GZK photons (shaded region). (From [37] and references therein.)
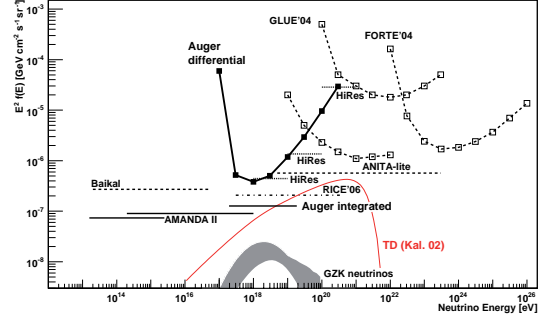


**Figure 3.12:** Upper limits on a diffuse flux of $\nu_\tau$ at 90% C.L., assuming equal neutrino numbers for each flavour (from [1] and references therein).

# 3.4 Origin and Acceleration of UHECR

This section is based mainly on [2]. The experimental key to solve the mystery about the origin of (UHE) cosmic rays are measurements of their chemical composition, flux and arrival direction distribution. Features of the energy spectrum constrain possible sources of particular energy ranges to distance regions, such as a maximum distance of 100 Mpc due to the GZK effect, our Galaxy or extragalactic sources. The primary mass composition restricts possible source candidates due to their chemical composition. Measurements of the arrival direction distribution might directly point out possible sources by analysing eventual correlations with catalogues of source candidates. Complementary information are obtained analysing fluxes of secondary particles (i.e. UHE photons and neutrinos) produced in hadronic interactions in the source or during the propagation.

In order to constrain source candidates locally and, in particular, to understand at which energies the transition from galactic to extragalactic cosmic rays takes place, it is essential to measure the features of the energy spectrum in detail and with sufficient statistics. The knee turned out to play an important role in this context. In the last decades various models have been proposed to explain the *knee*, the *ankle* and a possible *second knee*. They can be merged to two main groups: Phenomenological and theoretical models.

A phenomenological model, called *poly-gonato* model [38], describes the knee as a series of knees belonging to different nuclear charge numbers $Z$. Assuming the proton knee cut-off to be located at an energy $E_{\text{knee}}^p \approx 4$ PeV, the series obeys $E_{\text{knee}}^Z = Z \cdot E_{\text{knee}}^p$. It explains the commonly accepted first knee to be the starting point while, based on a potential important role of heavy elements in the high energy range, a so-called second knee at about $92 \cdot E_{\text{knee}}^p \approx 4 \cdot 10^{17}$ eV might indicate the end of the galactic component.
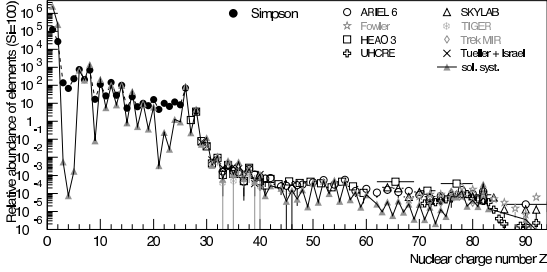
**Figure 3.13:** Abundance of elements in CR as function of their nuclear charge number $Z$ at energies around 1 GeV, normalized to $Si = 100$. In addition, the abundance of elements in the solar system is shown (from [2] and references therein).
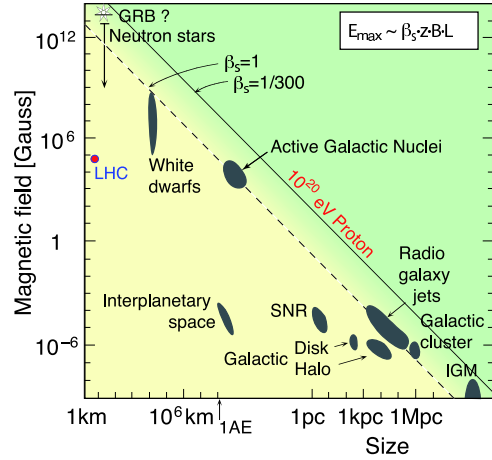


**Figure 3.14:** Hillas plot: Astrophysical objects below the diagonal line cannot accelerate CR protons up to $10^{20}$ eV (from [39]).

On the contrary, other theories suppose galactic accelerators to faint around $E = 30 \cdot E_{\mathrm{knee}}^{\mathrm{p}}$ due to an assumed small fraction of primary heavy nuclei in the GeV energy range. In the classical picture ($G$-$EG$) the ankle represents the transition region from a heavy to a light composition [1].

The theoretical models can be subdivided into subgroups [38]: Models relating the knee to the acceleration process (1), models connecting the knee with leakage of CR from the Galaxy (2), models relating the knee to interactions of CR with background particles (3) and models accounting air shower developments for the knee (4).

1. Models of this group suggest the knee to be a consequence of restricted power of supernova shockwave acceleration or an effect due to alternative acceleration scenarios.

2. Another set of models bases on the assumption of particles escaping the Galaxy above a certain energy (leakage). The knee is explained as a consequence of diffusive propagation of CR through the Galaxy.

3. As known from the GZK effect, CR interact with photons of the cosmic microwave background ($\gamma_{\mathrm{CMB}}$). Some models explain the knee as a consequence of interactions of CR with different kinds of background particles - particularly photons or neutrinos. A well-known model of this context is the *Berezinsky-dip-model*. This model requires primary protons.

4. A last group contains models that assume a currently unknown air shower component to receive a part of the energy from the knee region on, resulting in a dip.

As mentioned before, a helpful tool to rule out transition- and source-models, in addition to flux measurements, are measurements of the composition that can be compared to predictions of each model.

Based on CR measurements around 1 GeV, the resulting mass spectrum can be compared to the abundance of elements in the Solar System, as depicted in Fig. 3.13. Both spectra look macroscopically similar, but there exist momentous differences. Some very light elements and elements below iron and lead are more abundant in CR while heavy elements of the C-N-O, iron, and lead groups appear to be more abundant in the Solar System. The underlying process that relates both effects is assumed to be spallations of the heavier nuclei during their propagation in the Galaxy.

Various ratios of primary nuclei and their spallation products, combined with known spallation cross-sections, provide estimations of quantities like the propagation path length $\lambda_{\mathrm{cr}}$, the residence time $\tau_{\mathrm{esc}}$ of CR in the Galaxy until they escape, the energy density $\rho_{\mathrm{cr}}$ of CR in a volume $V$ and, based on that, the power[3] $L_{\mathrm{cr}}$ required to keep up a constant CR intensity. These estimations are based on two assumptions: Firstly, CR are assumed to propagate through the Galaxy in a diffuse process, being deflected repeatedly by randomly oriented magnetic fields of approximately 3 $\mu$G field strength. Secondly, CR seem to propagate not only in the Galaxy but even in the galactic halo, which has to be factored in the determination of $V$.

Now that we have approximated the power required to sustain a constant CR intensity, the question about suffecent acceleration mechanisms arises. The rate of supernovae in a typical Galaxy is about three per century. In order to explain the spectrum of CR up to the knee region, an acceleration efficiency of about 10% is needed. The formal description of a shock acceleration of CR is given by the *first-order Fermi acceleration*.

This mechanism is located in shock fronts of supernova explosions and bases on a diffuse propagation of a particle from the supernova remnant (SNR) into the interstellar medium (ISM). A particle gains an energy $\Delta E$ moving from the unshocked region (upstream) into the shockfront and the region behind (downstream) and back. The magnetic field $B$ in the upstream and downstream region acts as a mirror that reflects the particle. This cycle is being repeated until the particle escapes into the ISM. A longer duration of the whole acceleration results in a higher total energy. The maximum energy $E_{\mathrm{max}}$ that a particle can gain after a time $T$ in a shockfront moving with a velocity $v_{\mathrm{s}}$, containing a large-scale magnetic field of field strength $B$, is (cf. [40], p. 68):

$$E_{\mathrm{max}} = Z\, e \cdot \beta_{\mathrm{s}} \cdot B \cdot T\, v_{\mathrm{s}} \qquad (3.13)$$

where $\beta_{\mathrm{s}} = \frac{v_{\mathrm{s}}}{c}$ represents the velocity of the shockfront and $L = T\, v_{\mathrm{s}}$ the size of the source region. This relation can be approximated for an average SNR:

$$E_{\mathrm{max}} \propto Z \cdot 10^{14}\ \mathrm{eV} \qquad (3.14)$$

The outlined first-order Fermi acceleration yields a non-thermal power-law spectrum similar to the measured energy spectrum. Possible UHECR source candidates can be ex-

---

[3]$\tau_{\mathrm{esc}} \approx 15 \cdot 10^6$ years, $\rho_{\mathrm{cr}} \approx 1$ eV/cm$^3$ $\Rightarrow L_{\mathrm{cr}} = \rho_{\mathrm{cr}} \cdot V/\tau_{\mathrm{esc}} \approx 10^{41}\ \frac{\mathrm{erg}}{\mathrm{s}}$. (1 erg $= 10^{-7}$ J $\simeq 624.15$ GeV)
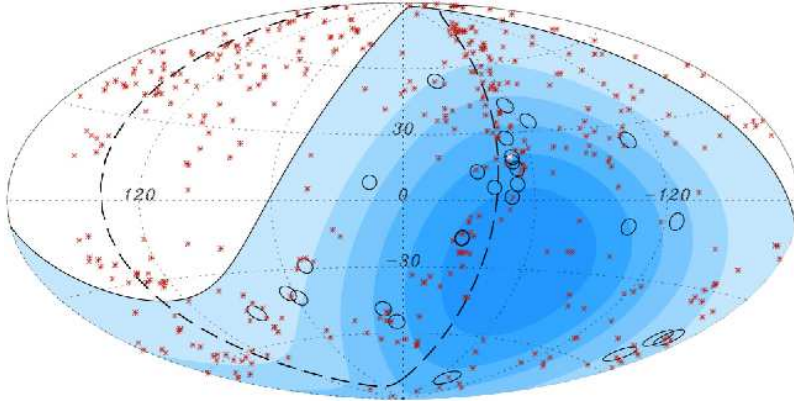
**Figure 3.15:** Aitoff projection of the celestial sphere in galactic coordinates. The positions of AGN within $D < 71$ Mpc and of events with $E > 57$ EeV are marked with stars and circles respectively. The blue gradient indicates equal exposures (from [41]).

tracted from the so-called Hillas plot (Fig. 3.14). This plot contains all combinations of the source-specific quantities $L$ and $B$. In this representation a constant maximum acceleration follows a line perpendicular to a line with $45°$ slope. The resulting list of possible UHECR source candidates contains active galactic nuclei (AGN), radio galaxy jets and gammy-ray bursts (GRB).

Composition measurements could help to restrict this set of possible source candidates and acceleration models. Another promising issue is *CR astronomy* above approximately $10^{19.5}$ eV. As magnetic deflections of charged UHECR particles of this energy range in extragalactic and galactic magnetic fields are expected to be only a few degrees, direct meaurements of UHECR correlations with presumably extragalactic objects (due to GZK) should be possible in high statistics meaurements. A sky map, measured with the Pierre Auger Observatory, is shown in Fig. 3.15.

Until that point, CR are assumed to be accelerated from very low or even rest energy to high energies by interactions with large-scale magnetic fields. Alternative scenarios suggest a decay of super-heavy objects instead of acceleration. They are called *top-down-models*. All of them predict high fluxes of UHE photons and thus could be finally ruled out by constraining the UHE photon-limits to the predicted GZK background.

# Chapter 4

# The Pierre Auger Observatory

The southern site of the Pierre Auger Observatory is located in the the Pampa Amarilla in western Argentina near the town Malargüe. It covers an area of 3000 km$^2$ to detect air showers initiated by the highest energetic cosmic rays in the atmosphere, accounting for their low flux. An EAS leaves its marks in various ways. The Pierre Auger Observatory measures the fluorescence light produced by an air shower using fluorescence telescopes until the shower cone smashes into the ground, leaving an electric signal in the surface detector array. Figure 4.1 sketches the observatory. The array of about 1660 Water Cherenkov Detectors, forming a triangular grid of 1.5 km spacing, is overlooked by four telescope stations called *eyes*. Each eye comprises six telescopes. With regard to the detection technique, the Pierre Auger Observatory is called a *Hybrid detector*. A clear advantage of this technique are cross-calibrations and cross-checks between both systems. The first surface detector was deployed in 2002, stable data have been taken since January 2004 and the construction of the whole detector array was finished in June 2008 [42].

The observatory will be or has been extended with detectors to measure efficiently in a lower energy range, by muon detectors and by radio antennae. Moreover, a northern site is planned to be built in Colorado (USA) to achieve a full sky coverage. Once finished, an area of 10000 km$^2$ will be covered by 4000 surface detectors and additional fluorescence telescopes.

## 4.1  Surface Detectors

The Surface Detectors (SD) are cylindrical, opaque tanks of 1.2 m height and an area of 10 m$^2$, filled with 12.000 liters of purified water. This detector type is also called *Water Cherenkov Detector*. When a shower hits a tank, the incident particles produce Cherenkov light, as their speed in the water exceeds light velocity. Three photomultiplier tubes (PMT) are directed downwards into the water to measure the light produced in the water. The tank height has been optimized for a clear muon signal and a separation of the muon signal from the signal of the electromagnetic shower component.

An EAS hits several tanks, producing different signal strengths in and a relative timing between the triggered tanks. The timing and coordinate information are available using
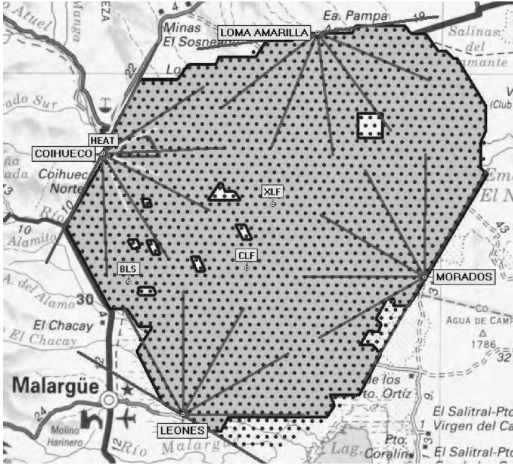
**Figure 4.1:** The Pierre Auger Observatory. Each point represents a surface detector (SD). The SD array is framed by four fluorescence telescope stations: Los Leones, Los Morados, Loma Amarilla and Coihueco (from [42]).
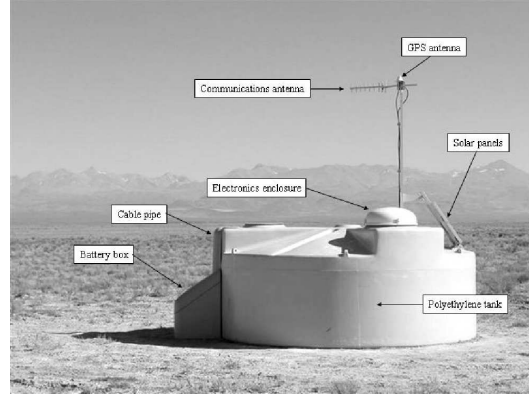


**Figure 4.2:** The water-filled SD tanks measure the Cherenkov light that a shower produces in the water. Each tank features a solar panel, a battery box, a GPS antenna, an antenna for communication between the detectors and encloses the entire electronics (from [43]).

GPS antennae. A second antenna, placed on each tank, is used for the communication on the array. The high voltage for the PMT is provided by a solar power system.

The tank calibration is performed separately for each tank using single down-going atmospheric muons, as they are known to form a uniform background. The gain of each PMT is adjusted to obtain a certain trigger rate above a fixed threshold. The accuracy of this calibration is about 5%. Due to the calibration, the SD signal is usually expressed in units of vertical equivalent muons (VEM). One VEM corresponds to the average signal produced by a single vertical muon. The average signal is measured using a test tank. Section 5.1 explains the event reconstruction based on SD measurements.

## 4.2 Fluorescence Telescopes

The Fluorescence Detectors (FD) comprises four eyes called Los Leones, Los Morados, Loma Amarilla and Coihueco. The buildings are in a slightly elevated position with respect to the SD array to guarantee an unhindered view onto the atmosphere above the array. Each building contains six individual fluorescence telescopes with a field-of-view of $\sim 30° \times 30°$ in azimuth and elevation respectively. The overall field-of-view of each eye thus is $\sim 180° \times 30°$. A scheme of an individual telescope is illustrated in Fig. 4.3. The nitrogen fluorescence light produced by EAS within the field-of-view of a telescope enters the telescope by passing a UV-filter and a Schmidt optics corrector ring. It is focussed onto the camera by a segmented mirror of an overall area of about 10 m$^2$. The camera consists of a $22 \times 20$ matrix of PMT. Each PMT covers 1.5° in azimuth and elevation.

Incoming photons produce an electric pulse in the PMT that is proportional to the light intensity. The camera is digitized every 100 ns. Subsequent triggers filter the data for shower traces to reduce the volume. Shower traces are recorded as a sequence of triggered PMT forming a narrow line in the camera (see Fig. 4.4). The shower geometry is determined from the direction and timing information of this trace. Once the geometry is fixed, the longitudinal shower profile is determined using a Gaisser-Hillas fit (cf. Eq. 3.2). The electromagnetic energy is derived from the integral of the longitudinal profile over the traversed atmospheric depth. The reconstruction of FD events is described in Section 5.2.

To assure a correct FD energy measurement, the telescopes have to be calibrated and monitored. A calibration is necessary to convert the digitized ADC[1] signal of the camera to the incident photon flux. The **absolute calibration** is performed using drum-shaped, homogeneous diffusive light source of 2.5 m diameter, providing an equal light flux for each pixel. The pixels are calibrated by the drum light emission that is known from laboratory measurements within an overall uncertainty of 9%. This calibration should be performed three or four times a year.

The **relative calibration** aims to track short and long term changes of the PMT calibration and to check the stability of the method used for the absolute calibration, assuring stable FD measurements.

As the isotropically emitted fluorescence light is very faint and it has to travel several kilometers through the atmosphere, FD measurements are sensitive to presence of aerosols that attenuate the light on its way to the detector. Therefore, events have to lie within a certain distance to the telescope. The atmosphere is measured continuously to correct the signal for its influence afterwards (see Section 4.3).

A clear constraint of FD measurements and thus of hybrid detection is the duty cycle. FD measurements can only be performed in clear, moonless nights which leads to a duty cycle of about 13% for FD and Hybrid measurements, whereas the duty cycle of the SD array is approximately 100%.

As calorimetric energy measurements using fluorescence telescopes are independent of simulations, the SD energy scale is calibrated by the FD energy scale resulting from Hybrid measurements almost independent of simulations.

A detailed description of the fluorescence telescopes is given in [45].

Events with at least two triggered eyes are called *multi-eye events*. According to the number of triggered eyes they are called *stereo* (2), *triple* (3) and *quadrupole* (4) events. Most multi-eye events can be found close to the center between the triggered eyes. They play an important role in the estimation of the FD or Hybrid resolution of various quantities based on measured data.

---

[1]ADC means *Analog to Digital Converter*. It converts an analog to a digital signal.
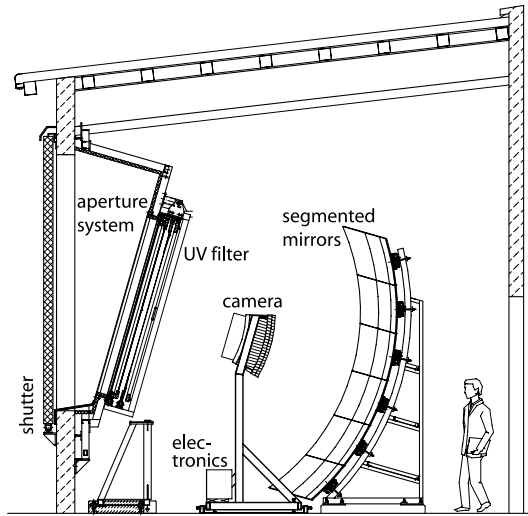
**Figure 4.3:** An individual fluorescence telescope. The fluorescence light passing a UV-filter is focussed onto the camera by a segmented mirror (from [45]).
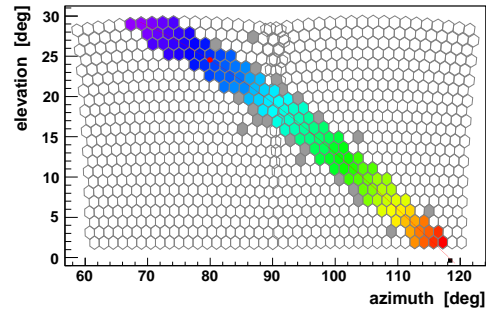


**Figure 4.4:** A shower crosses the field-of-view of two FD telescopes, leaving a trace in the cameras. The gradient from blue to red represents the evolution of the shower with time.

## 4.3   Atmospheric Monitoring

In order to assure a reliable energy reconstruction for the telescopes, it is necessary to monitor the atmosphere. The fluorescence light has to be corrected for the attenuation by molecular (Rayleigh) and aerosol (Mie) scattering.

The molecular atmospheric conditions are monitored in terms of temperature, pressure, density, atmospheric depth, relative humidity, wind speed and wind direction by weather stations.

The optical atmospheric conditions (i.e. the presence of aerosols) are measured using laser shots of LIDAR stations located at each eye and of two laser facilities located near the center of the array. Moreover, the horizontal attenuation length at several wavelengths is monitored. Measurements of the cloud coverage in the field-of-view of each eye are performed using cloud cameras.

### LIDAR

During FD measurements elastic backscatter LIDARs (LIght Detection And Ranging) monitor the vertical atmospheric optical depth (VAOD) of the atmosphere. This quantity is essential for the determination of the light attenuation of the fluorescence light from the point of its initiation to the detector by atmospheric scattering. The VAOD is directly related to the transmission coefficient. One LIDAR is located at each eye, measuring the backscattered light of vertical shots of pulsed UV lasers.

## Laser Facilities

The Central Laser Facility (CLF) and the eXtreme Laser Facilitiy (XLF) are both located close to the center of the detector array with a distance of about $25 - 30$ km to each eye. Both facilities are located rather equidistantly to three of the four sites. They feature pulsed UV-lasers of variable intensity with a wavelength[2] of 355 nm. The laser is mounted in a way that it can be directed to any position in the sky within an accuracy of 0.2°. The scattered light of the vertical laser shots is detected with one or more telescopes and the energy is reconstructed. These measurements provide a determination of the VAOD related to different directions. Moreover, the horizontal uniformity of the atmospheric scattering is monitored.

A more detailed description of the atmospheric aerosol monitoring is given in [46], for instance.

---

[2]The wavelength of the UV lasers is close to the wavelength of nitrogen emissions.

# Chapter 5

# Event Reconstruction

The event reconstruction can be performed using different reconstruction methods. This thesis is focussed on Hybrid- and especially Golden Hybrid-reconstructed data. Details about the SD reconstruction can be found in [47], details about the FD and Hybrid reconstruction are given in [45].

All reconstructions used in this thesis are based on the $\overline{\text{Off}}\underline{\text{line}}$ framework introduced in Section 5.5.

## 5.1   SD Reconstruction

The aim of the *SD reconstruction* is to determine the shower geometry, the lateral density function, the energy estimator $S_{1000}$ and mass-sensitive shower parameters. The determination of the mass-sensitive parameters will not be explained in detail, as the focus lies on the geometry and energy resonstruction.

The $\overline{\text{Off}}\underline{\text{line}}$ SD reconstruction chain is given in Fig. 5.1. The module `SdCalibrator`[1] rejects randomly triggered tanks by applying cuts on the relative event timing and the calibration of the triggered tanks. The `SdEventSelector` flags triggered tanks with no error code as candidate tanks and isolated tanks or tanks without reconstructed data as accidental tanks. Moreover, it provides a treatment of infill[2] stations. The calculation of triggers called T4 and T5 allows an offline data selection based on particular configuration patterns of working, active tanks. The T4 trigger selects physical data. The T5 trigger, subdivided into 5T5[3] and 6T5, requires five or respectively six active neighbouring tanks around the tank with the highest signal, called *hottest tank*. According to [44], the 5T5 trigger is recommended for events with 10 tanks or more.

---

[1] From now $\overline{\text{Off}}\underline{\text{line}}$ modules indicated using a typewriter font.

[2] The Pierre Auger Observatory as well as its extensions are outlined in Chapter 4.

[3] The 5T5 trigger is also called T5-ICRC.

```
<sequenceFile>
  <moduleControl>
    <loop numTimes="unbounded">
      <module> EventFileReaderOG </module>
      <module> SdCalibratorOG </module>
      <module> SdEventSelectorOG </module>
      <module> SdPlaneFitOG </module>
      <module> LDFFinderOG </module>
      <module> SdRecPlotterOG </module>
    </loop>
  </moduleControl>
</sequenceFile>
```

**Figure 5.1:** The offline module sequence of an SD reconstruction.

### 5.1.1 Shower geometry

The `SdPlaneFit` reconstructs the shower geometry in two steps, requiring at least three triggered tanks. In a first step the shower front is approximated by a plane, as sketched in Fig. 5.2. The origin is shifted into the signal-weighted barycenter of the tanks, $\widehat{b}$. The intersection point of the shower axis and the ground plane is commonly called *shower core*. The shower can be described by a point $\vec{x}(t)$ tracing the shower axis with almost light velocity $c$. The direction of the shower axis is parametrized by the normalized vector $\vec{a}$, pointing to the point of the shower initiation in the atmosphere. Passing the origin at time $t_0$, the difference vector between origin and moving point is:

$$\vec{x}(t) - \widehat{b} = -c \cdot (t - t_0) \cdot \vec{a} \tag{5.1}$$

$$\Rightarrow \quad t_i^{\text{pred}} \doteq t^{\text{pred}}(\vec{x_i}) = t_0 - \frac{1}{c} \cdot \left( \vec{x_i} - \widehat{b} \right) \cdot \vec{a} \tag{5.2}$$

The expression to minimize is the $\sigma$-weighted sum of the squares of the time difference between measured and predicted time $t_i$ over all triggered tanks $i$:

$$\chi^2 = \frac{1}{\sigma_{\text{t}}^2} \sum_i \left[ t_i^{\text{pred}} - t(\vec{x_i}) \right]^2 \tag{5.3}$$

where $\sigma_{\text{t}}$ is the time uncertainty.

This approximation of a plane shower front yields an estimator for the shower axis is improved taking the curvature of the shower front into account. A second minimization is performed to fix the shower geometry.
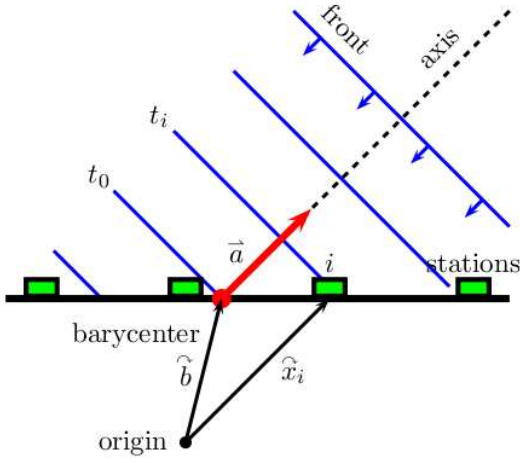
**Figure 5.2:** SD geometry: Scheme of the arrival of an approximated plane shower front (from [48]).
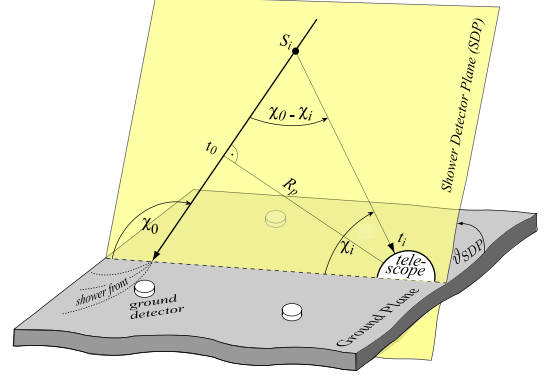


**Figure 5.3:** Illustration of the Hybrid geometry reconstruction (from [50]).

## 5.1.2 Lateral density function and energy

As the SD array measures discrete points of the lateral distribution function (LDF) of the shower signal strength, the `LDFFinder` performs a fit to obtain a continuous function. The lateral dependence of the signal strength $S(r)$ is expressed by the shape parameter $f_{\text{LDF}}(r)$:

$$S(r) = S_{1000} \cdot f_{\text{LDF}}(r) \tag{5.4}$$

$f_{\text{LDF}}$ is given by two different approaches: a modified power law and a slightly modified Nishimura-Kamata-Greisen (NKG) function. The data analysed in this thesis have been reconstructed using the NKG-type function [49]:

$$f_{\text{LDF}}(r) = \left( \frac{r}{r_{1000}} \right)^{\beta} \cdot \left( \frac{r + r_{700}}{r_{1000} + r_{700}} \right)^{\beta + \gamma} \tag{5.5}$$

where $r_{700} = 700$ m and $r_{1000} = 1000$ m. $\beta$ and $\gamma$ are a function of zenith angle.

The fit is performed minimizing the $\sigma$-weighted[4] sum of the square of the difference between measured and predicted signal strength $S_i$ (given by Eq. 5.4 and 5.5) over all triggered tanks, yielding an estimator for $S(r)$. The minimization is based on five parameters: The signal strength 1000 m from the shower core, $S_{1000}$, the shower core parameters in $x$- and $y$-direction and the slope parameters $\beta$ and $\gamma$.

The energy calibration relating the SD estimator $S_{1000}$ to an energy is based on FD energy measurements of hybrid events. It is described in Section 5.4.

---

[4] The uncertainty $\sigma_{S_i}$ of the signal $S_i$ is assumed to be related to the square root of the signal, $\sigma_{S_i} \sim \sqrt{S_i}$.

```
<sequenceFile>

  <enableTiming/>

  <moduleControl>

    <loop numTimes="unbounded" pushEventToStack="yes">

      <module> EventFileReaderOG </module>
      <module> ListOrLoopContinue </module>
      <module> SdCalibratorOG </module>

      <!-- Hybrid reconstruction -->
      <loop numTimes="1">
        <module> FdEventSelectorKG </module>
        <module> FdCalibratorOG </module>
        <module> FdPulseFinderOG </module>
        <module> PixelSelectorOG </module>
        <module> FdSDPFinderOG </module>
        <module> HybridGeometryFinderOG </module>
        <module> FdApertureLightOG </module>
        <module> FdProfileReconstructorKG </module>
      </loop>

      <!-- SD reconstruction -->
      <loop numTimes="1">
        <module> SdEventSelectorOG </module>
        <module> SdSignalRecoveryKLT </module>
        <module> SdPlaneFitOG </module>
        <module> LDFFinderOG </module>
        <module> Risetime1000LLL </module>
        <module> SdEventPosteriorSelectorOG </module>
      </loop>

      <module> RecDataWriter </module>

    </loop>

  </moduleControl>

</sequenceFile>
```

**Figure 5.4:**  The offline module sequence of a Golden Hybrid reconstruction, comprising a full Hybrid and SD reconstruction. A Hybrid reconstruction can be obtained leaving out the SD reconstruction loop.

## 5.2   FD (Hybrid) Reconstruction

The FD reconstruction is performed in three main steps: Geometry reconstruction, reconstruction of the longitudinal profile and energy reconstruction. The FD cameras record a sequence of triggered pixels that form a narrow linear trace, carrying information about the energy deposit of the shower in the atmosphere. The shower is represented by a moving light spot emitting fluorescence light.

### 5.2.1   Shower-detector-plane

After selecting the trace candidate pixels (`FdCalibrator`, `FdPulseFinder`, `PixelSelector`) the shower-detector-plane (SDP) is determined by the `FdSDPFinder`. The SDP is spanned using the position of the eye and the projection of the shower axis onto the camera, given by the trace of triggered pixels. This trace consists of a superposition of the basic pattern illustrated in Fig. 5.5. The uncertainties of the SDP detemination are evaluated by
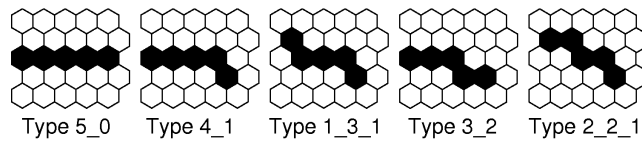
Type 5_0    Type 4_1    Type 1_3_1    Type 3_2    Type 2_2_1

**Figure 5.5:**  Fundamental pattern types regarded as straight track segments (from [45]).

comparing the opening angle between true and reconstructed axis of CLF laser shots.

## 5.2.2   Shower geometry

The next step is the determination of the orientation and position of the shower axis within the SDP. Performing an *FD monocular reconstruction*, the shower axis is determined using the following relation that describes the time $t_i$ when the fluorescence light arrives at the $i^{\text{th}}$ pixel:

$$t_i^{\text{pred}} = t_0 + \frac{R_{\text{p}}}{c} \cdot \tan\left[(\chi_0 - \chi_i)/2\right] \tag{5.6}$$

where $R_{\text{p}}$ is the closest distance between shower axis and eye, $\chi$ the observation angle within the SDP regarding the ground plane and $c$ the velocity of light. The index 0 indicates the situation when the distance between eye and light spot is $R_{\text{p}}$. Figure 5.3 illustrates the related quantities.

The shower axis is fixed minimizing the $\sigma$-weighted sum of the square of the time difference between predicted and measured time over all pixels. The accuracy is limited for small variations in the angular speed $d\chi/dt$ over the observed angular tracklength. In case of an approximately constant angular speed the reconstruction of the shower axis might yield an ambiguous result.

A hybrid detector achieves the best geometrical accuracy using complementary timing information of both detector systems, i.e. the timing of the hottest tank and the FD telescopes. This reconstruction method is called FD Hybrid reconstruction or shortly *Hybrid reconstruction*. Most FD events are also[5] Hybrid events due to an SD duty cycle of nearly 100%. The Hybrid reconstruction is implemented in the module `HybridGeometryFinder`. The related $\overline{\text{Off}}\underline{\text{line}}$ reconstruction chain is given in Fig. 5.4.

The predicted time of a plane shower front triggering the hottest tank can be related to the time $t_0$ when the distance between eye and light spot is $R_{\text{p}}$ (cf. [50]):

$$t_{\text{SD}}^{\text{pred}} = t_0 - \frac{R_{\text{p}}}{c} \cdot \frac{1}{\tan(\chi_0)} \tag{5.7}$$

The combination of both the measured and predicted FD time and the measured and predicted time of the shower plane arriving at the hottest tank is is minimized using the

---

[5]This was not true in the construction-phase, when the FD were constructed faster than the SD tanks deployed. Thus in this phase a large fration of the FD events were FD monocular events.
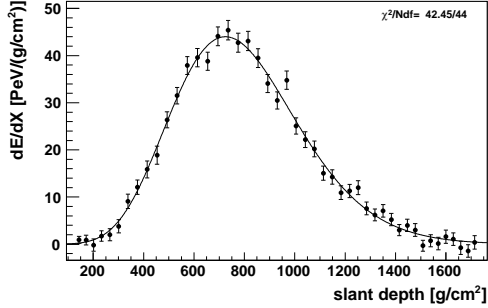
**Figure 5.6:** A longitudinal shower profile, featuring a depth $X_{\max}$ of the shower maximum of approximately 700 g/cm$^2$. The line represents a Gaisser-Hillas fit of the profile (from [45]).
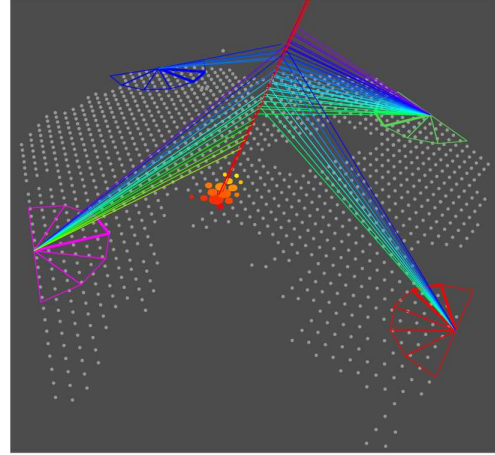


**Figure 5.7:** The first quadrupole event was observed on May 21st 2007 with an energy of approximately $10^{19}$ eV.

following $\chi^2$:

$$\chi^2 = \sum_i \frac{(t_i - t_i^{\mathrm{pred}})^2}{(\sigma_{t_i})^2} + \frac{(t_{\mathrm{SD}} - t_{\mathrm{SD}}^{\mathrm{pred}})^2}{(\sigma_{t_{\mathrm{SD}}})^2} \tag{5.8}$$

where $\sigma_t$ are the uncertainties of the time.

According to [45], the accuracy of the Hybrid-reconstructed FD shower axis is 50 $m$ for the shower core and 0.6° for the shower direction.

An $\overline{\mathrm{Off}}\underline{\mathrm{line}}$ trigger, called *isHybrid*, provides a selection of events with at least one triggered tank and telescope.

## 5.2.3 Longitudinal profile

Once the shower geometry is fixed, the longitudinal shower profile is determined by the `FdProfileReconstructor`. The intensity of the light collected at the aperture as a function of time can be converted to an energy deposit $dE/dX$ in the atmosphere as a function of atmospheric slant depth $X$. As the fluorescence light is scattered in the atmosphere, it is necessary to correct the intensity for molecular (Rayleigh) and aerosol (Mie) scattering as well as for incident scattered Cherenkov light and for multiple scattering.

An example longitudinal profile is given in Fig. 5.6. It is parametrized by a Gaisser-Hillas function (Eq. 3.2).

## 5.2.4 Energy

The electromagnetic energy $E_{\mathrm{em}}$ is obtained from an integration of the energy deposit over the traversed atmospheric slant depth:

$$E_{\mathrm{em}} = \alpha_{\mathrm{loss}} \int_{\mathrm{path}} N(X) \cdot dX = \int_{\mathrm{path}} \frac{dE}{dX} \cdot dX \tag{5.9}$$

where $N(X)$ is the number of particles as a function of slant depth and $\alpha_{\mathrm{loss}} \approx 2.2\,\mathrm{MeV} \cdot (\mathrm{g/cm^2})^{-1}$ the atmospheric loss length. According to [45] the FD energy resolution is 10% or even better.

## 5.3 Golden Hybrid Reconstruction

The Golden Hybrid Reconstruction combines a Hybrid reconstruction (Section 5.2) together with a full, independent SD reconstruction (Section 5.1). The SD geometry reconstruction requires three triggered tanks at minimum. The related subset of data provides comparisons between both reconstructions. Since the SD as well as the FD part of the event trigger the DAQ separately, Golden Hybrid events are independent of a combined trigger.

## 5.4 Energy Calibration

The SD energy calibration is performed using Golden Hybrid events. Fluorescence detectors provide an energy measurement with low uncertainties as the calorimetric measurement is independent of hadronic interaction models. The surface detectors measure the lateral distribution of the shower signal $S$ as a function of the distance $r$ to the shower axis, $S(r)$. This quantity depends strongly on the primary particle type due to related differences in the shower size. Moreover, $S(r)$ depends on the zenith angle $\theta$. As the LDF of different primary particles intersect at a distance $r \approx 1000$ m, $S_{1000}$ is approximately independent of the kind of primary particle, but it still depends on $\theta$.

### 5.4.1 SD energy estimator $S^{38}$

The attenuation curve, depicted in Fig. 5.8, has been fitted assuming a constant flux for the whole energy range considered [51]. This method is called *constant intensity cut* (CIC). The fit is performed using the following quadratic function:

$$\mathrm{CIC}(\theta) = 1 + a \cdot x(\theta) + b \cdot x(\theta)^2 \tag{5.10}$$

where $x(\theta) = \cos^2(\theta) - \cos^2(38°)$. The resulting fit parameters $a$ and $b$ are:

$a = 0.90 \pm 0.05$
$b = -1.26 \pm 0.21$

A new quantity is introduced:

$$S^{38} \doteq S_{1000}/\mathrm{CIC}(\theta) \tag{5.11}$$
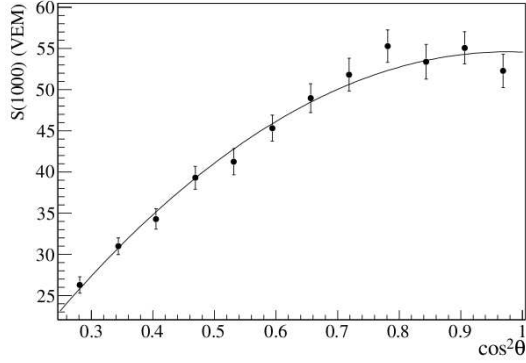
35

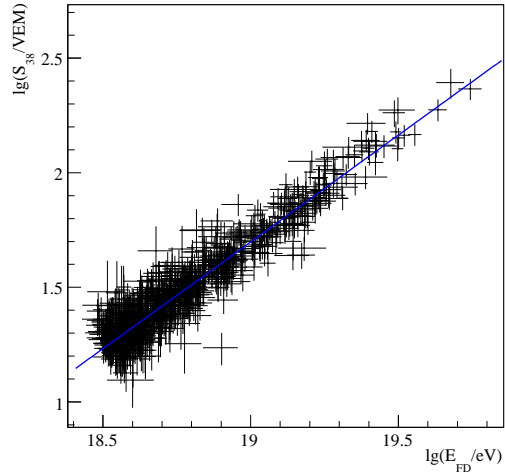**Figure 5.8:** $S_{1000}$ as a function of zenith angle $\theta$ (from [59]).



**Figure 5.9:** Energy calibration spectrum used to calculate the parameters of the calibration function given in Eq. 5.12. The blue line represents the best fit (from [59]).

$S^{38}$ describes the signal strength in units of vertical equivalent muons (VEM) at a distance of 1000 m from the shower core, scaled to an assumed reference zenith angle of 38°. This quantity depends mainly on the FD energy and thus represents an appropriate SD energy estimator.

### 5.4.2 Calibration function

The energy calibration is based on an approximately linear relation between $S^{38}$ and the FD energy $E_{\mathrm{FD}}$,

$$E = a \cdot \left(S^{38}\right)^b \doteq E_{\mathrm{SD}} \tag{5.12}$$

An example calibration spectrum is given in Fig. 5.9. The calibration parameters $a$ and $b$ are determined applying a $\chi^2$ minimization, using function 5.12 (from [59]).
The calibration has been performed several times using different datasets. The analyses of this thesis base on two different calibration functions. The *PRL08* energy calibration [61] is the default calibration that is used up to now. It has been performed on a dataset of 661 Hybrid events from January 1st, 2004 until August 31st, 2007. A derivation of a second, actual calibration is described in [59], flagged as *ICRC09*. This calibration has been performed based on 795 Hybrid events from January 1st, 2004 until December 31st, 2008. All related parameters are listed in Table 5.1. The abbreviations for the calibration functions are not official. They have been introduced for this thesis.
As the SD energy is calibrated by the FD energy scale, it is independent of simulations.

| Calibration | $a$ [EeV/VEM] | $b$ |
|---|---|---|
| PRL08 | $0.149 \pm 0.006\ (stat) \pm 0.012\ (syst)$ | $1.08 \pm 0.01\ (stat) \pm 0.04\ (syst)$ |
| ICRC09 | $0.151 \pm 0.006\ (stat) \pm 0.012\ (syst)$ | $1.07 \pm 0.01\ (stat) \pm 0.04\ (syst)$ |

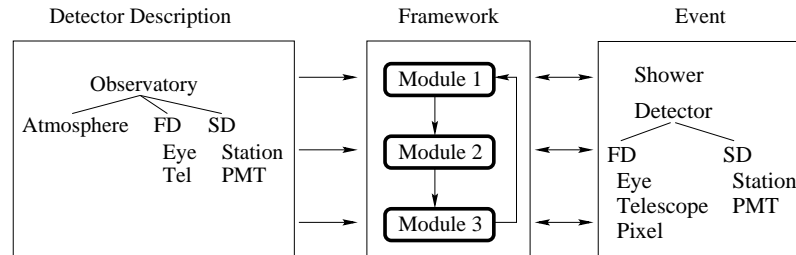**Table 5.1:** Parameters of different SD calibration functions, $E = a \cdot S^{38^b} \doteq E_{\mathrm{SD}}$.



**Figure 5.10:** Simulation and reconstruction steps are performed by individual modules. Each module is able to read information from the detector description and/or the event, process the information and write the results into the event structure. Communication between the modules occurs only through the event structure (taken from [53]).

Once performed, the calibration provides an energy measurement using SD only with a duty cycle of about 100%.

## 5.5   Software and Data Storage

### 5.5.1   Root

The ROOT system[6], based on the object-oriented programming language C++, represents a framework to handle and analyse large amounts of data. Treating the input data as objects, the framework provides a huge amount of methods, i.e.: Histograms of arbitrary dimension, function evaluation, curve fitting, minimization, graphics and visualization classes and many more. Analysed data can be written in so-called trees to achieve an object-oriented storage structure. In this thesis ROOT 5.22 has been used.

### 5.5.2   Offline

The data analysed in this thesis have been reconstructed with the $\overline{\mathrm{Off}}\underline{\mathrm{line}}$ framework [52]. The underlying principle of this software is breaking simulation and reconstruction tasks down to individual *modules* as illustrated in Fig. 5.10. Each module is able to read from the detector description and/or the event, process the information and write the results back into the event. The *detector description* contains information about the detector performance and configuration. The *event* facilitates the communication between the modules that are sequenced by a run controller and finally the output of this procedure

---

[6] *http://root.cern.ch*

can be stored partly or completely in various data formats.

The $\overline{\text{Off}}\underline{\text{line}}$ framework provides a large set of basic reconstruction and simulation modules. Individual modules can be written and the module sequence can be defined by the user, gluing a subset of modules together in a specific order. The output of the reconstruction can be completely controlled by the user.

A typical reconstruction folder contains three essential files in addition to a makefile, usually named: `ModuleSequence.xml`, `EventFileReader.xml` and `bootstrap.xml`.

The input data format and the input files are specified in the *EventFileReader* xml-card (steering a module of the same name containing the source code) in order to interpret its structure correctly. The *RunController* receives the sequence from a *ModuleSequence* that contains mainly a loop over a series of different modules. If output data shall be stored, an appropriate module, i.e. the *RecDataWriter* module, must be included at the end of the sequence. A *bootstrap* links to all needed configuration files, using config ID's to handle them internally, and thus must contain the paths to all modules being used, at minimum the *ModuleSequence* and the *EventFileReader*. $\overline{\text{Off}}\underline{\text{line}}$ provides a large set of xml-cards as configuration devices for related modules.

Those cards can be overridden by a changed card and new xml-cards can be added by copying it into the reconstruction folder and linking it in the *bootstrap.*

After typing `make` in the command line the executable `userAugerOffline` can be run by the following command line

```
userAugerOffline -b bootstrap.xml
```

Datasets of various reconstructions with sets of rather common models implemented in terms of modules are uploaded regularly on a webpage[7]. For this thesis I used Golden Hybrid data of this source, reconstructed with $\overline{\text{Off}}\underline{\text{line}}$ version `v2r5p6` based on the module sequence given in Fig. 5.4, as far as nothing else is mentioned. The set of config files can be found in `share/auger-offline/config/observerConfiguration.xml` and the Observer reconstruction folder is `StandardApplications/Observer`, containing all needed files to perform a Golden Hybrid reconstruction.

### 5.5.3 ADST

Before the ADST data structure was developed [54], reconstructed data had been stored in `ASCII` files, providing only separate information of the detector-subsystems of the Pierre Auger Observatory. The ADST file format is based on `ROOT`, containing SD and FD event variables. The name is an abbreviation for "Advanced Data Summary Tree", providing a branching structure that contains all reconstructed quantities together with the internal relations needed for physics analysis. Thus ADST files can be inspected interactively using `ROOT`. The overall structure of event variables in ADST, inherited in a class called *RecEvent*, is sketched in Fig. 5.11. Detailed information are provided in the manual [54]. For this thesis `ADST` version `v5r2p2_pozzo` has been used.
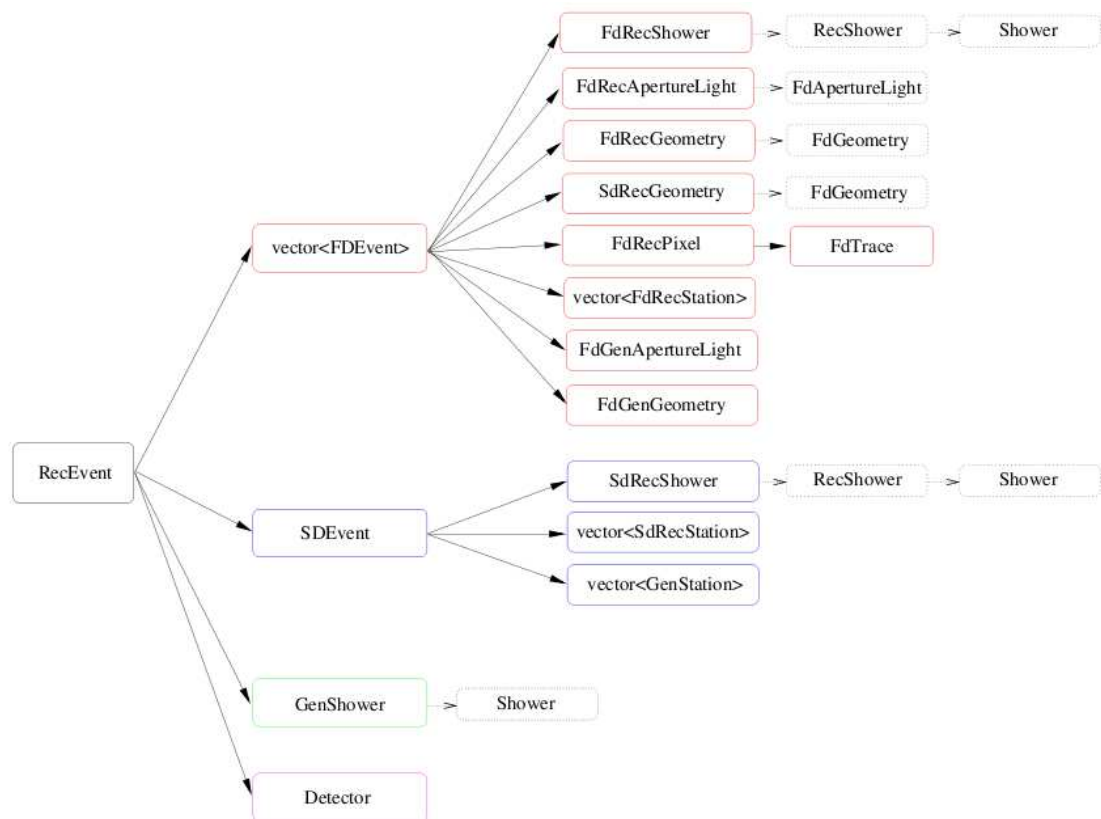
---

[7]*http://augerobserver.fzk.de*

**Figure 5.11:** The *RecEvent* class structure. Solid arrows indicate a "has a" relationship, dotted arrows signalize an "is a" relationship (from [54]).

# Chapter 6

# Evaluation of Fit Results

The probability of a fit to describe a distribution correctly can be analysed by two essential quantities, $\chi^2$ and $N_{\mathrm{dof}}$. The $\chi^2$ of a distribution with $N_{\mathrm{Data}}$ data points is defined as:

$$\chi^2 = \sum_{i=1}^{N_{\mathrm{Data}}} \left( \frac{x_i - x_{i,\mathrm{Fit}}}{\sigma_i} \right)^2 \tag{6.1}$$

where $x_i$ is the $i$th data point, $x_{i,\mathrm{Fit}}$ the related value of the fit and $\sigma_i$ the error of the data point. The number of degrees of freedom is defined as $N_{\mathrm{dof}} = N_{\mathrm{Data}} - N_{\mathrm{Fit}}$. Based on those parameters, the probability distribution of a $\chi^2$ as a consequence of statistical uncertainties, related to a given $N_{\mathrm{dof}}$, can be calculated:

$$f(x) = \frac{1}{2^{N_{\mathrm{dof}}/2} \cdot \Gamma(N_{\mathrm{dof}}/2)} \cdot x^{N_{\mathrm{dof}}/2-1} \cdot \exp(-x/2) \tag{6.2}$$

where $x$ substitutes the $\chi^2$. $N_{\mathrm{dof}}$ is the $\chi^2$ related to the maximum of this distribution. The skewness $\gamma$ of a probability distribution of a quantity $x$ measures the asymmetry of the distribution. For a $\chi^2$-distribution an essential relation is:

$$\gamma(x) \propto \frac{1}{\sqrt{N_{\mathrm{dof}}}} \tag{6.3}$$

A sketch of $\chi^2$-distributions for different $N_{\mathrm{dof}}$ is given in Fig. 6.1. The $\chi^2$-distribution is asymmetric for $N_{\mathrm{dof}} < 35$. Around this value it becomes rather symmetric. According to Eq. 6.2, the limit of a $\chi^2$-distributions for large $N_{\mathrm{dof}}$ is a Gaussian distribution (see also [62], p. 107). The fit quality can be guessed from a comparison of the magnitudes of $\chi^2$ and $N_{\mathrm{dof}}$, which should be approximately the same. A calculation of the fit probability is obtained from integrating the $\chi^2$-distribution from the measured $\chi^2$ to infinity. It gives the probability of an even larger $\chi^2$ due to statistical uncertainties. In this context a probability of 0.5 represents the highest probability.

The definition of confidence intervals is defined based on a Gaussian distribution. Thus for small $N_{\mathrm{dof}}$ it is difficult to define a fit probability in terms of a confidence interval. For asymmetric distributions the fit probability represents a lower limit on the true probability that takes both sides of the distribution into account.
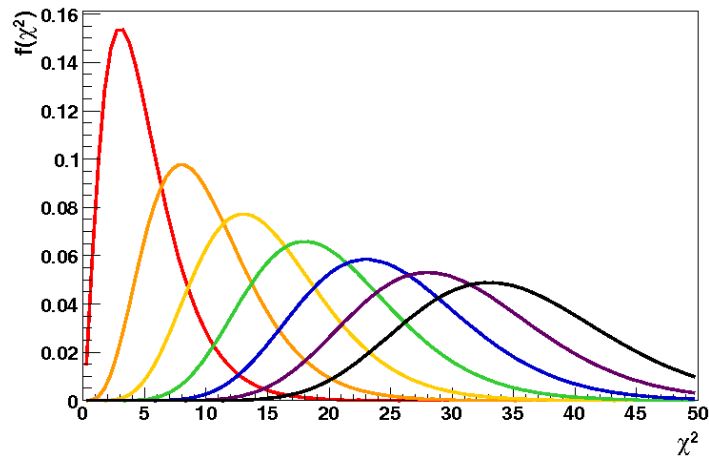
**Figure 6.1:** $\chi^2$-distributions for different $N_{\text{dof}}$, representing the $\chi^2$ related to the maximum of each distribution. The $N_{\text{dof}}$ of the black curve is 35.

# Chapter 7

# Accuracy of the Reconstructed Shower Axis

An accurate reconstruction of the shower direction is required by the direct search for point sources on one hand and all kinds of anisotropy studies on the other hand. The present analyses aim to investigate the angular resolution of the different detector systems and its variation with time. Moreover, the Hybrid angular resolution of each individual eye is estimated.

A common way to derive a resolution is a comparison between injected (true) and reconstructed data using simulations. The key quantity for angular resolution studies is the so-called *space angle*. It is defined as the opening angle between two shower axes, carrying information about the accuracy of the reconstructed shower direction. The direction of a shower axis can be parametrized in spherical coordinates in terms of zenith angle $\theta$ and azimuth angle $\phi$ (see Fig. 7.2) via

$$\vec{x} = \begin{pmatrix} \cos(\phi)\sin(\theta) \\ \sin(\phi)\sin(\theta) \\ \cos(\theta) \end{pmatrix} \tag{7.1}$$

where $\theta \in [0, \frac{\pi}{2}]$ and $\phi \in [0, 2\pi]$ (counterclockwise).

Given two axes of unit vectors $\vec{x_1}$ and $\vec{x_2}$, the intermediate space angle $\Delta_{1,2}$ is

$$\Delta_{1,2} = \arccos\left(\vec{x_1} \cdot \vec{x_2}\right) \tag{7.2}$$

The angular resolution is commonly defined as the the 68% quantile $\Delta^{68}$ of the space angle distribution between true and reconstructed axis, using simulations (cf. [55], [56]). This angle[1] $\sigma^{68}$ thus contains 68% of the events coming from a given direction. The extracted angular resolution depends on the underlying simulations.

As only real data will be used for all present analyses, the angular resolution is estimated

---

[1]From now on the symbol $\sigma$ will be used to represent the angular resolution and $\sigma^{\mathrm{M}}$ to represent its estimation by a method M. The estimator related to the 68% quantile method thus is $\sigma^{68} \doteq \Delta^{68}$.
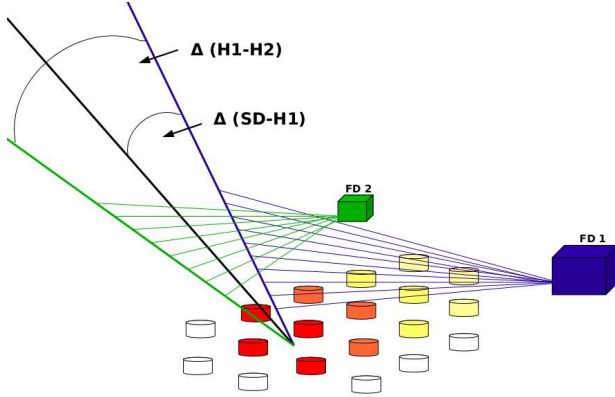
**Figure 7.1:** Reconstructed shower axes and space angles $\Delta$ of a Golden Hybrid Stereo event, shifted into a common impact point on the ground. The colors of the SD array represent the temporal development of the shower signal on the ground, from red to yellow. The indices $H$ and $SD$ represent the Hybrid-reconstructed and the SD-reconstructed shower axes respectively.
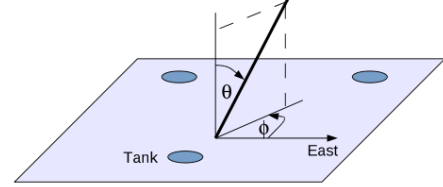
**Figure 7.2:** The shower direction is parametrized by SD-related spherical coordinates *zenith angle* $\theta$ and *azimuth angle* $\phi$. (Taken from [56])

by the 68% quantile of the space angle distribution between different types[2] of reconstructed axes. This means that 68% of the events have a space angle smaller than $\sigma^{68}$. The overall angular resolution is assumed to be the geometric mean of SD and Hybrid angular resolution, yielding the basic relation

$$\sigma_{\mathrm{SD,H}}^2 = \sigma_{\mathrm{SD}}^2 + \sigma_{\mathrm{H}}^2 \quad \Leftrightarrow \quad \sigma_{\mathrm{SD}} = \sqrt{\sigma_{\mathrm{SD,H}}^2 - \sigma_{\mathrm{H}}^2} \tag{7.3}$$

The indices indicate comparisons between the reconstructed axes using particular detector systems, as sketched in Fig. 7.1. The overall angular resolution $\sigma_{\mathrm{SD,H}}$ is derived from the space angle distribution between SD- and Hybrid-axis[3]. The Hybrid angular resolution $\sigma_{\mathrm{H}}$ is derived from the space angle distribution between the Hybrid-axes of two different triggered eyes, dividing the resulting estimator by a factor $\sqrt{2}$ in order to obtain the resolution related to one eye. The estimation of $\sigma_{\mathrm{H}}$ obviously requires stereo events. The remaining SD angular resolution $\sigma_{\mathrm{SD}}$ is calculated from both quantities, applying Eq. 7.3. In order to check the results and to diversify the analysis, complementary methods are tested in addition to the general 68% quantile method (see Section 7.3).

---

[2]Details about the underlying SD and Hybrid reconstruction are given in Sections 5.1 and 5.2 respectively.

[3]The Hybrid-reconstructed shower axis is called 'Hybrid-axis' from now on.

# 7.1 Cuts and dataset

Reconstructed Golden Hybrid Stereo data from January 1st, 2004 to April 28th, 2009, downloaded from the Auger Observer webpage[4], have been used for all presented angular resolution analyses. The reconstruction has been done with $\overline{\text{Off}}\underline{\text{line}}$ version `v2r5p6` and the module sequence sketched in Fig. 5.4.

Golden Hybrid data contain Hybrid events with at least three triggered SD tanks, providing a full Hybrid reconstruction together with a full, independent SD reconstruction. Details about the particular reconstructions are given in Chapter 5. The quality of the geometry reconstruction is given by the quality of SDP- and time-fits and the space-time compatibility between the hottest tank and the FD telescope.

All cuts have been taken from [55], composing a set of *basic cuts* that can be extended depending on the used dataset. They have been defined by the angular resolution working group [57].

- A reconstructed FD- and SD-axis ($\leftrightarrow$ both rec-levels $> 4$)

- SDP fit $\chi^2/N_{\text{dof}} < 7$

- Time fit $\chi^2/N_{\text{dof}} < 8$

- Distance between hottest tank and axis $< 2000$ m

- |SD-FD time offset| $< 200$ ns

A *high quality* can be achieved applying a further cut that restricts the selected events to a minimum angular track length observed by FD:

- FD Angular tracklength $> 15°$

Using *Golden Hybrid* events, the following cuts are recommended:

- $\log_{10}(E_{\text{FD}}/[\text{eV}]) > 18.5$, according to the efficiency of Hybrid detection

- Exclude SD bad periods

As the estimation of the Hybrid resolution requires *stereo* events, two further cuts have been applied:

- Number of SDP pixels $> 5$

- At least two remaining eyes after application of all cuts

---

[4]*http://augerobserver.fzk.de*

For the sake of completeness the energy $E$, its uncertainty $\Delta E$, $\chi_0$ and $R_p$ are required to be greater than zero. The high quality cut selects events with a mean space angle smaller than 1.5° (see Fig. A.1 and A.2 in the appendix) that is rather constant as a function of angular track length.

The basic cuts are passed by 5739 out of 77144 Golden Hybrid events. Of these, about 69% pass the high quality cut and another 99% pass the second Golden Hybrid cut. The stereo cut reduces the statistics to 228 events and, finally, 185 events remain after applying all cuts, including the Loma Amarilla bad period cut introduced in Section 7.2. The remaining dataset contains 5 triple events and 180 stereo events.

To determine $\sigma_{SD,H}$ every eye is interpreted as a single event, yielding 375 data points. For the determination of $\sigma_H$ every permuting pair of eyes is interpreted as a single event, yielding 195 data points.

As no parameter has been fixed in the analyses because of rather low statistics, the results represent a superposition of various dependences. The impact points of the SD shower axes on the ground are illustrated in Fig. 7.3. Due to the fact that almost 10 months of Loma Amarilla data have been rejected in the selected dataset, fewer impact points are located near Loma Amarilla. Stereo events are most frequently found near the center between two neighbouring eyes and, consequently, most triple and quadrupole events near the center of the SD array. Thus the highest statistics have been observed on a cross-like structure that vanishes near Loma Amarilla. Stereo events cause a bias to larger core-eye-distances and, accordingly, to higher energies (see Fig. 7.5 and 7.6). As the angular track length decreases as a function of core-eye-distance for a fixed energy, all lower energetic showers with an angular tracklength $< 15°$ are rejected by the high quality cut.

In addition to this there are detector-related effects and dependences. The closer a shower of fixed energy moves relative to a telescope, the faster the light spot propagates through the field-of-view of the camera and the less precise the geometry reconstruction gets. With increasing core-eye-distances the effect of atmospheric scattering on the FD measurement gets more intense. The accuracy of the SD reconstruction is influenced by the tank multiplicity. The SD angular resolution improves with increasing multiplicity and, with regard to other analyses [55, 56], in particular for more than five tanks. The multiplicity ranges from three to 28 tanks, yielding an average of 11 SD tanks and 10 events with less than six tanks (see Fig. 7.4 in the appendix).

In conclusion, $\sigma_H$ is expected to be rather constant as function of energy while $\sigma_{SD}$ is expected to improve.

## 7.2 Variation of the overall angular resolution with time

The time constancy of the angular resolution is an important issue concerning the detector performance, which is preceding anisotropy and correlation analyses. A change of the
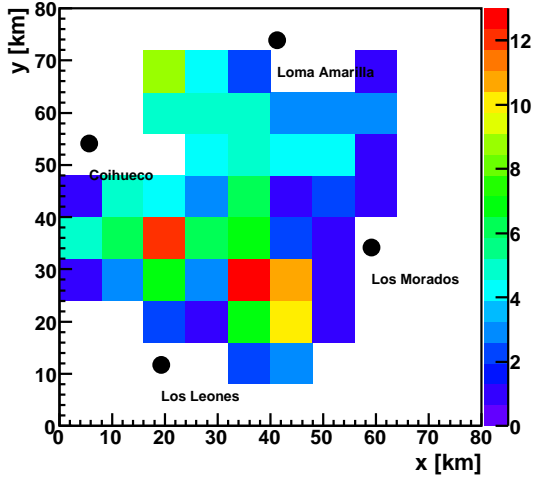
**Figure 7.3:** Impact points of the SD-reconstructed shower cores of the 185 selected events in units of the detector coordinate system.
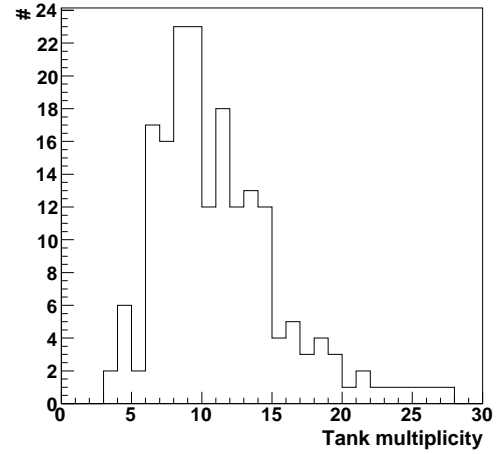


**Figure 7.4:** Distribution of the tank muliplicity, yielding on average 11 tanks and 10 events with less than six tanks.
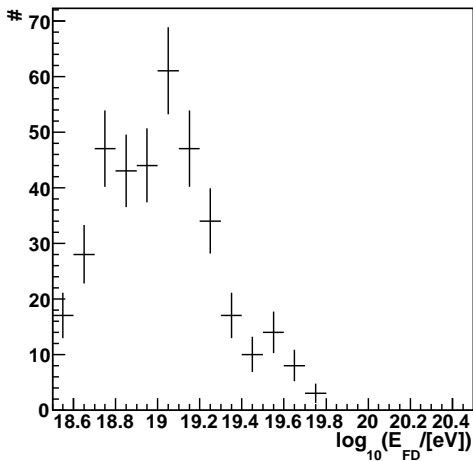


**Figure 7.5:** Hybrid energy distribution of the 375 selected data points, interpreting every eye as a single event. Error bars: $\sqrt{N}$
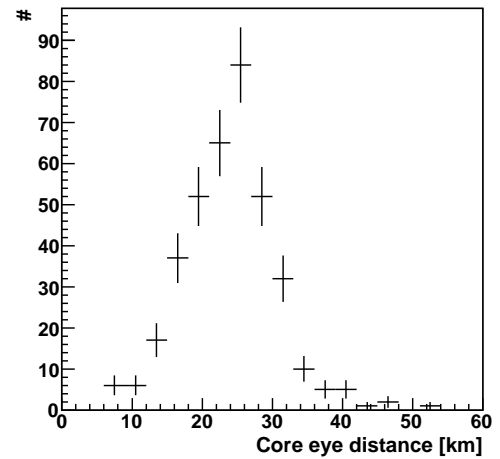


**Figure 7.6:** Distribution of the core-eye-distances of the 375 selected data points, interpreting every eye as a single event. Error bars: $\sqrt{N}$

directional reconstruction accuracy influences the uncertainties of all these analyses.
In this section an analysis of the variation of the overall angular resolution $\sigma_{\mathrm{SD,H}}$ with time is presented, comparing two time periods arising from AGN correlation analyses (cf. [58]):

**Period 1:** January 1st, 2004 - August 31st, 2007 (Known as periods I + II)
**Period 2:** September 1st, 2007 - April 28th, 2009

As mentioned before, $\sigma_{\mathrm{SD,H}}$ is estimated by the 68% quantile of the distribution of the space angle between SD- and Hybrid-axis. In order to analyse a more common dataset, the stereo cuts have been ignored. At first the analysis has been done without the bad period cut.
The resulting $\sigma_{\mathrm{SD,H}}^{68}$ of the entire detector is 1.29° for the first and 1.45° for the second period. After several improvements of the detectors during operation one would intuitively expect the detector to resolve smaller angles in the second period or expect at least a resolution similar to the one of the first period. In order to understand how $\sigma_{\mathrm{SD,H}}^{68}$ is composed of individual eyes, the overall angular resolution related to the particular eyes have been estimated for the first and the second period. The angular resolution of Loma Amarilla degrades by about 25% from 1.88° in the first period to 2.35° in the second period and the angular resolution of Los Morados degrades by approximately 8% from 1.14° to 1.22° while the resolutions of the remaining eyes improve.
A reason for the degrading angular resolution of Loma Amarilla has been found. From 2nd February until October 30th, 2008 GPS-timing problems[5] appeared at Loma Amarilla. Within the bad period the GPS time offset between SD and FD of Loma Amarilla covers a few thousand ns, compared to Los Leones showing a spread over a few hundred ns (Fig. A.3, A.4, appendix).
$\sigma_{\mathrm{SD,H}}^{68}$ has been estimated a second time, excluding Loma Amarilla measurements of that bad period, as listed in Table 7.1. Los Leones has the highest statistics in the first period with about 36% of all events since it was in operation first. Regarding the full period (periods 1+2), the deviations of the angular resolution of the individual eyes from the entire detector reach from -12% at Los Leones up to 43% at Loma Amarilla. Improving angular resolution from the first to the second period have been observed for all eyes except of Los Morados. The overall angular resolution of the entire detector of about 1.28° is similar in both periods.
The same analysis has been done for the fully restricted Golden Hybrid Stereo dataset that is essential for the estimation of $\sigma_{\mathrm{SD}}$ in Section 7.3. The results are listed in Table 7.2. The overall angular resolution of the entire detector improves from 1.19° the first to 1.09° in the second period. Regarding Los Morados, a degrading resolution has been observed. The maximum deviations of the individual resolutions from the entire detector in the full period are found between Loma Amarilla - Los Morados ($\sim 51\%$) and Loma Amarilla - Los Leones ($\sim 65\%$). As Los Morados and Loma Amarilla are neighbouring eyes, they measure a couple of multi-eye events simultaneously.
As $\sigma_{\mathrm{SD,H}}$ is composed by two quantities, $\sigma_{\mathrm{SD}}$ and $\sigma_{\mathrm{H}}$, the question is, which of the two

---

[5]Details can be found on *http://www.physics.adelaide.edu.au/∼jbellido/Auger/LA/*

| $\sigma_{\mathrm{SD,H}}^{68}[°]$ | Period 1 | # | Period 2 | # | Periods 1+2 | # |
|---|---|---|---|---|---|---|
| LL | 1.174 (-8.9%) | 739 | 1.036 (-19.0%) | 396 | 1.138 (-11.5%) | 1135 |
| LM | 1.139 (-11.6%) | 570 | 1.224 (-4.3%) | 500 | 1.169 (-9.1%) | 1070 |
| LA | 1.877 (+45.7%) | 120 | 1.798 (+40.6%) | 290 | 1.842 (+43.2%) | 410 |
| Co | 1.438 (+11.6%) | 651 | 1.214 (-5.1%) | 567 | 1.345 (+4.6%) | 1218 |
| PAO | 1.288 | 2080 | 1.279 | 1753 | 1.286 | 3833 |

**Table 7.1:** Variation of $\sigma_{\mathrm{SD,H}}^{68}$ with time, applying bad period cut on Loma Amarilla and ignoring all kinds of stereo cuts. The percentual deviations from the angular resolution of the entire detector (PAO) are given in braces.

| $\sigma_{\mathrm{SD,H}}^{68}[°]$ | Period 1 | # | Period 2 | # | Periods 1+2 | # |
|---|---|---|---|---|---|---|
| LL | 1.021 (-14.0%) | 53 | 0.813 (-25.2%) | 59 | 0.884 (-19.8%) | 112 |
| LM | 0.987 (-16.8%) | 38 | 1.089 (+0.2%) | 61 | 1.042 (-5.4%) | 99 |
| LA | 1.672 (+40.9%) | 12 | 1.586 (+45.9%) | 53 | 1.600 (+45.2%) | 65 |
| Co | 1.388 (+16.9%) | 39 | 1.104 (+1.6%) | 60 | 1.185 (+7.5%) | 99 |
| PAO | 1.187 | 142 | 1.087 | 233 | 1.102 | 375 |
| PAO (-LA) | 1.146 | | 0.889 | | 1.007 | |
| $\sigma_{\mathrm{H}}^{68}[°]$ | Period 1 | # | Period 2 | # | Periods 1+2 | # |
| PAO | 0.985 | 74 | 0.993 | 121 | 0.986 | 195 |
| PAO (-LA) | 0.954 | 62 | 0.730 | 66 | 0.883 | 128 |

**Table 7.2:** Variation of $\sigma_{\mathrm{SD,H}}^{68}$ and $\sigma_{\mathrm{H}}^{68}$ with time, applying bad period cut on Loma Amarilla. The percentual deviations from the angular resolution of the entire detector (PAO) are given in braces. Related plots are listed in the appendix (Fig. A.5, A.6). The abbreviation '-LA' means excluding Loma Amarilla completely.

causes the observed deviations. Due to the fact that at least one triggered telescope and three triggered tanks are required for a Golden Hybrid geometry reconstruction, the SD angular resolution represents an average of all triggered tanks while the Hybrid angular resolution is related to one single eye. Therefore, $\sigma_{\mathrm{SD}}$ should be rather equal for all SD tanks and the differences in the $\sigma_{\mathrm{SD,H}}$ of individual eyes should mainly arise from the telescopes.

The low statistics of high quality Golden Hybrid Stereo events is not sufficient to analyse the Hybrid angular resolution of each individual eye. The average Hybrid resolution $\sigma_{\mathrm{H}}$ has been estimated for both periods, including and excluding data of Loma Amarilla (see Table 7.2). Including Loma Amarilla, the Hybrid angular resolution of the entire detector does not change significantly from the first to the second period. Excluding Loma Amarilla, it increases from 0.95° to 0.73°. Thus it shows a similar time dependence as $\sigma_{\mathrm{SD,H}}^{68}$ which supports the assumption of a comparatively constant $\sigma_{\mathrm{SD}}^{68}$. The exclusion of Loma Amarilla yields an improvement of about 0.1° from 0.99° to 0.88° regarding the full period.

## 7.2.1 Summary and outlook

Both datasets[6] show a similar behaviour. Loma Amarilla has the worst resolution in all periods and for both datasets, even after applying the bad period cut. Its average deviation from the overall angular resolution of the entire detector exceeds 40%. The calibration and a correct cabling of the photomultipliers (PMT) in the FD cameras influence the accuracy of the SDP reconstruction (see Section 5.2). As the calibration of the PMT at Loma Amarilla is preliminary and some PMT are miscabled, the geometry reconstruction accuracy of Loma Amarilla has not been optimized yet, yielding a worse FD and Hybrid angular resolution. A reason for the degrading angular resolution of Los Morados could not be found.

The overall angular resolution of the entire detector equals approximately $1.28°$ in both periods in case of ignoring the stereo cuts. For the fully restricted dataset it improves slightly from $1.19°$ to $1.09°$. The average overall angular resolution of the entire detector regarding the full period yields $1.29°$ without and $1.10°$ with stereo cuts.

Due to still scarce statistics of high quality stereo events it is not possible to distinguish between eyes in particular time periods. The variation of $\sigma_\mathrm{H}^{68}$ of the entire detector with time has been analysed, yielding a result similar to the one of $\sigma_\mathrm{SD,H}^{68}$. This indicates a rather constant $\sigma_\mathrm{SD}^{68}$. Excluding Loma Amarilla, the overall angular resolution and the Hybrid angular resolution improve significantly by about 23%. The absolute values are topic of Section 7.3. As soon as sufficient statistics of measured Golden Hybrid Stereo data are available, an analysis similar to the present one could be performed to investigate the time constancy of $\sigma_\mathrm{H}$ of the entire detector and individual eyes.

## 7.3 Estimation of the SD angular resolution

In this section an estimation of the SD angular resolution $\sigma_\mathrm{SD}$ is presented as a complementary analysis to simulation-based approaches. As no simulations are used, one has to find an appropriate method for the estimation of the individual resolutions, as explained in the beginning of this chapter. The universal estimator of the angular resolution is again the 68% quantile of the space angle distribution and the basic relation is given by Eq. 7.3. The dataset has been selected by applying the complete set of cuts together with the Loma Amarilla bad period cut. In order to compare and evaluate the results, further estimation methods will be applied, assuming the space angles to be Rayleigh-distributed. If a two-dimensional vector contains two Gaussian-distributed components of equal $\sigma$, the vector's length is Rayleigh-distributed. Transfering this to a simultaneous measurement by two detectors that measure shower directions following a Gaussian distribution, the space angle $\Delta$ is Rayleigh-distributed in case of equal $\sigma$ (or rather angular resolutions) for both detectors:

---

[6]One dataset has been selected by applying the complete set of cuts. A second, more general dataset has been selected relieving the stereo cuts.

$$\text{Rayleigh}(\Delta) = \frac{\Delta}{\sigma^2} \cdot e^{-\frac{\Delta^2}{\sigma^2}} \tag{7.4}$$

A fit of a Rayleigh-distribution with the function $f(\Delta) = c \cdot \Delta \cdot e^{-\frac{\Delta^2}{\sigma^2}}$ approximates the distribution and its $\sigma$ quite exactly. The resulting $\sigma^{\text{Ray}}$ of the space angle distributions is interpreted as the angular resolution of each of two detectors.

There are two estimators for the $\sigma^{\text{Ray}}$ of a Rayleigh distribution related to the mean and the variance of the distribution:

$$\sigma^{\text{Mean}} = \sqrt{\frac{2}{\pi}} \cdot \text{Mean} \pm \sqrt{\frac{2}{\pi}} \cdot \frac{\text{RMS}}{\sqrt{N}} \tag{7.5}$$

$$\sigma^{\text{Var}} = \sqrt{\frac{2}{4-\pi}} \cdot \text{Var} = \sqrt{\frac{2}{4-\pi}} \cdot \text{RMS} \tag{7.6}$$

The square root of the variance equals the RMS of a distribution, as indicated by the error bars of the mean profile. In case of assuming the overall angular resolution $\sigma_{\text{SD,H}}$ to be Rayleigh-distributed, the related estimators must be multiplied by a factor $\sqrt{2}$ in order to obtain the overall angular resolution of both detector systems.

In principle the present analysis can be split into two parts: An estimation of the all energy angular resolution and an estimation of the angular resolution as a function of energy.

## 7.3.1 All energy angular resolution

The distribution of the average space angle between two Hybrid-axes for all energies ranging from $10^{18.5}$ eV to $10^{19.7}$ eV, $\Delta_{\text{H1}-\text{H2}}$, is skeched in Fig. 7.7. The full red line represents the cumulative distribution and the dashed red lines mark its 68% quantile. In order to obtain the angular resolution related to one eye, the estimator is divided by a factor $\sqrt{2}$. The resulting Hybrid angular resolution is $\sigma_{\text{H}}^{68} = 0.99°$. As all eyes have been mixed in this analysis, this result represents an average over all eyes.

Assuming the angular resolution of all eyes to be equal, which is of course just an approximation, the distribution has been fitted with a Rayleigh function. The plot together with its fit result is given in Fig. 7.8, yielding $\sigma_{\text{H}}^{\text{Ray}} = 0.92° \pm 0.04°$. The fit result approximately supports the assumption of a Rayleigh distribution, knowing that the angular resolution of individual eyes differ slightly. Moreover, the small $N_{\text{dof}}$ means an asymmetric $\chi^2$-distribution (cf. Chapter 6). Thus the fit probability represents a lower limit on the true probability that takes both sides of the $\chi^2$-distribution into account. The estimators regarding mean and variance of the distribution are $\sigma_{\text{H}}^{\text{Mean}} = 0.91° \pm 0.04°$ and $\sigma_{\text{H}}^{\text{Var}} = 0.98°$.

The same procedure has been applied to the distribution of the space angle between SD- and Hybrid-axis, $\Delta_{\text{SD,H}}$. In Fig. 7.9 the space angle distribution together with its cumulative distribution and its 68% quantile (dashed lines) are given, yielding $\sigma_{\text{SD,H}}^{68} = 1.10°$.
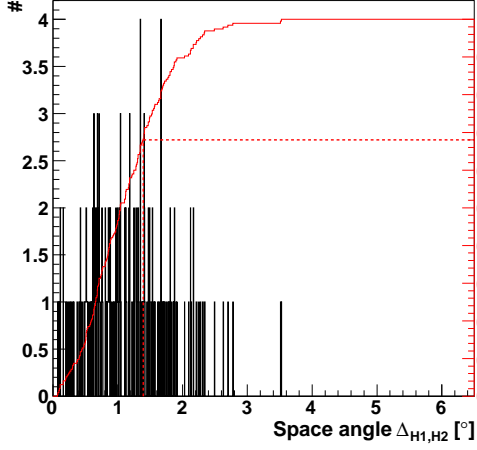
**Figure 7.7:** Estimation of the Hybrid angular resolution $\sigma_H$ using the 68% quantile of the space angle distribution: $\sigma_H^{68} = 0.99°$.
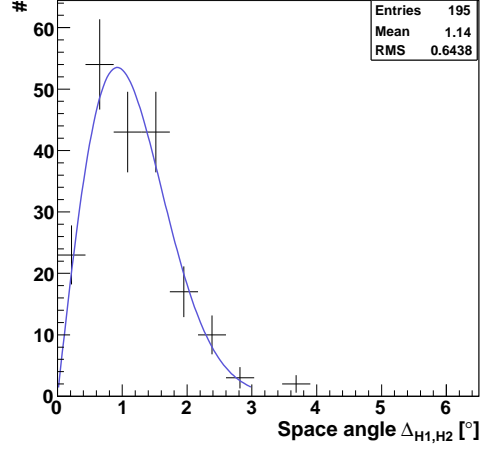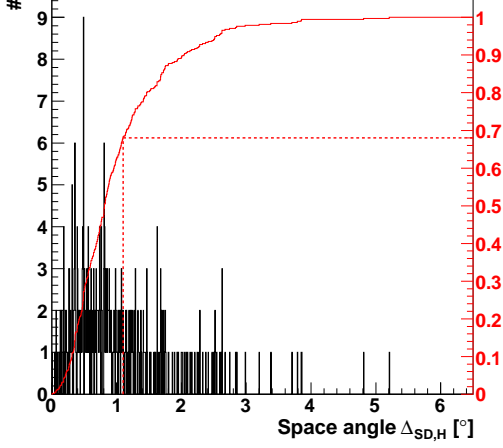
**Figure 7.8:** Estimation of the Hybrid angular resolution $\sigma_H$ by means of a Rayleigh fit ($\chi^2 = 4.43$, $N_{dof} = 5$). Error bars: $\sqrt{N}$.

|  | $\sigma_H[°]$ | $\sigma_{SD,H}[°]$ | $\sigma_{SD}[°]$ |
|---|---|---|---|
| 68% | 0.986 | 1.102 | 0.491° |
| Rayleigh | $0.921 \pm 0.039$ | $0.995 \pm 0.043$ |  |
| Mean | $0.910 \pm 0.037$ | $1.148 \pm 0.045$ |  |
| Variance | 0.983 | 1.654 |  |

**Table 7.3:** Estimation of angular resolutions by means of various methods. 68% of the distribution are universal, all other methods require a Rayleigh distribution. The Rayleigh-related estimators of $\sigma_{SD,H}$ have been multiplied by $\sqrt{2}$ to obtain the resolution of two detector systems.

Figure 7.10 shows the Rayleigh fit of the space angle distribution under the assumption of a Rayleigh-distribution. The fit result is not in agreement with this assumption. Thus the Gaussian-distributed directions of SD- and Hybrid-axis have two different $\sigma$. The resulting SD angular resolution, using the estimators $\sigma_{SD,H}^{68}$ and $\sigma_H^{68}$ together with Eq. 7.3, is $\sigma_{SD}^{68} = 0.49°$. All results are summarized in Table 7.3.

## 7.3.2 Angular resolution as a function of energy

This analysis is based on the distributions of the space angles as a function of energy. As a first step the Hybrid angular resolution $\sigma_H$ is analysed based on the space angle $\Delta_{H1,H2}$ between each two Hybrid-axes. Each point of the profile given in Fig. 7.11 represents the space angle containing 68% of the bin statistics at minimum. The error bars have been chosen to be the distance to the next lower and upper event, requiring three events per bin at minimum. A straight line fit has been applied, yielding the function

**Figure 7.9:** Estimation of the overall angular resolution $\sigma_{\mathrm{SD,H}}$ using the 68% quantile of the space angle distribution: $\sigma_{\mathrm{SD,H}}^{68} = 1.10°$.
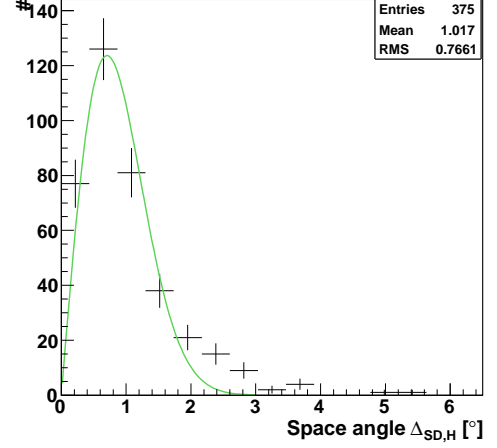
**Figure 7.10:** Estimation of the overall angular resolution $\sigma_{\mathrm{SD,H}}$ by means of a Rayleigh fit ($\chi^2 = 30.40$, $N_{\mathrm{dof}} = 5$). Error bars: $\sqrt{N}$.

$$\sigma_{\mathrm{H}}^{68}(E) = (1.003° \pm 0.006°) - (0.112° \pm 0.052°) \cdot (\log_{10}(E/[\mathrm{eV}]) - 18.5)$$

after dividing it by a factor $\sqrt{2}$ to obtain the angular resolution regarding one eye. The same procedure has been performed to the space angle distribution of $\Delta_{\mathrm{SD,H}}$ (see Fig. 7.12), yielding the function

$$\sigma_{\mathrm{SD,H}}^{68}(E) = (1.338° \pm 0.012°) - (0.347° \pm 0.025°) \cdot (\log_{10}(E/[\mathrm{eV}]) - 18.5)$$

$\sigma_{\mathrm{SD}}^{68}$ is derived from both functions, applying Eq. 7.3. Figure 7.13 depicts all results. $\sigma_{\mathrm{SD,H}}^{68}$ decreases from about 1.34° at $10^{18.5}$ eV to approximately 0.90° at $10^{19.7}$ eV. $\sigma_{\mathrm{SD,H}}^{68}$ decreases from about 1.00° at $10^{18.5}$ eV to approximately 0.90° at $10^{19.7}$ eV. $\sigma_{\mathrm{SD}}^{68}$ is derived from both functions, applying Eq. 7.3. It decreases from about 0.90° at $10^{18.5}$ eV to approximately 0.18° at $10^{19.7}$ eV. Figure 7.13 depicts all results.

Due to the low statistics of $\Delta_{\mathrm{H}}$, $\sigma_{\mathrm{H}}^{68}(E)$ has large statistical uncertainties that could be represented as a band around the fitted function. The slope is in agreement with zero within $2\sigma$ regarding the rather large slope parameter error. This uncertainty can also be seen in the large binning dependence of the slope, it varies from "slightly falling" to "constant". The angular resolution near the highly statistical center of the $x$-axis appears to be almost fixed, while the angular resolution near the borders fluctuates strongly as a consequence of decreasing statistics. These effects are mainly caused by a bias to larger distances and thus higher energies that is typical for stereo events. The statistics of the overall space angle distribution is about twice the Hybrid statistics and therefore $\sigma_{\mathrm{SD,H}}^{68}(E)$
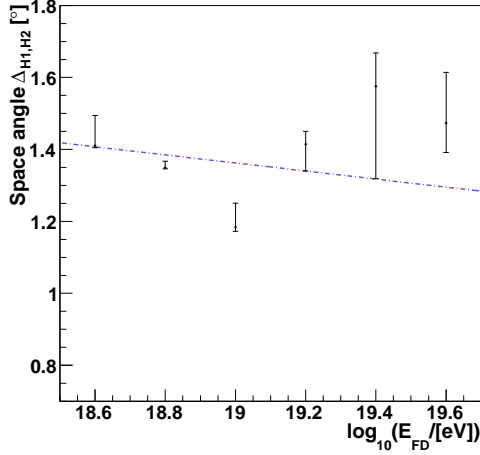
**Figure 7.11:** 68% quantile profile of the space angle $\Delta_{\mathrm{H1,H2}}$ between two Hybrid-axes as function of energy. Fit result: $\chi^2 = 18.13$, $N_{\mathrm{dof}} = 4$. Error bars: Next neighbour.
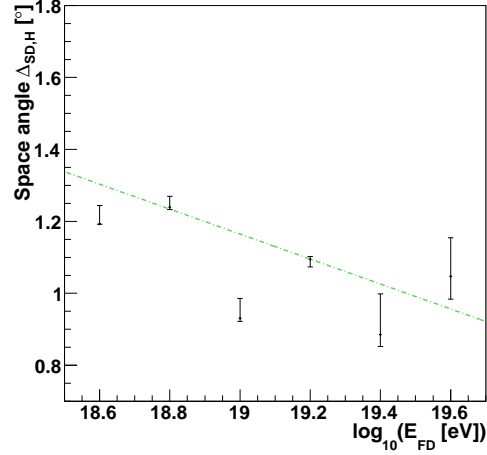
**Figure 7.12:** 68% quantile profile of the space angle $\Delta_{\mathrm{SD,H}}$ between SD- and Hybrid-axis as function of energy. Fit result: $\chi^2 = 26.95$, $N_{\mathrm{dof}} = 4$. Error bars: Next neighbour.

shows a better stability with a changing binning, i.e. giving always a negative slope. Thus the resulting $\sigma_{\mathrm{SD}}^{68}(E)$ depends on $\sigma_{\mathrm{H}}^{68}(E)$ and $\sigma_{\mathrm{SD,H}}^{68}(E)$, showing a variation of more than 50% at $10^{19.7}$ eV as a consequence of the uncertainties of $\sigma_{\mathrm{H}}^{68}(E)$. In case of $\sigma_{\mathrm{SD,H}}^{68} < \sigma_{\mathrm{H}}^{68}$ the result would be complex (statistical effect).

$\sigma_{\mathrm{H}}$ has been estimated a second time, assuming the space angle to be Rayleigh-distributed in each energy bin. The related mean profile plot together with a straight line fit and the fit result are given in Fig. 7.15. The resulting fit function, multiplied by $\sqrt{2/\pi}$ (see Eq. 7.5), is:

$$\sigma_{\mathrm{H}}^{\mathrm{Mean}}(E) = (0.949° \pm 0.007°) - (0.123° \pm 0.155) \cdot (\log_{10}(E/[\mathrm{eV}]) - 18.5)$$

In order to evaluate the results of the 68% quantile method, the mean method and the variance method all $\sigma_{\mathrm{H}}(E)$ estimators have been plotted in Fig. 7.16 for a comparison. They are consistent within 10% according to the relative deviations between mean and 68% as well as between variance and 68%, as depicted in Fig. 7.14. This result supports the approximation of $\Delta_{\mathrm{H1-H2}}$ by a Rayleigh distribution.

For the sake of completeness, the plots of the estimators of $\sigma_{\mathrm{SD,H}}(E)$ and $\sigma_{\mathrm{SD}}(E)$ related to the assumption of a Rayleigh-distribution of the space angle are listed in the appendix, in comparison to the estimators of the 68% quantile method (Fig. A.7 - A.10, appendix).
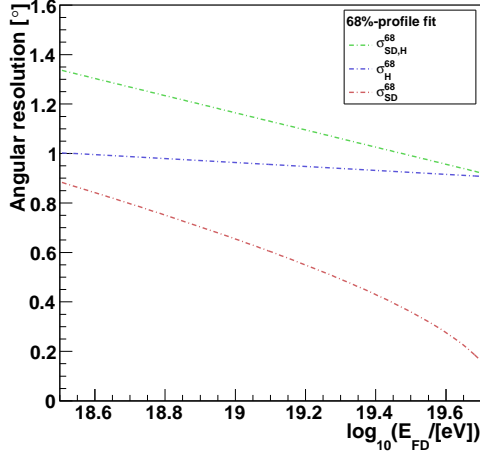
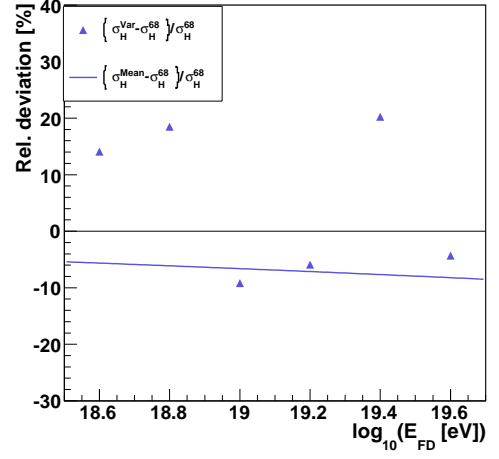**Figure 7.13:** Resulting angular resolution as function of energy, using the 68% quantile method.



**Figure 7.14:** Relative deviations of the estimation of $\sigma_H$ by means of various methods. Agreement within 10%.
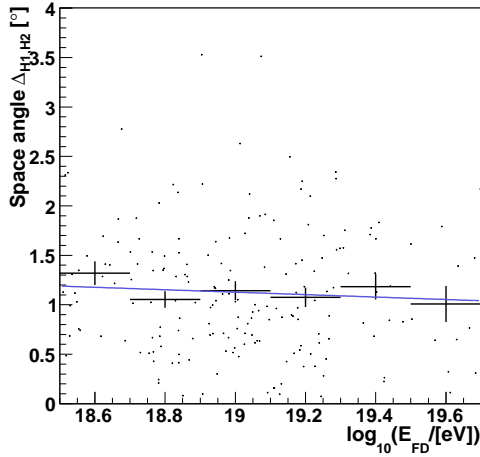


**Figure 7.15:** Space angle $\Delta_{H1,H2}$ between two Hybrid-axes as function of energy, superimposed with the (mean) profile plot. Fit result: $\chi^2 = 3.59$, $N_{\mathrm{dof}} = 4$. Error bars: RMS/$\sqrt{N}$.
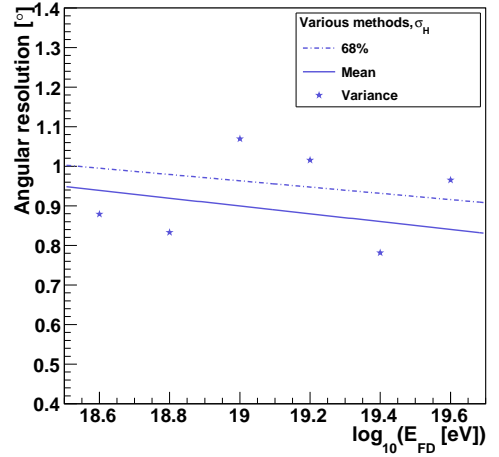


**Figure 7.16:** Comparison of the $\sigma_H$ estimators using the 68% quantile method, the mean method and the variance method. Agreement within 10%.

| $\sigma_{\mathrm{H}}[°]$ | Periods 1+2 |
|---|---|
| Los Leones | 0.736 (-25.4%) |
| Los Morados | 0.919 (-6.8%) |
| Loma Amarilla | 1.523 (+54.5%) |
| Coihueco | 1.079 (+9.4%) |
| PAO | 0.986 |

**Table 7.4:** Estimation of the Hybrid angular resolution $\sigma_{\mathrm{H}}$ of each individual eye, assuming a homogeneous SD angular resolution $\sigma_{\mathrm{SD}}^{68} = 0.491°$. The deviations of the individual eyes from the Hybrid resolution $\sigma_{\mathrm{H}}^{68}$ of the entire detector (PAO) are given in braces.

### 7.3.3 Estimating the Hybrid angular resolutions of each individual eye

Using the energy mean $\sigma_{\mathrm{SD}}^{68}$ resulting from this analysis together with the results of the previous analysis (see Table 7.2), one can derive the $\sigma_{\mathrm{H}}^{68}$ of each individual eye by adapting Eq. 7.3, assuming an approximately homogeneous $\sigma_{\mathrm{SD}}^{68}$. The results are listed in Table 7.4, yielding a spread of the individual resolutions between $0.74°$ and $1.52°$. The deviation of Loma Amarilla from the entire detector angular resolution by more than 50% is conspicuous. As mentioned in Section 7.2, the obvious deviation of Loma Amarilla from the mean Hybrid angular resolution may be caused by the preliminary calibration of its PMT and by miscabling. The assumption of equal angular resolutions for all eyes is obviously just a rough approximation.

The supporting fit result might be accidental, caused by advantageous statistics of individual eyes that let the superposition of four different space angle distributions look like one single Rayleigh distribution. The estimators of the 68% quantile method must be interpreted as an average.

Those results justify to exclude Loma Amarilla for the estimation of $\sigma_{\mathrm{SD}}(E)$ in order to compare it to the results obtained using simulations. Doing so, the all energy average[7] $\sigma_{\mathrm{H}}^{68}$ and the calculation of $\sigma_{\mathrm{H}}^{68}(E)$ for an energy $E = 10^{19}$ eV yield:

$$\sigma_{\mathrm{H}}^{68} = 0.88° \pm 0.04$$

$$\sigma_{\mathrm{H}}^{68}(10^{19} \text{ eV}) = 0.90° \pm 0.11°$$

where the error of $\sigma_{\mathrm{H}}^{68}$ has been estimated by 5% of the absolute value. The Hybrid angular resolution derived from the comparison of multi-eye events and simulated hybrid events at $E = 10^{19}$ eV is (cf. [55], p.11):

$$\sigma_{\mathrm{H}} = 0.89° \pm 0.04°$$

Both estimators of the present analysis are in good agreement with the simulation-based result.

---

[7]The average energy of the analysed interval ($\bar{E} \approx 10^{19.1}$ eV) is close to $10^{19}$ eV. Thus the energy-averaged estimator can be compared as well.

The analyses of this section have been redone parametrizing the shower direction in the equatorial coordinate system[8], yielding similar results.

## 7.3.4 Summary and outlook

The estimation of the angular resolutions as a function of energy as well as averaged over all energies have been performed successfully using Golden Hybrid Stereo events. The energy-averaged particular angular resolutions, estimated by the 68% quantile method, are $\sigma_{\mathrm{SD,H}}^{68} = 1.10°$, $\sigma_{\mathrm{H}}^{68} = 0.99°$ and $\sigma_{\mathrm{SD}}^{68} = 0.49°$. A fit of the distribution of the space angle $\Delta_{\mathrm{H1,H2}}$ between two Hybrid-axes with a Rayleigh function has successfully been performed, supporting the assumption of independent $\sigma$ that are equal in size. This result is possibly caused by an advantageous combination of statistics and $\sigma$. Nevertheless, the estimators related to the 68% quantile, the mean and the variance of the distribution are in good agreement. The assumption of a Rayleigh-distributed space angle $\Delta_{\mathrm{SD,H}}$ between SD- and Hybrid-axis is not supported by the fit result, as the SD and Hybrid angular resolution differ significantly.

Based on $\sigma_{\mathrm{SD,H}}^{68}$ of the individual eyes (see Section 7.2) and the mean $\sigma_{\mathrm{SD}}^{68}$, the Hybrid angular resolution of the individual eyes has been estimated successfully. The resulting Hybrid angular resolution of Loma Amarilla is approximately $\sigma_{\mathrm{H}}^{68} = 1.52°$, exceeding the average of the entire detector by more than 50%. The geometry reconstruction of Loma Amarilla has not been optimized yet as the calibration of the PMT is preliminary and some PMT are miscabled.

With regard to the angular resolution as a function of energy, the 68% quantile- and the Rayleigh-related estimators could as well be obtained from the one-dimensional space angle distributions within each energy bin.

In order to evaluate the presented results, comparisons have been drawn to simulation-based results (cf. [55]) excluding Loma Amarilla. This comparison yields a good agreement ($\sigma_{\mathrm{H}}^{68} = 0.88° \pm 0.04°$, $\sigma_{\mathrm{H}}^{\mathrm{sim}} = 0.89° \pm 0.04°$).

As mentioned in Section 7.3, error bands should be given together with all resulting angular resolution functions to illustrate the statistical uncertainties. Moreover, there may be a more appropriate definition for the error bars of an 68% quantile. These errors should be given together with all 68% estimators.

In order to compare the $\sigma_{\mathrm{SD}}$ estimators of the presented analyses with another method based on measured data only, the SD angular resolution could be estimated by a so-called *checkboard method*. This method subdivides the set of triggered SD tanks randomly into two sets of half the number of tanks, requiring a sufficient number of tanks. The distribution of the tank multiplicity of the present dataset is depicted in Fig 7.4 in the appendix. The SD geometry reconstruction would be performed independently by both sets of tanks, yielding two different SD reconstructed axes. $\sigma_{\mathrm{SD}}^{\mathrm{check,68}}$ would be a further

---

[8]Equatorial coordinate system: Azimuth angle $\alpha$, declination angle $\delta$.

|  | $CR_{\mathrm{H}}^{68}$ [km] |
|---|---|
| Los Leones | 0.23 |
| Los Morados | 0.33 |
| Loma Amarilla | 0.44 |
| Coihueco | 0.65 |
| PAO | 0.41 |

**Table 7.5:** Estimation of the reconstruction accuracy of the Hybrid shower core, assuming the SD shower core to approximate the true core. The accuracy is estimated for the individual eyes and for the entire detector (PAO).

estimator of the angular resolution of the surface detectors, related to the 68% quantile of the space angle distribution between both SD-axes.

## 7.4 Accuracy of Hybrid-reconstructed shower core

The absolute position of the shower axis is determined by the impact point of the shower axis on the ground, called *shower core*. The angular resolution does not contain information about the accuracy of this reconstructed shower core. Using Golden Hybrid data (see Chapter 5), the accuracy of the Hybrid-reconstructed shower core can be estimated by comparing the shower cores of Hybrid and SD reconstruction. Assuming the SD core to approximate the true core, the accuracy of the Hybrid core is estimated by the 68% quantile $CR_{\mathrm{H}}^{68}$ of the distribution of the distance $\Delta d$ between Hybrid and SD core. This means that 68% of the SD and Hybrid cores are closer to each other than $CR_{\mathrm{H}}^{68}$.

This analysis has been performed using again the fully restricted dataset of the full period (see Section 7.1). Every eye is interpreted as a single event, yielding 375 data points.

The resulting estimators $CR_{\mathrm{H}}^{68}$ are listed in Table 7.5. Related plots can be found in the appendix (see Fig. A.11).

The estimated mean accuracy of the Hybrid-reconstruced shower cores of the entire detector is 0.41 km. The accuracy of Los Morados and Loma Amarilla are close to this mean value with 0.33 km and 0.44 km respectively. The accuracy of Los Leones and Coihueco deviates from the mean accuracy. Los Leones has the best accuracy with 0.23 km and Coihueco the worst with 0.65 km. All of those estimators are approximately constant for both periods (see Section 7.2). The core distance in $x$- and $y$-direction for each individual eye is given in Fig. 7.17. The magnitude of the spread of each plot confirms the results related to the estimators. Moreover, $\Delta d$ has been analysed as a function of the distance $d$ between Hybrid core and eye. The mean $\Delta d$ increases as a function of core-eye-distance (see Fig. 7.18).
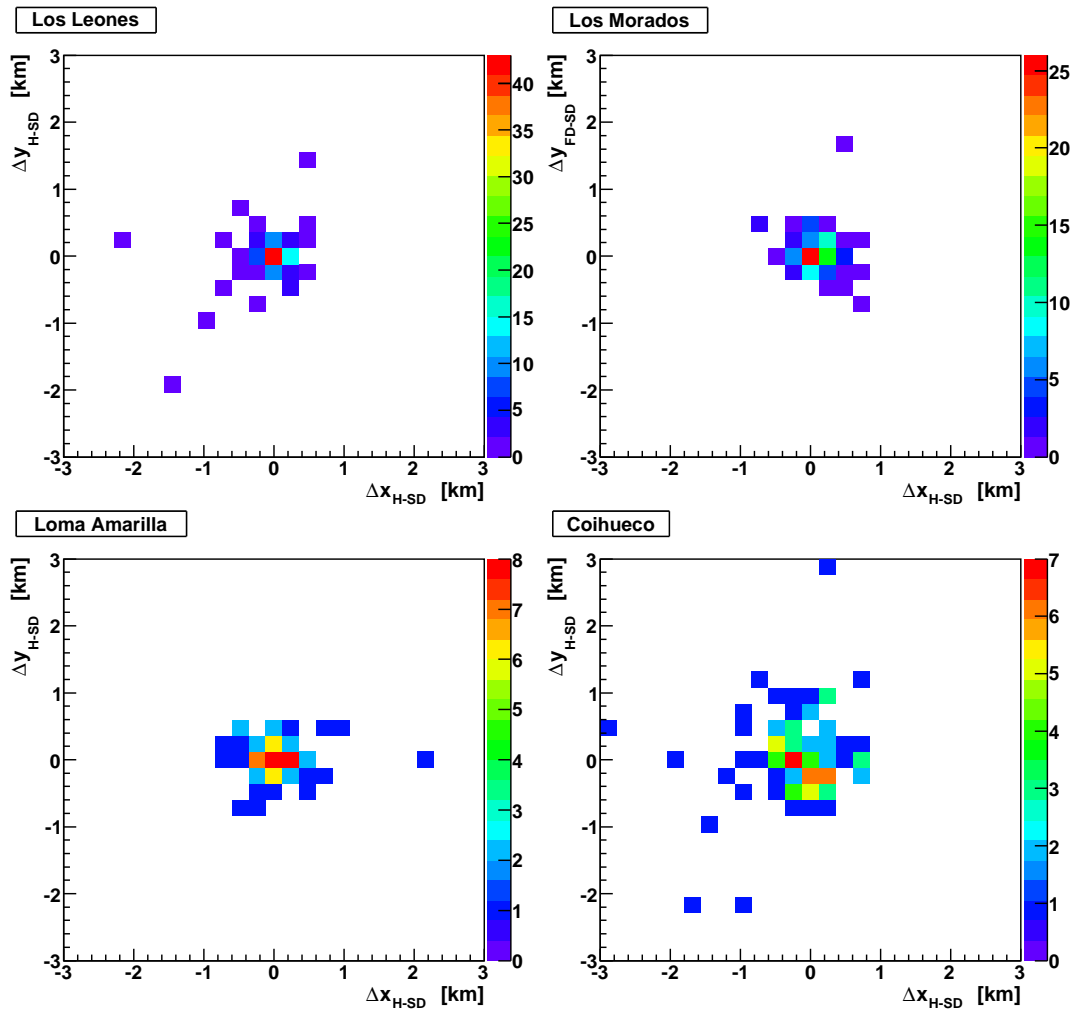
**Figure 7.17:** Distance between Hybrid- and SD-reconstructed shower core in $x$- and $y$-direction, for each individual eye.
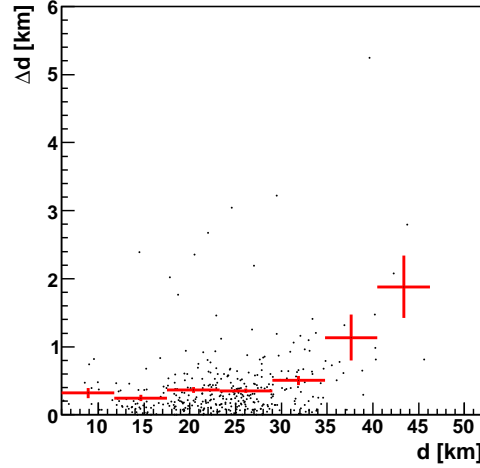
**Figure 7.18:** Distance between Hybrid- and SD-reconstructed shower core, $\Delta d$, as a function of the Hybrid-reconstructed core-eye-distance $d$. The distribution is superimposed with its profile. Error bars: RMS/$\sqrt{N}$.

## 7.4.1 Summary and outlook

The accuracy of the shower core reconstruction is not covered by the angular resolution studies. The present analysis is a complementary analysis to investigate the reconstruction accuracy of Hybrid-reconstructed shower axes.

The results of Los Leones, Los Morados and Loma Amarilla are rather expected. Los Leones and Los Morados provide a comparatively precise Hybrid geometry reconstruction, resulting in an accurate reconstruction of the direction and the core of the shower axis. The geometry reconstruction of Loma Amarilla has not been optimized yet, as mentioned before, which might cause a comparatively inaccurate Hybrid reconstruction of both the core and the direction of the shower axis. As the Hybrid angular resolution of Coihueco does not exceed the average resolution of the entire detector significantly, the resulting accuracy of the shower core for Coihueco is remarkable. The unit cell of the SD array is an equal-sided triangle of 1.5 km spacing between each two SD tanks. Thus a distance[9] of 1.73 km or more between both cores means that there must be a tank that is closer to the Hybrid core than the SD-reconstructed hottest tank. Six of 99 events of Coihueco have a core distance exceeding 1.73 km. Despite selecting only high quality events regarding the geometry reconstruction, those events pass the cuts.

The mean distance between SD- and Hybrid-reconstructed shower core increases as a function of core-eye-distance. This dependence may be related to a decreasing accuracy of FD measurements for large observation distances due to atmospheric scattering. For increasing observation distances the observed light intensity in the camera faints and the arriving fluorescence light spreads around the true direction. Thus the sharpness of the

---

[9]An equal-sided hexagon of approximately 0.87 km side length around the hottest tank comprises all shower cores whose closest tank is the hottest tank. The largest distance within this hexagon is 1.73 km.

camera trace and the timing of the pixels depend on this distance, which in conclusion influences the geometry reconstruction accuracy.

The present analysis could be performed investigating much more details. As the Hybrid reconstruction accuracy is mainly given by three parameters ($\chi^2/N_{\mathrm{dof}}$ of the time fit, the event-wise time offset between SD and FD and the distance between hottest tank and shower axis), an analysis of possible correlations between those parameters and $\Delta d$ could be performed. Another question is related to the relative location of SD and Hybrid core. An analysis of the angle between the connecting lines $\vec{D}_{\mathrm{H}}$ between Hybrid core and eye and $\vec{D}_{\mathrm{SD}}$ between SD core and eye, taking $\vec{D}_{\mathrm{SD}}$ as zero, could reveal eventual offsets of individual eyes.

# Chapter 8

# Variation of the SD Energy Calibration with Time

The analysis of the variation of the SD energy calibration with time is an important issue concerning the understanding of the detector, which is preceding measurements related to the spectrum of CR. The flux of CR as a function of energy depends strongly on the energy scale and its accuracy. In the Hybrid detection mode the energy measurement is performed by FD and SD simultaneously. The SD energy $E_{SD}$ is calibrated with the FD energy $E_{FD}$ independent of simulations, as explained in Section 5.4. Once calibrated the SD energy scale, an energy measurement using SD only is provided.

In this chapter two different analyses are presented to investigate the temporal variation of the energy calibration. Applying a fixed energy calibration to the whole dataset, the analysis of the variation of the energy ratio $E_{SD}/E_{FD}$ and of differential flux of CR with time can shed light on eventual changes of the measured SD and FD energies.

The calibration parameters of two different calibration functions, here noted as *PRL08* and *ICRC09*, are given in Table 5.1. The *PRL08* calibration [61] is the default calibration that is used up to now and that has been used for the reconstruction. It has been performed on a dataset[1] of 661 Golden Hybrid events from January 1st, 2004 until August 31st, 2007. The *ICRC09* calibration [59] has been performed using 795 Golden Hybrid events from January 1st, 2004 until December 31st, 2008. As the reconstruction has been done using the *PRL08* calibration, the SD energy based on the *ICRC09* calibration can be obtained from applying the related calibration function on the SD energy estimator[2] $S^{38}$.

## 8.1 Cuts and dataset

Reconstructed Golden Hybrid data from January 1st, 2004 until March 31st, 2009, downloaded from the Auger Observer webpage[3], have been used for the present analyses. The

---

[1]This dataset has been selected using another set of cuts than used for the present analysis. For details about the cuts see [61].

[2]$S^{38}$ can be derived from $S_{1000}$ as explained in Section 5.1.2.

[3]*http://augerobserver.fzk.de*

reconstruction has been performed with $\overline{\text{Off}}\underline{\text{line}}$ version `v2r5p6`.
The data have been selected using the cuts of the *ICRC09* energy calibration (see [59]), selecting a subset of high quality Golden Hybrid events:

- Data of Los Leones not before December 1st, 2004

- Data of Los Morados not before June 2nd, 2005

- Data of Loma Amarilla rejected completely due to a preliminary PMT calibration

- Data of Coihueco not before December 1st, 2004

- Zenith angle $\theta < 60°$ (selecting only non-inclined showers)

- Offline T4 trigger value $> 1$

- The 6T5 trigger[4] used in [59] has been relieved by using a 5T5 trigger[5]

- Distance between hottest tank and shower axis $< 750$ m

- Gaisser-Hillas fit: $\chi^2_{\text{GH}}/N_{\text{dof,GH}} \leq 2.5$

- Comparison of Gaisser-Hillas fit and straight line fit: $\chi^2_{\text{Lin}} - \chi^2_{\text{GH}} \geq 4$

- $\Delta X_{\text{max}} \leq 40$ g/cm$^2$

- $X_{\text{max}}$ within the field-of-view of the telescope

- Summed up tracklength of holes in the longitudinal shower profile $< 20\%$ of the profile

- Cherenkov fraction $\leq 50\%$

- Mie-database entry must be available for each event

- FD Energy reconstruction uncertainty $\Delta E_{\text{FD}}/E_{\text{FD}} < 20\%$

- $\Delta S^{38}/S^{38} < 50\%$

- Ellipse cut (see Section 8.1.1)

In addition to the high quality cuts a set of consistency cuts has been applied:

- $E_{\text{FD}} > 0$ and $S^{38} > 0$

- $0 < \Delta E_{\text{FD}} < 10^{22}$ eV and $0 < \Delta S^{38} < 1000$ VEM

---

[4]The 6T5 trigger is realized by requiring an Offline T5 trigger value of 1 or 3.
[5]The 5T5 trigger is realized by requiring an Offline T5 trigger value of 2 or 3.

Those cuts assure an accurate reconstruction of the LDF and especially the SD energy estimator $S_{1000}$, an accurate Hybrid reconstruction of the geometry and an accurate reconstruction of the longitudinal shower profile of the selected dataset. The 6T5 trigger has been relieved by using a 5T5 trigger, as this trigger is used for analyses of the correlations of the shower direction with UHECR source candidates. The 5T5 trigger should be used for events with 10 triggered tanks or more (for details see [44]). The dataset selected by the complete set of cuts yields an average tank multiplicity of seven tanks and approximately 15% events which fulfill the condition. Therefore, the analyses are redone using the 6T5 cut in order to control the influence of the 5T5 cut.

Applying the complete set of cuts, 1472 events are selected in case of the 5T5 cut and 1264 events are selected in case of the 6T5 cut, interpreting the data of each triggered eye as a single event. This causes a slight bias, as in [59] a weighted mean of all triggered eyes has been built to be treated as one event. The original[6] dataset of the *ICRC09* calibration contains 795 events, yielding 860 datapoints in case of treating the data of every eye separately.

### 8.1.1  Ellipse cut

The ellipse cut has been introduced to minimize the bias caused by cutting on the lower edge of the energy calibration spectrum (see Fig. 5.9). Using Golden Hybrid data, the relative FD energy uncertainty, also called energy resolution in this thesis, is constant[7] as a function of energy and the relative uncertainty of $S^{38}$ decreases with energy (cf. [60]). Thus the $1\sigma$ contour of each data point of the calibration spectrum is an ellipse, assuming $E_{\mathrm{FD}}$ and $S^{38}$ to be Gaussian-distributed. Any rejection of data points below a line that intersects the ellipse centered in $(E_{\mathrm{FD}}^{\mathrm{cut}}, S_{\mathrm{cut}}^{38})$ will cause a bias. The ellipse cut selects events within the 90% confidence level ellipse centering in $(E_{\mathrm{FD}}^{\mathrm{cut}}, S_{\mathrm{cut}}^{38})$.

For the present calibration studies $S_{\mathrm{cut}}^{38} = 25$ has been chosen. The FD energy cut $E_{\mathrm{FD}}^{\mathrm{cut}}$ is calculated within the $\chi^2$ minimization of the fit on the calibration spectrum.

## 8.2  Variation of the ratio of SD and FD energy with time

The analysis of the energy ratio $E_{\mathrm{SD}}/E_{\mathrm{FD}}$ for a fixed energy calibration as a function of time can shed light on eventual changes of the measured SD and FD energies. The time periods have been chosen according to the correlation analyses presented in [58]:

---

[6]The original dataset has been selected based on Golden Hybrid data from January 1st, 2004 until December 31st, 2008 that have been reconstructed with Offline version `v2r5p1`. The complete set of cuts has been used, including the 6T5 cut.

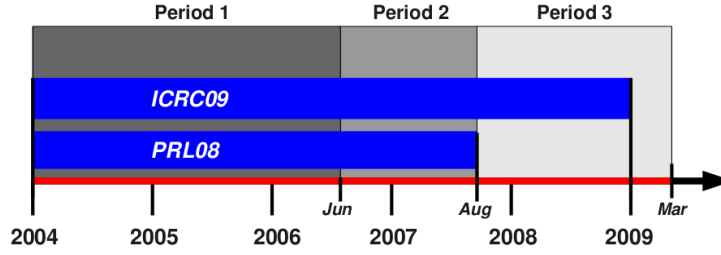[7]This condition is fulfilled, cf. Section 9.2.

**Figure 8.1:** The blue bars represent the underlying time periods of the Golden Hybrid datasets that have been used for the *PRL08* and *ICRC09* energy calibration. The grey regions indicate the three time periods that have been used for the present analyses.

**Period 1:** January 1st, 2004 - May 26th, 2006
**Period 2:** May 27th, 2006 - August 31st, 2007
**Period 3:** September 1st, 2007 - March 31st, 2009

An overview over all relevant time periods of this analysis is given in Fig. 8.1. At first the energy ratio $E_{\mathrm{SD}}/E_{\mathrm{FD}}$, based on the *ICRC09* calibration, has been analysed as a function of $E_{\mathrm{FD}}$ for the particular periods (Fig. 8.2 - 8.4) and for the full period (Fig. 8.5). The profiles of the particular distributions have been fitted with a constant line, as this is a basic requirement for the SD energy calibration. Details about the evaluation of fits, in particular with small $N_{\mathrm{dof}}$, are given in Chapter 6. The fit results are given in each plot, yielding an agreement with an energy-independent ratio $E_{\mathrm{SD}}/E_{\mathrm{FD}}$ for all periods. This means that a comparison of the fit constants as the only free fit parameters yields direct information about the variation of the FD and SD energy scale with time. In case of a successful energy calibration the fit constant $\langle E_{\mathrm{SD}}/E_{\mathrm{FD}}\rangle$, representing the average energy ratio, is expected to be in agreement with one through all periods. The resulting fit constants are summarized in Table 8.1.
The average energy ratio of the first and second period are in agreement with a ratio of one within two and three standard deviations respectively. The fit of the third period yields a ratio of $1.104 \pm 0.007$, which deviates from one by about 15 standard deviations. This result indicates either a shift of the FD energy to lower energies, a shift of the SD energy to higher energies or a shift of both within period 3. Moreover, the range of the profile has been scaled down, as only four events are found above $10^{19.4}$ eV. In period 1 as well four events have energies of $10^{19.4}$ eV or more, but within less than one third of the statistics of period 3. This might again indicate an underestimation of $E_{FD}$. The plot of the full period shows a structure that could eventually be a sign of saturation effects of the SD.
The same analysis has been performed using the 6T5 cut instead of the 5T5 cut, as the 5T5 cut is not recommended for the lower energy range. The results are listed in Table 8.1 and the related plots are given in Fig. B.1 - B.4 in the appendix. The results using the 6T5 cut confirm the former findings within the statistical uncertainties.
In order to check if this variation with time can be found even within the original *ICRC09*

| **ICRC09**, 5T5 cut | $\langle E_{\mathrm{SD}}/E_{\mathrm{FD}} \rangle$ | # |
|---|---|---|
| Period 1 | $1.021 \pm 0.012$ | 206 |
| Period 2 | $1.021 \pm 0.007$ | 574 |
| Period 3 | $1.104 \pm 0.007$ | 692 |
| Full Period | $1.061 \pm 0.005$ | 1472 |
| **ICRC09**, 6T5 cut | $\langle E_{\mathrm{SD}}/E_{\mathrm{FD}} \rangle$ | # |
| Period 1 | $1.035 \pm 0.013$ | 163 |
| Period 2 | $1.025 \pm 0.008$ | 496 |
| Period 3 | $1.105 \pm 0.008$ | 603 |
| Full Period | $1.065 \pm 0.006$ | 1264 |
| **ICRC09**, original | $\langle E_{\mathrm{SD}}/E_{\mathrm{FD}} \rangle$ | # |
| Period 1 | $1.061 \pm 0.015$ | 148 |
| Period 2 | $0.996 \pm 0.008$ | 465 |
| Period 3 | $1.056 \pm 0.011$ | 274 |
| Full Period | $1.022 \pm 0.006$ | 860 |
| **PRL08**, 5T5 cut | $\langle E_{\mathrm{SD}}/E_{\mathrm{FD}} \rangle$ | # |
| Period 1 | $1.045 \pm 0.013$ | 206 |
| Period 2 | $1.046 \pm 0.008$ | 574 |
| Period 3 | $1.130 \pm 0.010$ | 692 |
| Full Period | $1.086 \pm 0.005$ | 1472 |

**Table 8.1:** The average energy ratio $\langle E_{\mathrm{SD}}/E_{\mathrm{FD}} \rangle$ resulting from constant line fits on the profile of the energy ratio distributions for different time periods. The analysis has been performed using the *ICRC09* and the *PRL08* energy calibration. The 5T5 cut has been used according to correlation analyses, requiring a cross-check using the 6T5 cut. Moreover, the analysis has been performed based on the original dataset used for the *ICRC09* calibration. The error of the ratio represents the error of the related fit parameter.

| Entries | 206 |
| Mean | 18.86 |
| Mean y | 1.021 |
| RMS | 0.259 |
| RMS y | 0.1895 |
| $\chi^2$ / ndf | 1.515 / 5 |
| Prob | 0.9113 |
| p0 | $1.021 \pm 0.012$ |
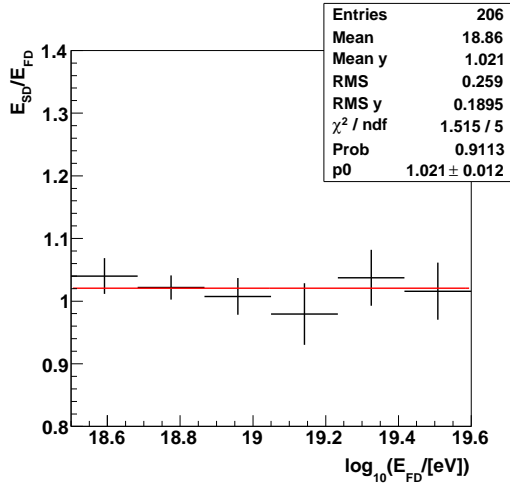
**Figure 8.2:** Mean energy ratio $E_{\mathrm{SD}}/E_{\mathrm{FD}}$ as a function of $E_{\mathrm{FD}}$, for period 1. The profile has been fitted with a constant (red line). Error bars: RMS/$\sqrt{N}$.

| Entries | 574 |
| Mean | 18.8 |
| Mean y | 1.028 |
| RMS | 0.2374 |
| RMS y | 0.1889 |
| $\chi^2$ / ndf | 10.3 / 7 |
| Prob | 0.1724 |
| p0 | $1.021 \pm 0.007$ |
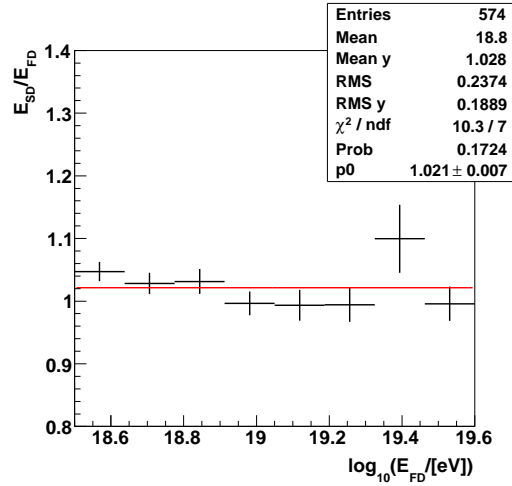
**Figure 8.3:** Mean energy ratio $E_{\mathrm{SD}}/E_{\mathrm{FD}}$ as a function of $E_{\mathrm{FD}}$, for period 2. The profile has been fitted with a constant (red line). Error bars: RMS/$\sqrt{N}$.

| Entries | 692 |
| Mean | 18.78 |
| Mean y | 1.104 |
| RMS | 0.2184 |
| RMS y | 0.1952 |
| $\chi^2$ / ndf | 7.916 / 7 |
| Prob | 0.34 |
| p0 | $1.104 \pm 0.007$ |
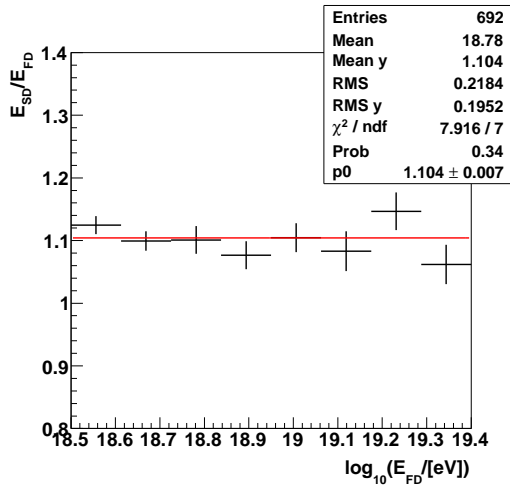
**Figure 8.4:** Mean energy ratio $E_{\mathrm{SD}}/E_{\mathrm{FD}}$ as a function of $E_{\mathrm{FD}}$, for period 3. The profile has been fitted with a constant (red line). Error bars: RMS/$\sqrt{N}$.

| Entries | 1472 |
| Mean | 18.8 |
| Mean y | 1.063 |
| RMS | 0.2405 |
| RMS y | 0.1979 |
| $\chi^2$ / ndf | 15.3 / 9 |
| Prob | 0.08293 |
| p0 | $1.061 \pm 0.005$ |
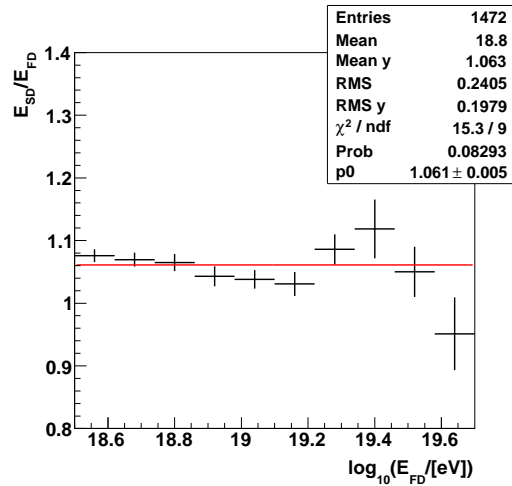
**Figure 8.5:** Mean energy ratio $E_{\mathrm{SD}}/E_{\mathrm{FD}}$ as a function of $E_{\mathrm{FD}}$, for the full period. The profile has been fitted with a constant (red line). Error bars: RMS/$\sqrt{N}$.

dataset only, the analysis has been redone using the 795 events[8] that have been used for this energy calibration (see Fig. B.9 - B.12 in the appendix, results in Table 8.1). The different numbers of events for the first and second period, compared to the former result, are a consequence of using an older offline version that has been used for the reconstruction of the calibration dataset (Offline version `v2r5p1`). The first period yields an average energy ratio of $1.061 \pm 0.015$, deviating from one within approximately four standard deviations. The second period is in agreement with a ratio of one. The third period yields a ratio of $1.056 \pm 0.011$, deviating from one within approximately five standard deviations. The resulting ratio of period 3 might support the former indications for a shift of at least one energy, even within this original calibration dataset.

Moreover, the distribution in Fig. B.12, subtracted by one to obtain the quantity $(E_{\mathrm{SD}} - E_{\mathrm{FD}})/E_{\mathrm{FD}}$, can be compared to the corresponding distribution given in [59]. The mean $\mu$ and the RMS of both distributions are in agreement within the statistical uncertainties, yielding $\mu \approx 0.02$ and RMS $\approx 0.01$. Slight differences may be caused by the statistical dependence caused by splitting up multi-eye events into events of the particular eyes.

As the *PRL08* energy calibration is commonly used for reconstructions up to now, the analysis has been redone using this energy calibration (see Fig. B.5 - B.8 in the appendix, results in Table 8.1). The average energy ratios of the second and the third period are comparatively higher than for the *ICRC09* calibration, supporting again the former findings. Moreover, this result might as well indicate an energy shift even within the calibration dataset.

The results indicate either a shift of the SD energy to higher energies, a shift of the FD energy to lower energies or a shift of both, as a function of time. It seems that none of the energy calibrations is able to establish a stable energy ratio. Particular conclusions on the FD and SD energy cannot be drawn from this analysis method.

## 8.3   Variation of the differential flux of CR with time

In order to analyse the temporal variation of the SD and FD energy separately, a second approach has been used. The differential flux for a certain energy and within a period of a certain exposure is expected to be equal for all periods of similar exposures. Therefore, the time span from May 28th, 2006 until March 31st, 2009 has been subdivided into four periods of rather equal 5T5 exposures:

---

[8]Yielding 860 datapoints, as the data of every eye are treated separately.

Overall exposure = 12643 (10768) km$^2$ sr yr

**Period 1:** May 28st, 2006 - May 14th, 2007
exposure = 3161 (2651) km$^2$ sr yr
**Period 2:** May 15th, 2007 - January 22th, 2008
exposure = 3154 (2703) km$^2$ sr yr
**Period 3:** January 23th, 2008 - September 4th, 2008
exposure = 3167 (2647) km$^2$ sr yr
**Period 4:** September 1st, 2008 - March 31st, 2009
exposure = 3160 (2766) km$^2$ sr yr

The related 6T5 exposures are given in braces. The deviations of the particular exposures for each period from the average exposure is below 0.3% for the 5T5 trigger and below 2.8% for the 6T5 trigger. The influence of those deviations on the results and an error of about 1% resulting from a calculation of the exposures from dates instead of hours, minutes and seconds will be neglected.

Within these time periods the differential flux can be analysed as a function of $E_{\mathrm{FD}}$ and $E_{\mathrm{SD}}$. Due to low statistics in the higher energy range, periods 1+2 and periods 3+4 have been merged. The result of Section 8.2 for the dataset reconstructed with $\overline{\mathrm{Off}}\underline{\mathrm{line}}$ version `v2r5p6` and selected with the full set of cuts (incl. 5T5 cut), is a shift of the energy ratio by about 10%. Assuming the flux to follow a power law spectrum $E^{-3.2}$, an underestimation of $E_{\mathrm{FD}}$ by i.e. 10% would result in a decrease[9] of the flux by about 26%.

Figure 8.6 shows a comparison of the differential fluxes of periods 1+2 and periods 3+4 as a function of $E_{\mathrm{SD}}$. The comparison points out a significant decrease of the differential flux within the lower energy range up to 20 EeV. Within the energy range from 20 EeV to 40 EeV the shift of the flux is less significant due to low statistics. But the magnitude of the eventual shift is still in agreement with the order of the roughly estimated, expected magnitude of this shift of about 26%. Figure 8.7 shows a similar plot comparing the differential fluxes of periods 1+2 and periods 3+4 now as a function of $E_{\mathrm{FD}}$. The result is similar, but within energy range from 20 EeV to 40 EeV the error bars do not intersect. After comparing the fluxes of different periods as a function of $E_{\mathrm{SD}}$ or $E_{\mathrm{FD}}$, another set of plots has been done to compare the fluxes of one period as a function of $E_{\mathrm{SD}}$ and $E_{\mathrm{FD}}$. Figures 8.8 and 8.9 show a comparison of the differential fluxes as a function of $E_{\mathrm{SD}}$ and $E_{\mathrm{FD}}$ for periods 1+2 and periods 3+4 respectively. The magnitude of a possible shift between the flux related to $E_{\mathrm{FD}}$ compared to the flux related to $E_{\mathrm{SD}}$ is in agreement with an expected maximum shift of about 26% in case of an energy ratio $E_{\mathrm{SD}}/E_{\mathrm{FD}} \approx 1.1$. Comparing the results of both periods, the second period maybe indicates a slightly larger shift between the fluxes, but this conclusion is not significant with regard to the uncertainties.

As the 5T5 cut might influence the reconstruction accuracy of the lower energy range and thus the accuracy of the related results, the analyses have been redone using the

---

[9]Remark: $(1.1 \cdot E_{\mathrm{FD}})^{-3.2} \approx 74\% \cdot E_{\mathrm{FD}}$

6T5 cut. The results are in agreement with the former presented results. Moreover, the 5T5 analysis has been cross-checked using another common reconstruction software called *Herald*. The results are in good agreement as well.

The presented findings might indicate a shift of the differential flux related to $E_{\rm FD}$ and $E_{\rm SD}$ to lower fluxes as a function of time. The comparison of both fluxes within each period yields only vague results that might indicate a dominant shift of the flux related to $E_{\rm FD}$. The present results are in agreement with the results of Section 8.2. An underestimation of $E_{\rm FD}$ could be explained by aging PMT that measure a lower signal than the expected (see Fig. 8.10). This underestimation of $E_{\rm FD}$ would be propagated to $E_{\rm FD}$ by the energy calibration. Thus the decrease of the flux as a function of $E_{\rm SD}$ could be completely inherited from $E_{\rm FD}$ or it could be partly caused by an aging of the PMT. Actually regular calibrations[10] of SD and FD should compensate changes of the energy scales caused by aging PMT.

## 8.4 Summary and outlook

In this chapter two complementary approaches have been presented to analyse the variation of the energy calibration with time. The analysis of the variation of $E_{\rm SD}/E_{\rm FD}$ with time, using the *ICRC09* calibration, yields a ratio of $1.104 \pm 0.007$ for the third period[11], deviating from one by 10.4% within about 15 standard deviations. A similar result has been obtained using the *PRL08* energy calibration. This significant deviation of the energy ratio by about 10.4% might indicate an underestimation of $E_{\rm FD}$, an overestimation of $E_{\rm SD}$ or a shift of both. It seems that none of the calibration functions is able to establish a stable energy ratio over a longer time period. Further details cannot be drawn from this analysis, as an analysis of a ratio is not sensitive to its particular components.

The analysis of the differential flux as a function of $E_{\rm FD}$ and $E_{\rm SD}$ within different time periods might indicate a decrease of the flux. An eventual larger shift related to $E_{\rm FD}$ might be vaguely concluded from the results. The magnitude of the shifts of the energy ratio and the differential flux are in agreement.

An underestimation of $E_{FD}$ could be explained by aging PMT. This underestimation would be propagated to $E_{SD}$ by the energy calibration. Based on these two analyses it is not clear if an eventual underestimation of $E_{SD}$ is completely inherited from $E_{FD}$ or if its partly caused by aging PMT or anything else. A similar analysis of the differential flux as a function of the SD energy estimator $S^{38}$ could help to answer this question.

The analysis of the differential flux could be done again for suffcent statistics in the energy range around 57 EeV and above, as this energy range is used for analyses of correlations between the reconstructed shower directions and UHECR source candidates. Moreover, higher statistics would provide more reliable results.

---

[10]For details about the detectors see Sections 4.1 and 4.1.
[11]September 1st, 2007 - March 31st, 2009
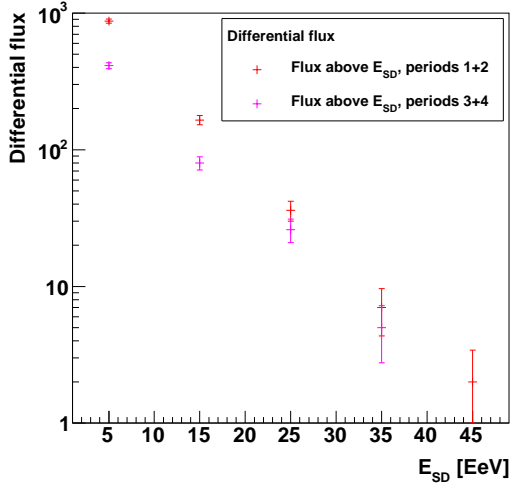
**Figure 8.6:** Differential flux as a function of $E_{\mathrm{SD}}$ for periods 1+2 (red) and for periods 3+4 (purple). The markers are located in the center of the underlying energy interval. Error bars: RMS/$\sqrt{N}$.
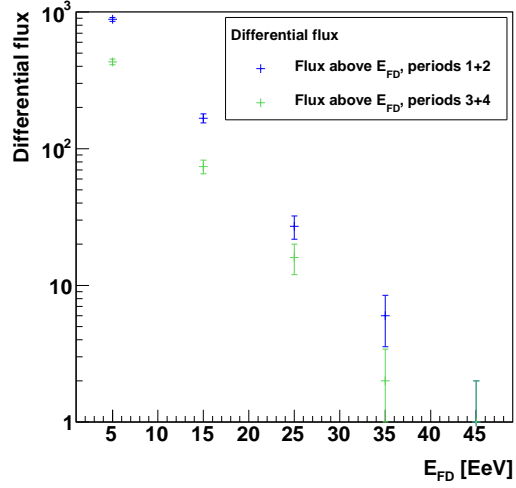


**Figure 8.7:** Differential flux as a function of $E_{\mathrm{FD}}$ for periods 1+2 (blue) and for periods 3+4 (green). The markers are located in the center of the underlying energy interval. Error bars: RMS/$\sqrt{N}$.
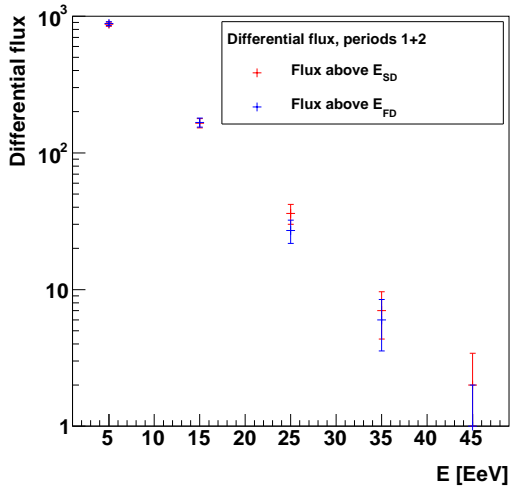


**Figure 8.8:** Differential flux of periods 1+2 as a function of $E_{\mathrm{FD}}$ (blue) and $E_{\mathrm{SD}}$ (red). The markers are located in the center of the underlying energy interval. Error bars: RMS/$\sqrt{N}$.
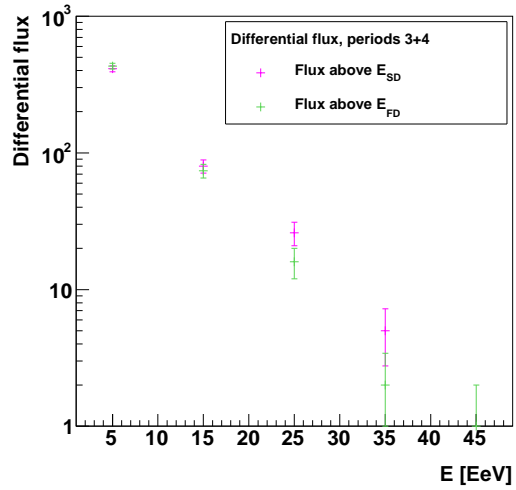


**Figure 8.9:** Differential flux of periods 3+4 as a function of $E_{\mathrm{FD}}$ (green) and $E_{\mathrm{SD}}$ (purple). The markers are located in the center of the underlying energy interval. Error bars: RMS/$\sqrt{N}$.
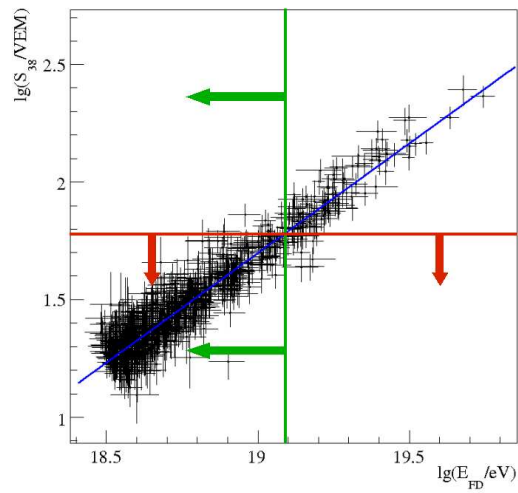
**Figure 8.10:** An example for a true FD energy and SD energy estimator is represented by the green and red line respectively. The arrows indicate a shift of the measured values to lower FD and SD energies. These shifts could be of different size.

# Chapter 9

# Energy Resolution Studies

The accuracy of the energy reconstruction is an important issue concerning the understanding of the detector, which is preceding measurements related to the spectrum of CR. The measured flux of CR as a function of energy strongly depends on the energy scale and its accuracy.

In the Hybrid mode the energy measurement is performed using combined SD and FD information. The SD energy $E_{\mathrm{SD}}$ is calibrated with the FD energy $E_{\mathrm{FD}}$, as explained in Section 5.4. Therefore, the FD energy resolution has a large impact on the accuracy of the SD energy scale as a consequence of the energy calibration. Thus the resolution of $E_{\mathrm{FD}}$ and $E_{\mathrm{SD}}$ influence the accuracy of CR flux measurements. In addition to the energy calibration studies presented in Chapter 8, here, the energy resolution within statistical and systematic reconstruction uncertainties has been estimated by comparing $E_{\mathrm{FD}}$ and $E_{\mathrm{SD}}$ of the same event.

The present analysis can be subdivided into three sections: An analysis of the distance- and energy-dependence of the FD and SD energy resolution, an approximation in order to obtain an average energy resolution of both detector systems and an evaluation of the estimation of the energy reconstruction uncertainties.

The energy resolution is estimated by the relative reconstruction uncertainty $\Delta E/E$.

## 9.1   Cuts and dataset

Reconstructed Golden Hybrid data from January 1st, 2004 until March 31st, 2009, downloaded from the Auger Observer webpage[1], have been used for these studies. The reconstruction has been performed with $\overline{\mathrm{Off}}\underline{\mathrm{line}}$ version `v2r5p6`, using the *PRL08* energy calibration[2] for the SD energy.

The dataset has been selected using the cuts introduced in Section 8.1, except of the ellipse cut (see Section 8.1.1). The ellipse cut has been replaced by requiring $E_{\mathrm{FD}} > 3 \cdot 10^{18}$ eV, as above this energy the efficiency of Hybrid measurements is larger than 99% (cf. [61]).

---

[1] *http://augerobserver.fzk.de*
[2] The calibration functions have been introduced in Section 5.4.
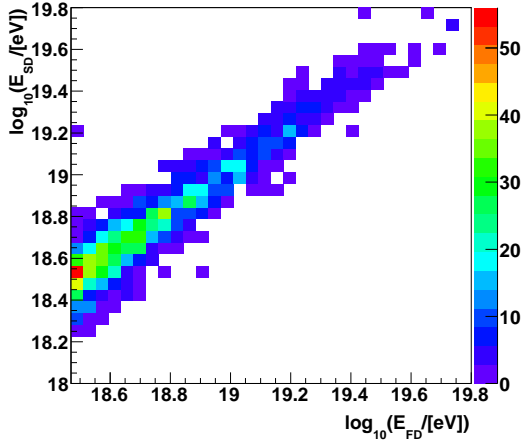
**Figure 9.1:** Two-dimensional distribution of FD energy $E_{FD}$ and SD energy $E_{SD}$. The color gradient represents the number of events per bin.
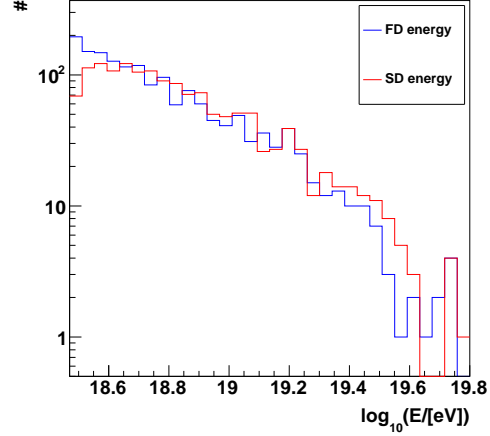


**Figure 9.2:** Superimposed FD and SD energy. The counting rates differ for energies below approximately 18.6 eV, due to a cut-related shift of $E_{SD}$ to lower energies within this energy range.

The 6T5 trigger has again been relieved by using the 5T5 trigger in order to keep the dataset similar to the dataset of Chapter 8. This trigger might cause a worse reconstruction quality for events with less than 10 triggered tanks, according to [44]. As the average tank multiplicity is seven tanks and about 10% of the events have a tank multiplicity of 10 tanks or more, the choice of the 5T5 cut might influence the results. The analyses regarding the entire detector have been done a second time using the 6T5 trigger instead of 5T5, yielding variations of the magnitude of the uncertainties. The exact shape of the profiles analysed in the following does not change much as well.

Interpreting every eye as a single event, 1605 events are selected by applying the cuts. The cut on the FD energy $E_{FD}$ causes a bias when looking at the lower energies of the distribution given in Fig.9.1. The cut rejects all events located left of the related line that is parallel to the $y$-axis. Below $E_{SD} \approx 10^{18.6}$ eV this bias causes a shift of the mean $E_{SD}$ to lower energies (cf. Fig. 9.2). This effect must be considered in fits of distributions that contain $E_{SD}$ by adjusting the fit range.

$E_{SD}$ is calibrated applying Eq. 5.12, which means that $E_{SD}$ and $E_{FD}$ should be distributed symmetrically around the line of equal energies, comprising it with the statistical error bars. As mentioned before, each dataset of non-fixed parameters (i.e. energy, distance, angular tracklength and tank multiplicity) incorporates multidimensional correlations of various dependences.

The average FD energy, $\langle E_{FD} \rangle$, increases as a function of core-eye-distance and the closest distance $R_p$ between eye and shower axis. A dependence of the average SD energy, $\langle E_{SD} \rangle$,

on the distance is inherited from FD by using only Hybrid events. Figure 9.3 shows the distribution of $\langle E_{\mathrm{FD}} \rangle$ on the detector array. Since Loma Amarilla has been excluded completely from this analysis due to a preliminary PMT calibration, less events with low and moderate energies are observed near Loma Amarilla, resulting in a comparatively high mean energy near Loma Amarilla. In Fig. 9.4 $\langle E_{\mathrm{FD}} \rangle$ is plotted as a function of $R_{\mathrm{p}}$, showing a similar energy-distance-dependence. Related plots of the individual[3] eyes can be found in Fig. B.13 in the appendix.

Due to the different measurement techniques, the energy reconstruction uncertainties $\Delta E_{\mathrm{FD}}$ and $\Delta E_{\mathrm{SD}}$ differ as well. As mentioned before, FD energy measurements have to be corrected for atmospheric scattering. The accuracy of those corrections results in an increase of $\langle \Delta E_{\mathrm{FD}} \rangle$ as a function of distance, for a fixed energy. This effect is superimposed with a expected decrease of $\langle \Delta E_{\mathrm{FD}} \rangle$ as a function of energy due to a related increasing light intensity, for a fixed distance. Moreover, the energy-dependent light intensity and a short observed angular tracklength limit the maximum distance of FD measurements. Just about 0.1% of the selected events have an $R_{\mathrm{p}} > 30$ km.

Another effect has been mentioned before in Chapter 7.1. The angular tracklength observed within the field-of-view of the FD decreases for showers close to the telescope and thus the Hybrid reconstruction accuracy degrades for those showers.

As SD measurements are less influenced by the atmosphere, $\langle \Delta E_{\mathrm{SD}} \rangle$ is expected to decrease as a function of energy and thus as a function of core-eye-distance and $R_{\mathrm{p}}$ as well, as a consequence of the restriction to Hybrid events. For small core-eye-distances $\langle \Delta E_{\mathrm{SD}} \rangle$ is expected to increase as the shower core is close to the borders of the array. The accuracy of the LDF reconstruction degenerates for lateral shower distributions where the shower core is close to the array border and thus a larger part of the shower is not measured.

## 9.2 FD and SD energy resolution as a function of distance and energy

The particular energy resolutions of FD and SD, estimated by $\Delta E_{\mathrm{FD}}/E_{\mathrm{FD}}$ and $\Delta E_{\mathrm{SD}}/E_{\mathrm{SD}}$, have been analysed as a function of $E_{\mathrm{FD}}$ and $R_{\mathrm{p}}$. One of the applied cuts requires $\Delta E_{\mathrm{FD}}/E_{\mathrm{FD}} < 20\%$. This requirement does not directly cut on $\Delta E_{\mathrm{FD}}$ but mainly on the fit quality of the Gaisser-Hillas fit of the longitudinal profile.

Figure 9.5 shows $\Delta E_{\mathrm{FD}}/E_{\mathrm{FD}}$ as a function of $E_{\mathrm{FD}}$. The average FD energy resolution $\langle \Delta E_{\mathrm{FD}}/E_{\mathrm{FD}} \rangle$ as a function of $E_{\mathrm{FD}}$ has been fitted with a constant, yielding an average energy resolution of approximately 8.9%. A fit probability of 0.062 means that with a probability of 6.2% even larger $\chi^2$ would be measured for a given $N_{\mathrm{dof}}$ as a consequence of statistical uncertainties, assuming a Gaussian distribution. As $N_{\mathrm{dof}}$ is less than $\sim 35$ (for details see Chapter 6), the $\chi^2$-distribution is not symmetric. Thus it is different to interpret this probability in terms of a confidence interval. We do not reject the hypoth-

---

[3]Loma Amarilla has only been included for the analysis of this individual eye.
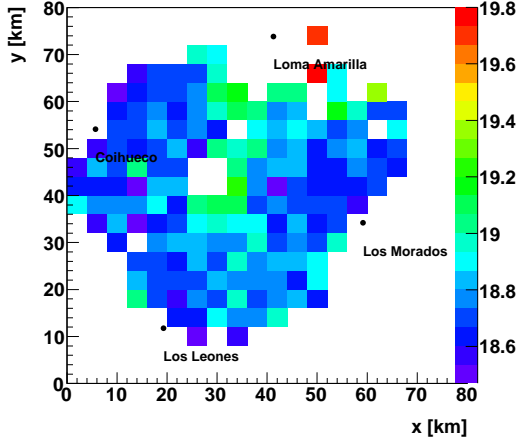
**Figure 9.3:** Distribution of the FD energy on the detector array. The color gradient represents the logarithm of the average FD energy, $\log_{10}\left(\langle E_{\mathrm{FD}}\rangle/[\mathrm{eV}]\right)$.
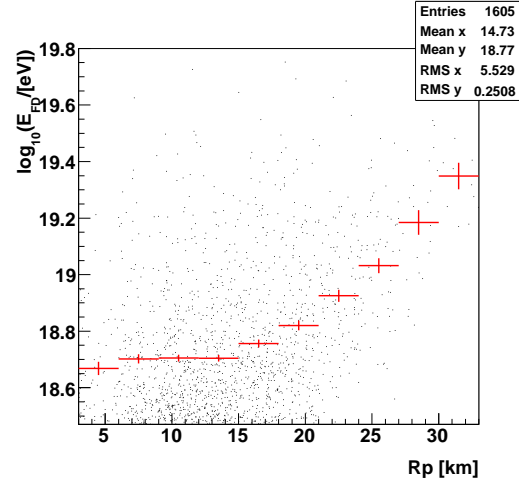


**Figure 9.4:** Distribution of the logarithmic FD energy, $\log_{10}(E_{\mathrm{FD}}/[\mathrm{eV}])$, as a function of the closest distance $R_{\mathrm{p}}$ between eye and shower axis. The distribution is superimposed with its profile. Error bars: RMS/$\sqrt{N}$.

esis of a constant $\Delta E_{\mathrm{FD}}/E_{\mathrm{FD}}$ as a function of $E_{\mathrm{FD}}$ for a minimum probability of 6.2%. Figure 9.6 shows $\Delta E_{\mathrm{FD}}/E_{\mathrm{FD}}$ as a function of $R_{\mathrm{p}}$. The energy resolution increases approximately linearly with $R_{\mathrm{p}}$ above a distance of about 5 km. An assumption of a linear increase of $\Delta E_{\mathrm{FD}}/E_{\mathrm{FD}}$ over the full range of $R_{\mathrm{p}}$ seems not to be supported by the fit results[4] of a straight line fit. A straight line fit of the range above $R_{\mathrm{p}} = 5$ km yields a probability of 30.7% ($\chi^2/N_{\mathrm{dof}} = 8.3/7$). The slope of this fit is $0.28\% \pm 0.01\%$.

The respective plots of the SD energy resolution are given in Fig. 9.7 and 9.8. $\Delta E_{\mathrm{SD}}/E_{\mathrm{SD}}$ decreases as a function of $E_{\mathrm{FD}}$. Above $10^{18.7}$ eV the slope[5] is approximately constant. The comparatively higher values for the resolution below $10^{18.7}$ eV should be mainly caused by an underestimation of $E_{\mathrm{SD}}$ that is caused by the cut on a constant $E_{\mathrm{FD}}$. $\Delta E_{\mathrm{SD}}/E_{\mathrm{SD}}$ decreases as a function of $R_{\mathrm{p}}$ as well above $R_{\mathrm{p}} \approx 12$ km. A similar structure can be found in Fig. 9.4. A straight line fit[6] supports the assumption of a rather constant slope above $R_{\mathrm{p}} \approx 12$ km.

The average FD energy resolution estimators of the entire detector without Loma Amarilla and of each individual eye are listed in Table 9.1, ranging from 8.5% to 9.5%. The estimated average FD energy resolution of the entire detector is $8.91\% \pm 0.09\%$ and the average SD energy resolution is $8.25\% \pm 0.08\%$.

Figures 9.9 and 9.10 illustrate the distribution of the particular energy resolutions on

---

[4]Fit result (straight line): $\chi^2/N_{\mathrm{dof}} = 23.1/8$, prob $\approx 0.3\%$

[5]Fit result (straight line): $\chi^2/N_{\mathrm{dof}} = 16.11/6$, prob $\approx 1\%$

[6]Fit result (straight line): $\chi^2/N_{\mathrm{dof}} = 6.7/5$, prob $\approx 24\%$
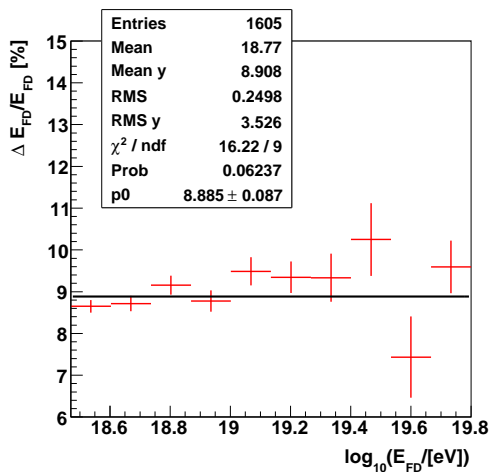
**Figure 9.5:** The average FD energy resolution $\langle \Delta E_{\mathrm{FD}}/E_{\mathrm{FD}} \rangle$ as a function of $E_{\mathrm{FD}}$ has been fitted with a constant. The fit result is given in the plot. Error bars: $\mathrm{RMS}/\sqrt{N}$.
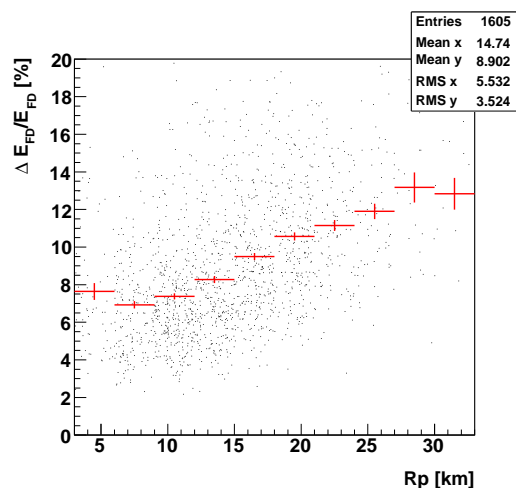


**Figure 9.6:** The distribution of the FD energy resolution $\Delta E_{\mathrm{FD}}/E_{\mathrm{FD}}$ as a function of $R_{\mathrm{p}}$ is superimposed with its profile. Error bars: $\mathrm{RMS}/\sqrt{N}$.
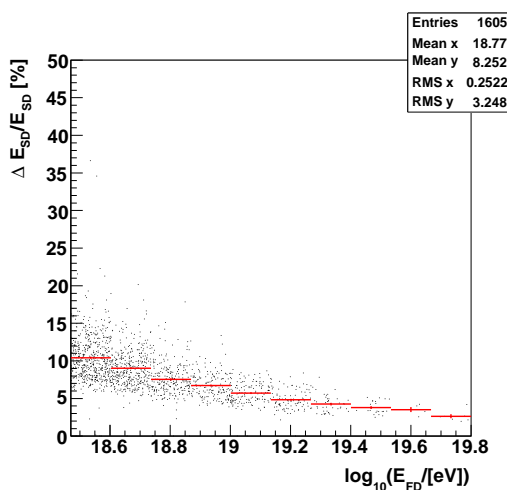


**Figure 9.7:** The distribution of the SD energy resolution $\Delta E_{\mathrm{SD}}/E_{\mathrm{SD}}$ as a function of $E_{\mathrm{FD}}$ is superimposed with its profile. Error bars: $\mathrm{RMS}/\sqrt{N}$.
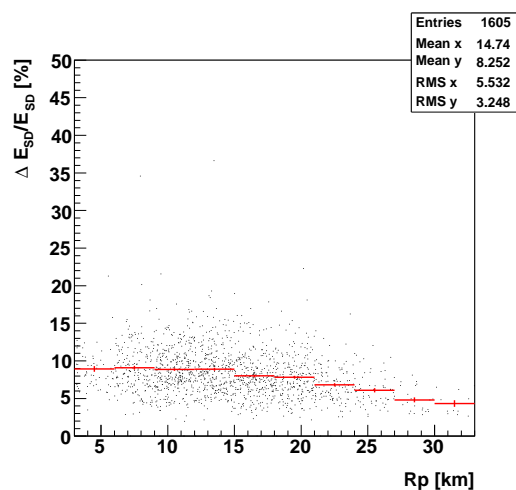


**Figure 9.8:** The distribution of the SD energy resolution $\Delta E_{\mathrm{SD}}/E_{\mathrm{SD}}$ as a function of $E_{\mathrm{FD}}$ is superimposed with its profile. Error bars: $\mathrm{RMS}/\sqrt{N}$.

|  | $\langle \Delta E_{\mathrm{FD}}/E_{\mathrm{FD}} \rangle$ [%] |
|---|---|
| Los Leones | $9.55 \pm 0.10$ |
| Los Morados | $8.73 \pm 0.09$ |
| Loma Amarilla | $8.55 \pm 0.09$ |
| Coihueco | $8.51 \pm 0.09$ |
| PAO | $8.91 \pm 0.09$ |

**Table 9.1:** Estimators of the average FD energy resolution $\langle \Delta E_{\mathrm{FD}}/E_{\mathrm{FD}} \rangle$ of the entire detector (PAO) excluding Loma Amarilla, and of the individual eyes. The error is approximated by 1% of the absolute value, according to the error of constant $p_0$ in Fig. 9.5.
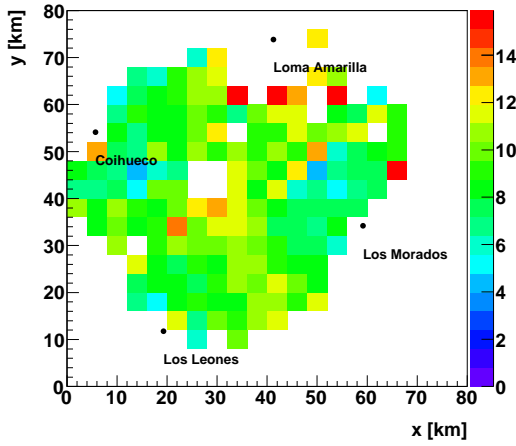


**Figure 9.9:** Distribution of the FD energy resolution on the detector array. The color gradient represents the average FD energy resolution $\langle \Delta E_{\mathrm{FD}}/E_{\mathrm{FD}} \rangle$ [%] per bin.
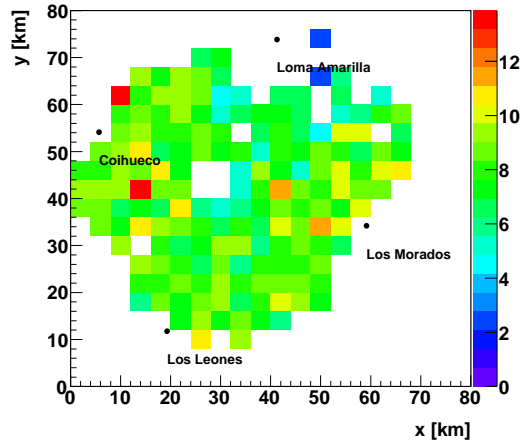
**Figure 9.10:** Distribution of the FD energy resolution on the detector array. The color gradient represents the average SD energy resolution $\langle \Delta E_{\mathrm{SD}}/E_{\mathrm{SD}} \rangle$ [%] per bin.

the detector array. The approximately reverse colors of Fig. 9.10 compared to Fig. 9.9 indicate a contrary distance-dependence of both resolutions. These plots show again an improvement of $\Delta E_{\mathrm{SD}}/E_{\mathrm{SD}}$ and a degrading of $\Delta E_{\mathrm{FD}}/E_{\mathrm{FD}}$ for increasing distances.

## 9.3 Approximation of an average energy resolution of both detector systems

Assuming the estimators of the FD and SD energy resolution to be approximately equal, an average energy resolution $\Delta \bar{E}/\bar{E}$ of the Hybrid detector can be derived. This estimator contains information on the average energy reconstruction accuracy within statistical and systematic reconstruction uncertainties. Analysing the logarithmic ratio of SD and FD

| | $\langle \Delta\bar{E}/\bar{E}\rangle$ [%] | $\sqrt{\langle(\Delta E_{\mathrm{FD}}/E_{\mathrm{FD}})^2 + (\Delta E_{\mathrm{SD}}/E_{\mathrm{SD}})^2\rangle}/\sqrt{2}$ [%] |
|---|---|---|
| Los Leones | $6.46 \pm 0.21$ | $9.14 \pm 0.12$ |
| Los Morados | $6.63 \pm 0.20$ | $8.80 \pm 0.10$ |
| Loma Amarilla | $6.84 \pm 0.31$ | $8.89 \pm 0.15$ |
| Coihueco | $5.68 \pm 0.17$ | $8.82 \pm 0.10$ |
| PAO | $6.29 \pm 0.11$ | $8.91 \pm 0.06$ |

**Table 9.2:** Particular average energy resolutions of two different approaches.

energy, $\Delta\bar{E}/\bar{E}$ approximately equals the RMS of the logarithmic ratio, divided by $\sqrt{2}$:

$$\Delta\left(\log_{10}\left(\frac{E_{\mathrm{SD}}}{E_{\mathrm{FD}}}\right)\right) = \mathrm{RMS}\left(\log_{10}\left(\frac{E_{\mathrm{SD}}}{E_{\mathrm{FD}}}\right)\right) \tag{9.1}$$

$$\Delta\left(\log_{10}\left(\frac{E_{\mathrm{SD}}}{E_{\mathrm{FD}}}\right)\right) = \sqrt{\left(\frac{\Delta E_{\mathrm{FD}}}{E_{\mathrm{FD}}}\right)^2 + \left(\frac{\Delta E_{\mathrm{SD}}}{E_{\mathrm{SD}}}\right)^2} \tag{9.2}$$

Using Eq. 9.1 and 9.2 and assuming $\Delta E_{\mathrm{FD}}/E_{\mathrm{FD}} = \Delta E_{\mathrm{SD}}/E_{\mathrm{SD}} = \Delta\bar{E}/\bar{E}$, we find:

$$\frac{\Delta\bar{E}}{\bar{E}} \approx \mathrm{RMS}\left(\log_{10}\left(\frac{E_{\mathrm{SD}}}{E_{\mathrm{FD}}}\right)\right) \cdot \frac{1}{\sqrt{2}} \tag{9.3}$$

The estimator[7] of this method, $\Delta\bar{E}/\bar{E}$, is compared to the estimator [8] of the particular energy resolutions, $\sqrt{(\Delta E_{\mathrm{FD}}/E_{\mathrm{FD}})^2 + (\Delta E_{\mathrm{SD}}/E_{\mathrm{SD}})^2}/\sqrt{2}$. The results of both approaches regarding the average resolution of the entire detector and individual eyes are listed in Table 9.2. They are not in agreement within their uncertainties. The average energy resolution, based on the assumption of an equal FD and SD energy resolution, is underestimated by approximately 30% compared to the result taking into account the particular energy resolutions.

The average energy resolution has been plotted as a function of $E_{\mathrm{FD}}$ and $R_{\mathrm{p}}$ (red markers), superimposed with the respective results using the particular resolutions (blue markers). The estimators have again been extracted from the one-dimensional distributions related to the particular approach, but this time within certain energy- and distance-intervals (Fig. B.14 - B.17). The resulting plots are given in Fig. 9.13 and 9.14. Obviously the different approaches are not in agreement within the uncertainties, neither regarding the absolute values nor the shape of the functions.

---

[7]This estimator and its error are taken from the RMS of the related distribution (Fig. 9.11) and its error respectively, divided by $\sqrt{2}$.

[8]This estimator and its error are taken from the mean of the related distribution (Fig. 9.12) and its error respectively, divided by $\sqrt{2}$.
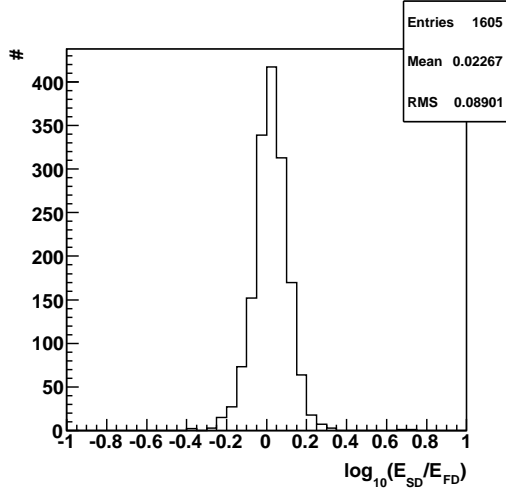
**Figure 9.11:** Distribution of the logarithmic energy ratio, $\log_{10}(E_{SD}/E_{FD})$, of the full selected dataset.
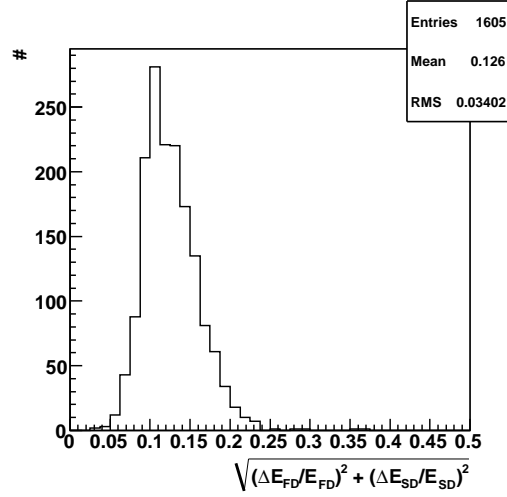


**Figure 9.12:** Distribution of the geometric mean of the particular energy resolutions (Eq. 9.3) of the full selected dataset.
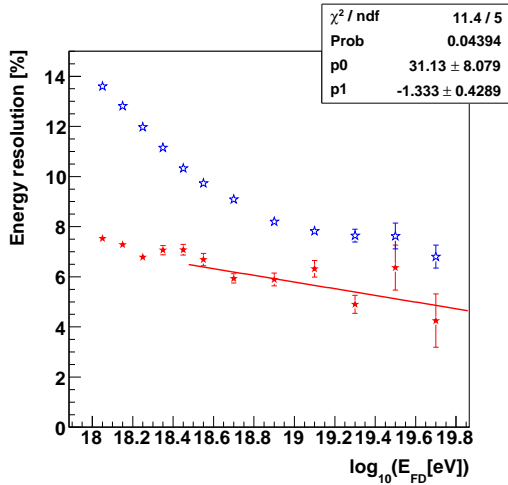


**Figure 9.13:** The average energy resolution $\Delta \bar{E}/\bar{E}$ as a function of the FD energy $E_{FD}$ (red markers) is superimposed with the respective results using the particular resolutions (blue markers). A straight line fit has been applied to the average energy resolution above $3 \cdot 10^{18}$ eV.
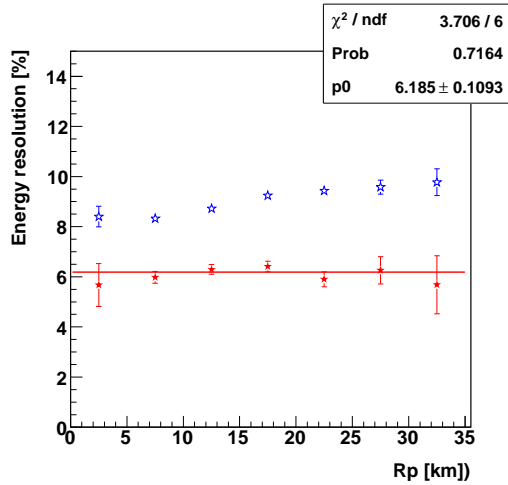


**Figure 9.14:** The average energy resolution $\Delta \bar{E}/\bar{E}$ as a function of the closest distance $R_p$ between shower axis and eye (red markers) is superimposed with the respective results using the particular resolutions (blue markers). A fit with a constant has been applied to the average energy resolution.
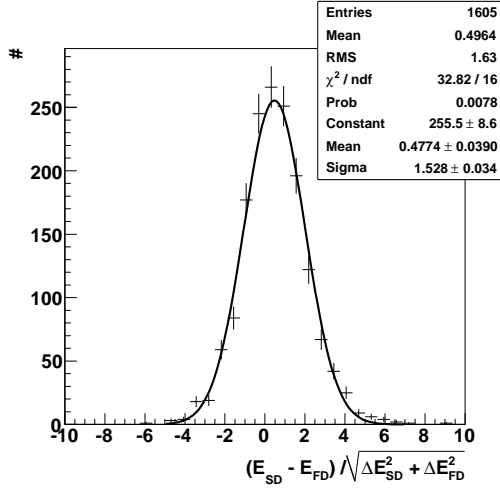
**Figure 9.15:** Pull plot of the energy error estimation, fitted with a Gaussian function. Error bars: $\sqrt{N}$.
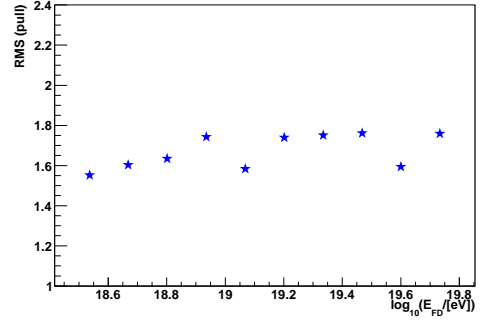


**Figure 9.16:** RMS of $P$ as a function of $E_{\mathrm{FD}}$.

## 9.4 Evaluation of the calculation of the FD and SD energy reconstruction uncertainties

In order to evaluate the energy error estimation, the distribution of ratio $P$ of the estimated SD and FD energy errors and the difference between SD and FD energy has been plotted event by event:

$$P \doteq \frac{E_{\mathrm{SD}} - E_{\mathrm{FD}}}{\sqrt{(\Delta E_{\mathrm{FD}})^2 + (\Delta E_{\mathrm{SD}})^2}} \tag{9.4}$$

The resulting plot is called *pull-plot*. It contains two essential quantities: The mean of the distribution and its spread. In case of a consistent error estimation the 68% quantile $P_{68}$ of the distribution and, in case of a Gaussian distribution, the $\sigma$ of the fit are expected to be in agreement with one. A consistent energy calibration together with a consistent error estimation requires a mean that is in agreement with zero. If $P_{68}$ or $\sigma$ are significantly smaller than one, this would indicate an overestimation of at least one error and greater than one an underestimation respectively. A significant shift of the mean would indicate an overestimation and overestimation of at least one energy. The pull-plot for the full selected dataset is given in Fig. 9.15.
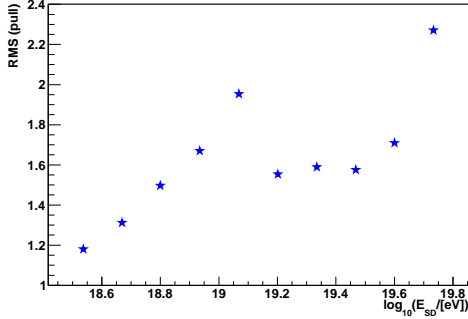
**Figure 9.17:** RMS of $P$ as a function of $E_{\mathrm{SD}}$.
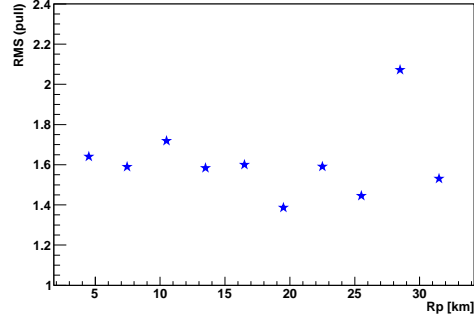


**Figure 9.18:** RMS of $P$ as a function of $R_{\mathrm{p}}$.

The distribution has been fitted with a Gaussian function:

$$f(x) = \frac{1}{\sigma \cdot \sqrt{2\pi}} \cdot \exp\left(-\frac{1}{2}\left(\frac{x - \mu^2}{\sigma}\right)\right) \tag{9.5}$$

where $\mu$ is the mean of the distribution. The fit results yield a probability of 0.8%, which does not clearly support the assumption of a Gaussian distribution, but the fit probability represents only a lower limit on the true probability (for details about the evaluation of fits with low $N_{\mathrm{dof}}$ see Chapter 6). However, taking the fit as a valid rough approximation of the distribution, the mean of the fit is $0.477 \pm 0.039$, deviating from zero by about 12 standard deviations. This indicates either a slight overestimation of $E_{\mathrm{SD}}$ or a slight underestimation of $E_{\mathrm{FD}}$, which supports the result of Chapter 9. The absolute value is weighted by the geometric mean of the errors. Thus this result might as well indicate an underestimation of at least one errors. The $\sigma$ of the fit is $1.528 \pm 0.034$, yielding a deviation of about 15 standard deviations from one. A similar result within the uncertainties is obtained using an estimator[9] of the spread based on the 68% quantile of the distribution of the absolute value of $P$, yielding $P_{68} \approx 1.563 \pm 0.016$. As the mean of the distribution and the fit are in agreement within the uncertainties as well, the fit seems to describe the distribution sufficiently. Both results indicate an underestimation of at least one error.
The FD energy error estimation of Los Leones and Coihueco has been analysed in [64] using the pull-method check with stereo events. This analysis was based on rather low statistics of 19 stereo events detected by both eyes, independent of simulations. The result yields a consistent error estimation of $E_{\mathrm{FD}}$ within the uncertainties. Assuming a consistent error estimation regarding Los Morados as well, the result of the present analysis might consequently indicate an underestimation of $\Delta E_{\mathrm{SD}}$.
This analysis has been redone for individual eyes (see Fig. B.18 in the appendix). The resulting mean and $\sigma$ of the pull-plot are in agreement within the uncertainties, supporting the assumption of a consistent estimation of $\Delta E_{\mathrm{FD}}$.

---

[9]The error of this estimator has been approximated by 1%.

Moreover, the dependence of the spread of the $P$-distribution on the $E_{\mathrm{FD}}$, $E_{\mathrm{SD}}$ and on $R_{\mathrm{p}}$ has been analysed. The spread has been estimated by $\mathrm{RMS}(P)$. The related plots are given in Fig. 9.16 - 9.18. As no error bars have been calculated, the interpretation of those plots cannot be significant. It is a qualitative description of the particular dependences. The plot in Fig. 9.16 shows $\mathrm{RMS}(P)$ as a function of $E_{\mathrm{FD}}$. As up to about $10^{19}$ eV the statistics are comparatively high (i.e. Fig. 9.1), the shape in this energy range should yield comparatively low uncertainties. Thus the shape might be interpreted as a slight increase of the spread of $P$. Above $10^{19}$ eV the shape might indicate a constant spread. The plot in Fig. 9.17 shows $\mathrm{RMS}(P)$ as a function of $E_{\mathrm{SD}}$. Up to about $10^{19.1}$ eV the shape of the graph indicates an increase of the spread which seems to be much stronger than for $E_{\mathrm{FD}}$. Above $10^{19.1}$ eV the shape might be in agreement with a less increasing spread. Figure 9.18 shows $\mathrm{RMS}(P)$ as a function of $R_{\mathrm{p}}$. The shape of the graph might indicate a slight distance dependence.

Those findings could be an indication for an underestimation of one of the energy errors at minimum. The magnitude of this underestimation seems to depend mostly on $E_{\mathrm{SD}}$. A possible dependence on $R_{\mathrm{p}}$ appears to be less strong. A strong dependence on $E_{\mathrm{SD}}$ together with weak dependence on $R_{\mathrm{p}}$ and thus on atmospheric influence may be a sign for a rather consistent estimation of $\Delta E_{\mathrm{FD}}$ and an underestimation $\Delta E_{\mathrm{SD}}$. As a consequence of the SD energy calibration a slight dependence of $\Delta E_{SD}$ on $E_{FD}$ is inherited, which is in agreement with the results.

## 9.5 Summary and outlook

The dependence of the energies and the energy resolutions of FD and SD on different parameters have been analysed successfully. The estimations of the FD and SD energy resolution yield $\Delta E_{\mathrm{FD}}/E_{\mathrm{FD}} = 8.91\% \pm 0.09\%$ and $\Delta E_{\mathrm{SD}}/E_{\mathrm{SD}} = 8.25\% \pm 0.08\%$. In [63] the FD energy scale uncertainty originating from various sources has been calculated. The resulting total uncertainty is about 22%. The particular average FD energy uncertainty due to the Hybrid reconstruction method is said to be approximately 10%. The present analysis is not in good agreement with this value, but this may be a consequence of using different datasets. In [59] the average uncertainty $\Delta E_{\mathrm{FD}}$ resulting from the Hybrid reconstruction is said to be approximately 9%, based on a similar dataset. This result is in agreement with the result of the present analysis.

Comparing the dependence of $\Delta E_{\mathrm{FD}}/E_{\mathrm{FD}}$ and $\Delta E_{\mathrm{SD}}/E_{\mathrm{SD}}$ on the FD energy and the distance, both resolutions show a contrary behaviour. The FD energy resolution degrades as a function of distance and is constant as a function of FD energy. The SD energy resolution improves as a function of distance and as a function of FD energy, as well. Due to different absolute values and different dependences of $\Delta E_{\mathrm{FD}}/E_{\mathrm{FD}}$ and $\Delta E_{\mathrm{SD}}/E_{\mathrm{SD}}$, the approximation of equal energy resolutions in order to estimate an average resolution $\Delta \bar{E}/\bar{E}$ is not justified.

The energy error estimation has been evaluated using the pull-method check. Analysing

the mean and the estimated spread $P_{68}$ (or $\sigma$ in case of a Gaussian distribution) of the essential quantity $P = (E_{\mathrm{SD}} - E_{\mathrm{FD}}) / \sqrt{(\Delta E_{\mathrm{FD}})^2 + (\Delta E_{\mathrm{SD}})^2}$, the consistence of the error-estimation and the energy calibration can be checked. The mean of the pull-plot yields $0.477 \pm 0.039$, deviating from zero by about 12 standard deviations. This result indicates an overestimation of $E_{\mathrm{SD}}$ or an underestimation of $E_{\mathrm{FD}}$, which is in agreement with the results of Chapter 8. The spread of the pull-plot is estimated by $P_{68} \approx 1.563 \pm 0.016$, deviating from one by about 15 standard deviations. Assuming a correct FD error estimation according to [64], this result might indicate an underestimation of $\Delta E_{\mathrm{SD}}$. This analysis has been redone for individual eyes (see Fig. B.18 in the appendix). The resulting mean and $\sigma$ of the pull-plot are in agreement within the uncertainties, supporting the assumption of a consistent estimation of $\Delta E_{\mathrm{FD}}$.

The analysis of the energy and distance dependence of the spread of $P$ could be as well an indication for an underestimation of $\Delta E_{\mathrm{SD}}$ and an approximately consistent estimation of $\Delta E_{\mathrm{FD}}$. All results of this analysis are in agreement with this interpretation. But, of course, this interpretation is of qualitative nature as no error bars have been given.

It would be helpful to analyse the estimation of the FD energy reconstruction uncertainty based on multi-eye events a second time, as the detector is finished and as there is a sufficient amount of Golden Hybrid Stereo data. The method would be an analysis of pull-plots with the quantity $P_{1,2}^{\mathrm{FD,stereo}} = (E_{\mathrm{FD},1} - E_{\mathrm{FD},2})/\sqrt{(\Delta E_{\mathrm{FD},1})^2 + (\Delta E_{\mathrm{FD},2})^2}$ for each pair of eyes.

# Chapter 10

# Summary

In the course of this thesis three issues have been analysed, based on measured Golden Hybrid data, following the order of the reconstruction chain: The reconstruction accuracy of the shower axis, the variation of the SD energy calibration with time and the energy resolution within statistical and systematic reconstruction uncertainties. Those issues are essential for the understanding of the detector as the reconstruction accuracy precedes any physical analysis based on measured data.

An essential data-subset to derive FD- and Hybrid-related resolutions of measured data are stereo events. A small subset of Golden Hybrid Stereo events from January 1st, 2004 until April 28th, 2009, selected with basic, high quality, Stereo- and Golden Hybrid-related cuts, were analysed to estimate the reconstruction accuracy of the shower axis. The angular resolution of the reconstructed shower direction was successfully estimated by the 68% quantile of the distribution of the space angle between two Hybrid-reconstructed shower axes (Hybrid angular resolution $\sigma_{\mathrm{H}}$) and between SD- and Hybrid-reconstructed shower axis (Overall angular resolution $\sigma_{\mathrm{SD,H}}$). $\sigma_{\mathrm{H}}$ and $\sigma_{\mathrm{SD,H}}$ were found to be rather constant with time. An estimation of the SD angular resolution $\sigma_{\mathrm{SD}}$ was performed using the following essential relation:

$$\sigma_{\mathrm{SD}} = \sqrt{\sigma_{\mathrm{SD,H}}^2 - \sigma_{\mathrm{H}}^2}$$

The mean SD and Hybrid angular resolution were estimated, yielding $\sigma_{\mathrm{H}} = 0.99°$ and $\sigma_{\mathrm{SD}} = 0.49°$. Excluding Loma Amarilla because of a preliminary PMT calibration and pixel-miscablings and thus a restricted geometry reconstruction accuracy, the resulting $\sigma_{\mathrm{H}} = 0.88°$ is in agreement with results of simulation-based estimations. Moreover, $\sigma_{\mathrm{SD,H}}$, $\sigma_{\mathrm{H}}$ and $\sigma_{\mathrm{SD}}$ were successfully analysed as a function of $E_{\mathrm{FD}}$. The average reconstruction accuracy of the shower axis intersection point with the ground (shower core) yielded on average 0.4 km.

Comparisons of the angular resolutions and of the reconstruction accuracy of the shower core of individual eyes showed that care has to be taken regarding the reconstruction accuracy of the shower axis using Loma Amarilla and maybe Coihueco as well.

Based on a dataset from January 1st, 2004 until March 31st, 2009, using the cuts of the ICRC09 calibration with a 5T5 cut instead of 6T5, the variation of the SD energy

calibration with time was analysed. Within the observed energy range of 5 EeV up to 40 EeV, the analysis of the energy ratio $E_{\mathrm{SD}}/E_{\mathrm{FD}}$ and of the measured differential flux as a function of $E_{\mathrm{FD}}$ and $E_{\mathrm{SD}}$ within different time periods might indicate an underestimation of $E_{FD}$ and $E_{SD}$. The energy ratio is shifted by about 10% within the last period from September 1st, 2007 to March 31st, 2009. The observed magnitude of a shift of the fluxes as a function of $E_{\mathrm{FD}}$ and $E_{\mathrm{SD}}$ is in agreement with the expected one according to the ratio shift and the assumption of a flux describing the power law spectrum $E^{-3.2}$. An underestimation of $E_{\mathrm{FD}}$ could possibly be explained by aging photomultipliers. Actually regular calibrations of FD and SD should compensate the aging effect of the photomultipliers.

A respective analysis of the differential flux as a function of the SD energy estimator $S^{38}$ could eventually answer the question if an underestimation of $E_{\mathrm{SD}}$ is completely inherited from $E_{\mathrm{FD}}$ by the calibration or if $S^{38}$ decreases with time as well.

Based on a similar dataset that has been selected requiring $E_{\mathrm{FD}} > 3 \cdot 10^{18}$ eV instead of the ellipse cut, the average resolution of $E_{\mathrm{FD}}$ and $E_{\mathrm{SD}}$ within statistical and systematic reconstruction uncertainties has been analysed, yielding $E_{\mathrm{FD}} = 8.91\% \pm 0.09\%$ and $E_{\mathrm{SD}} = 8.25\% \pm 0.08\%$. Using a pull-method check to evaluate the estimation of $\Delta E_{\mathrm{FD}}$ and $\Delta E_{\mathrm{SD}}$, the essential quantity $P = (E_{\mathrm{SD}} - E_{\mathrm{FD}})/\sqrt{(\Delta E_{\mathrm{FD}})^2 + (\Delta E_{\mathrm{SD}})^2}$ was analysed. Several indications were found for a rather consistent estimation of $\Delta E_{\mathrm{FD}}$ and for an underestimation of $\Delta E_{\mathrm{SD}}$. Both the analysis of the pull-plot and its spread within certain intervals of $E_{\mathrm{FD}}$, $E_{\mathrm{SD}}$ and $R_{\mathrm{p}}$ yield consistent results. The analysis of the dependences of the spread should be redone calculating error bars and applying fits for a sophisticated interpretation.

Golden Hybrid data provide a large set of cross checks and comparisons between Hybrid and SD data that help in the understanding of the detectors. In this thesis analyses of the reconstruction accuracy of the shower axis and the energy and of the SD energy calibration were successfully performed.

# Acknowledgements

# Appendix A

# Shower Direction
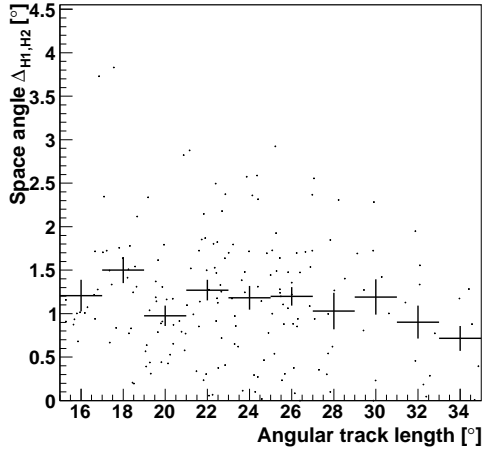
**Figure A.1:** Space angle $\Delta_{\text{H1,H2}}$ between two Hybrid-axes as a function of angular tracklength. Error bars: RMS/$\sqrt{N}$.
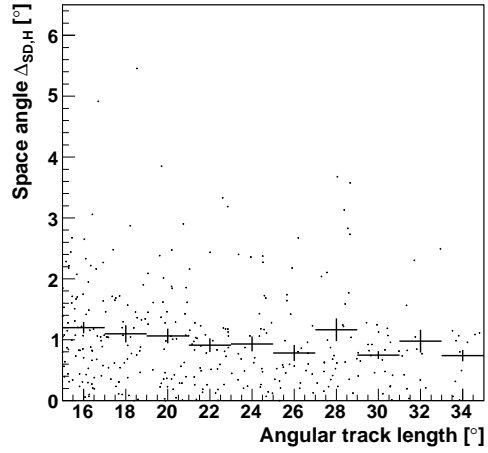


**Figure A.2:** Space angle $\Delta_{\text{SD,H}}$ between SD- and Hybrid-axis as a function of angular tracklength. Error bars: RMS/$\sqrt{N}$.
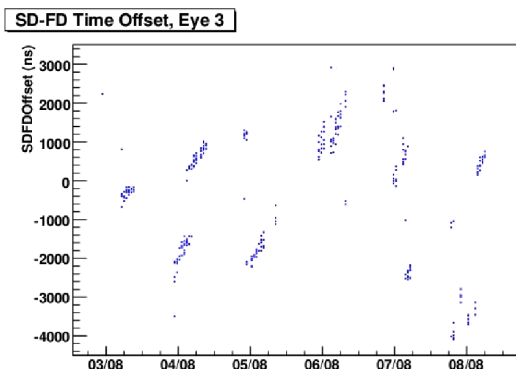


**Figure A.3:** GPS time offset between SD and FD, Loma Amarilla. (Plot: P. Younk)
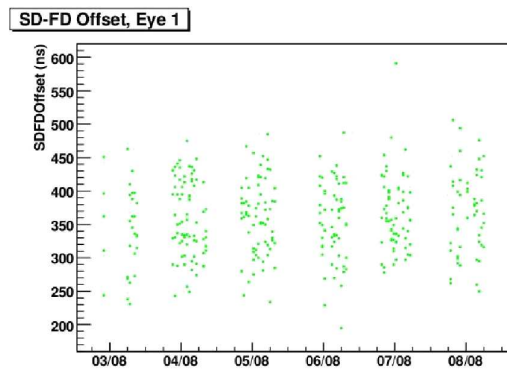


**Figure A.4:** GPS time offset between SD and FD, Los Leones. (Plot: P. Younk)
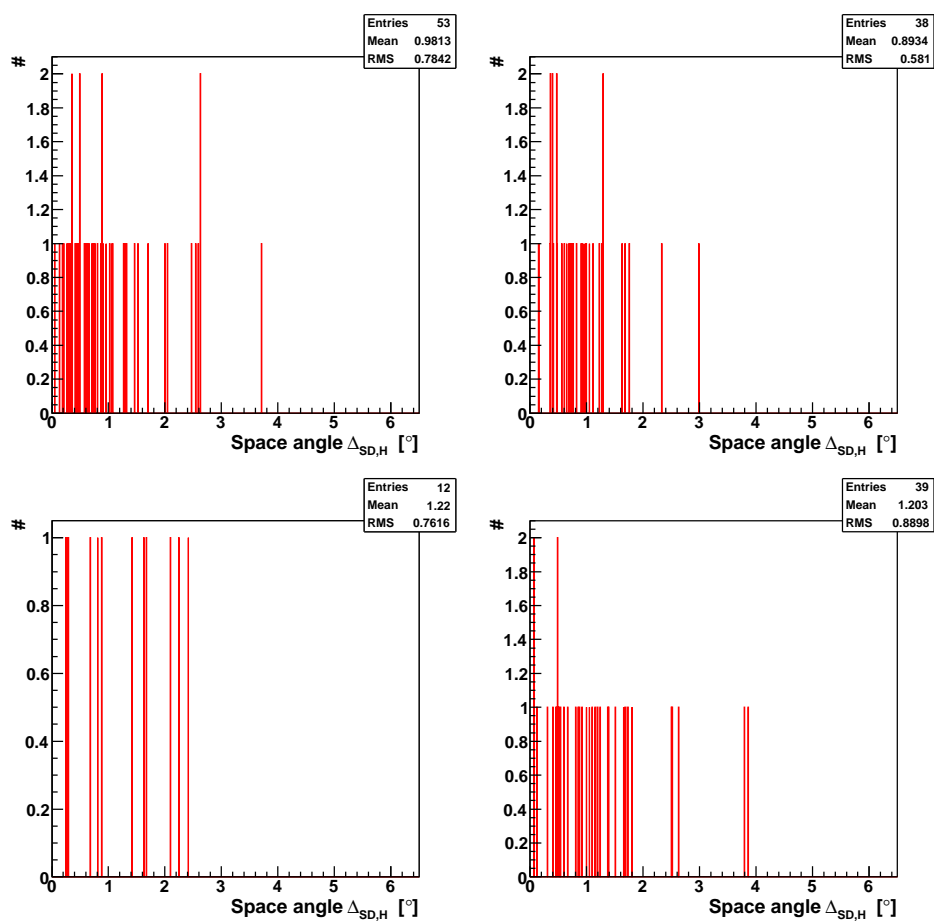
**Figure A.5:** Distributions of the space angle $\Delta_{\mathrm{SD,H}}$ of each individual eye in the first period. Related quantities are listed in Table 7.2. Upper left: Los Leones, upper right: Los Morados, lower left: Loma Amarilla, lower right: Coihueco.
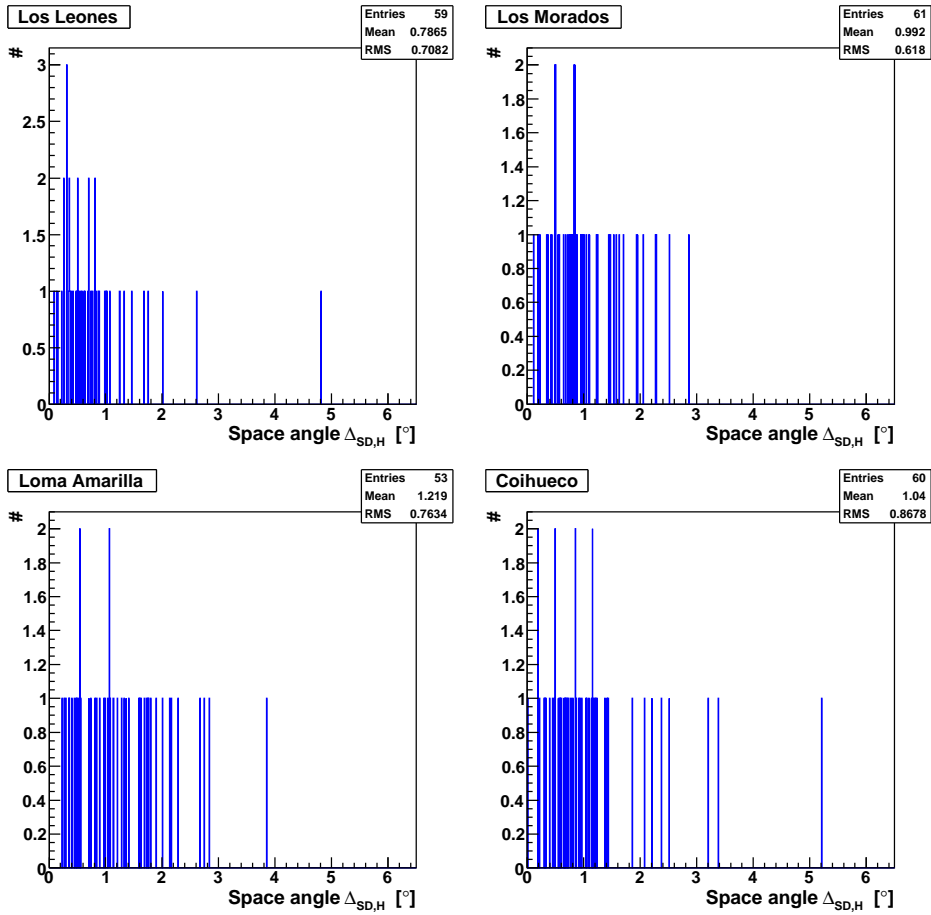
**Figure A.6:** Distributions of the space angle $\Delta_{\text{SD,H}}$ of each individual eye in the second period, excluding Loma Amarilla bad period. Related quantities are listed in Table 7.2.
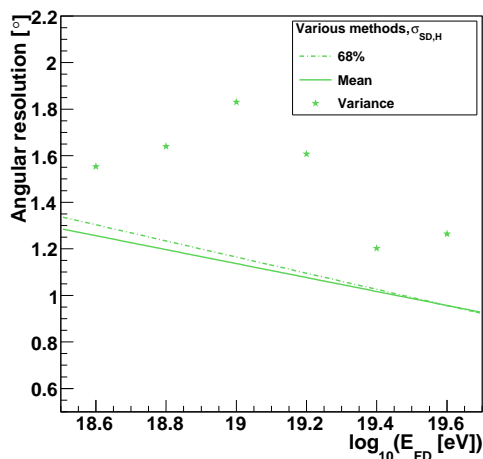
**Figure A.7:** Comparison of the $\sigma_{\mathrm{SD,H}}$ estimators related to the 68% quantile method, the mean method and the variance method. Fit result of the underlying mean profile fit: $\chi^2 = 1.31$, $N_{\mathrm{dof}} = 4$.
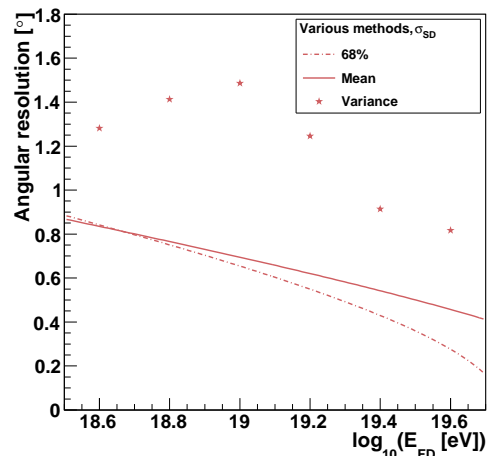


**Figure A.8:** Comparison of the $\sigma_{\mathrm{SD}}$ estimators related to the 68% quantile method, the mean method and the variance method.
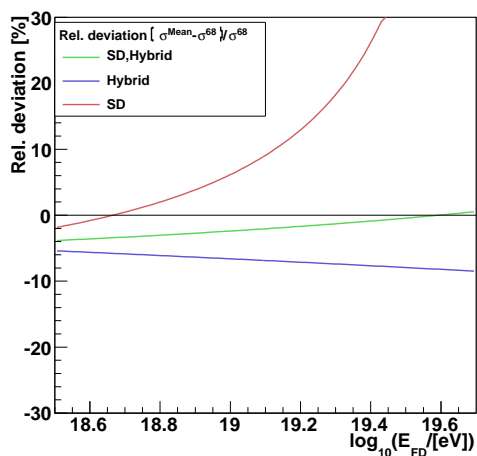


**Figure A.9:** Relative deviation of the estimators of the mean method compared to the 68% quantile method.
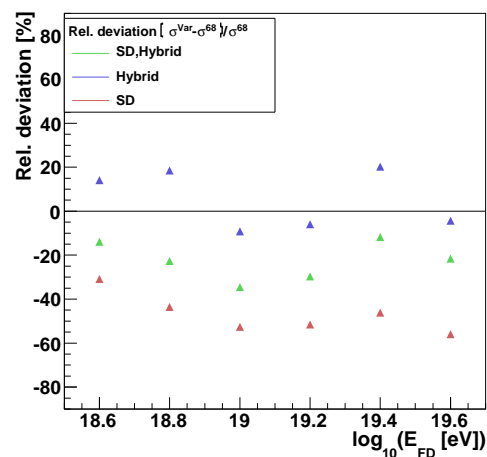


**Figure A.10:** Relative deviation of the estimators of the variance method compared to the 68% quantile method.
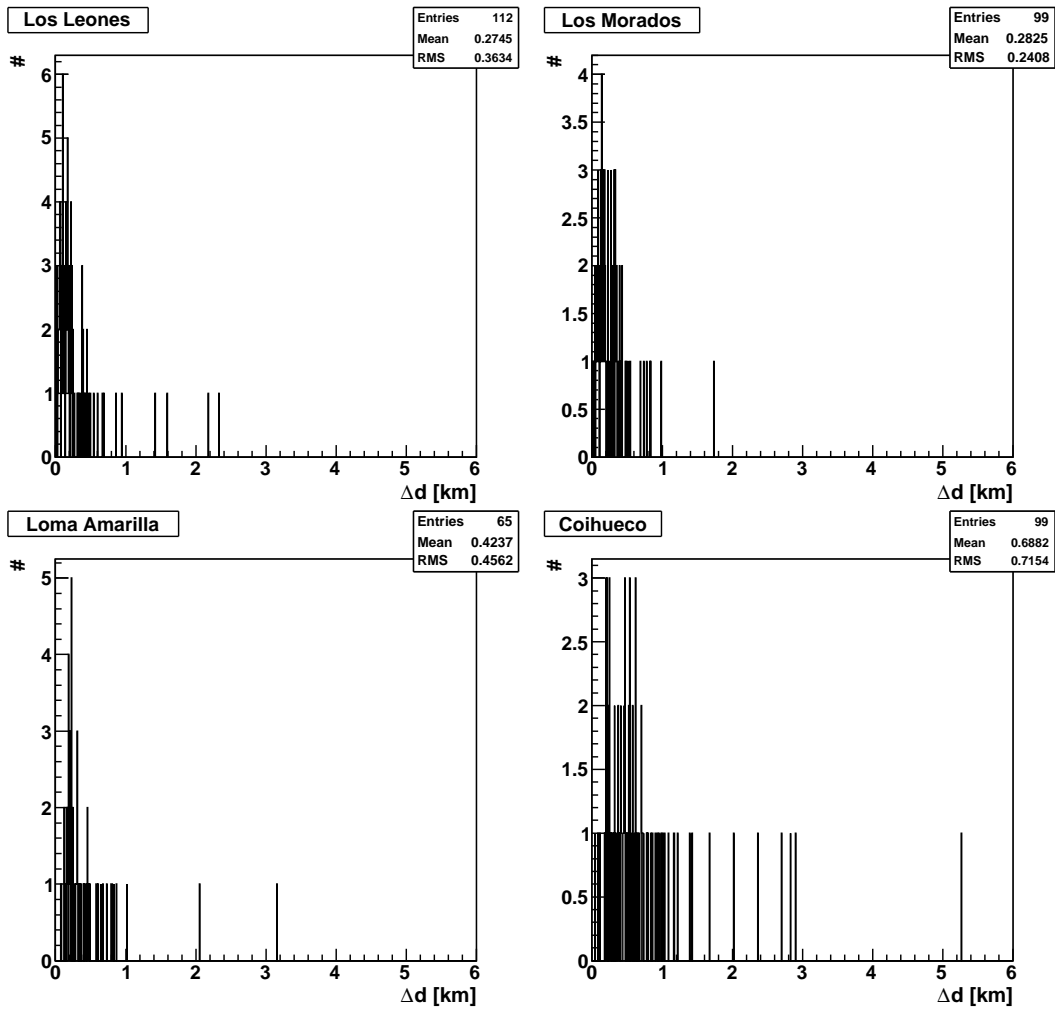
**Figure A.11:** Distributions of the distance $\Delta d$ between Hybrid- and SD-reconstructed shower core of each individual eye.

# Appendix B

# Energy Calibration and Resolution
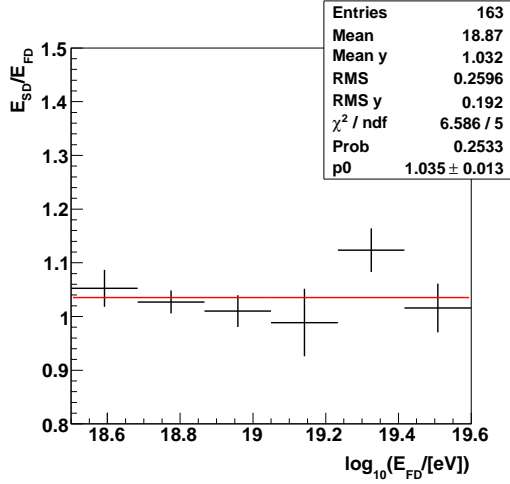
**Figure B.1:** Mean energy ratio $E_{SD}/E_{FD}$ as a function of $E_{FD}$, for period 1 (6T5 cut, *ICRC09* calibration). The profile has been fitted with a constant (red line). Error bars: RMS/$\sqrt{N}$.
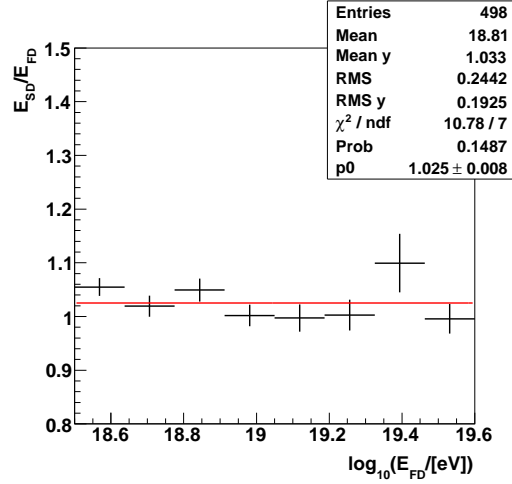


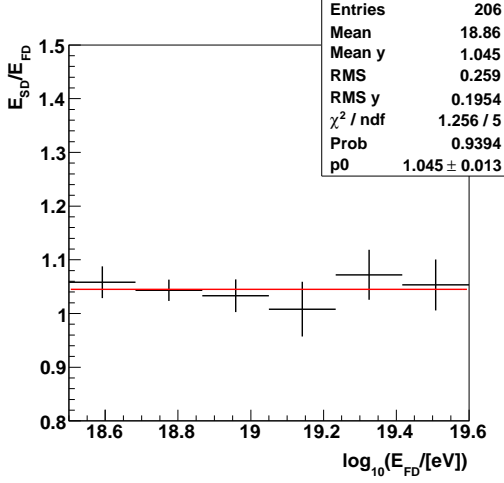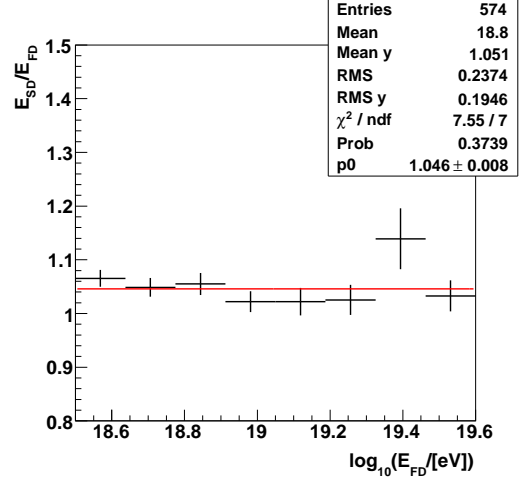**Figure B.2:** Mean energy ratio $E_{SD}/E_{FD}$ as a function of $E_{FD}$, for period 2 (6T5 cut, *ICRC09* calibration). The profile has been fitted with a constant (red line). Error bars: RMS/$\sqrt{N}$.
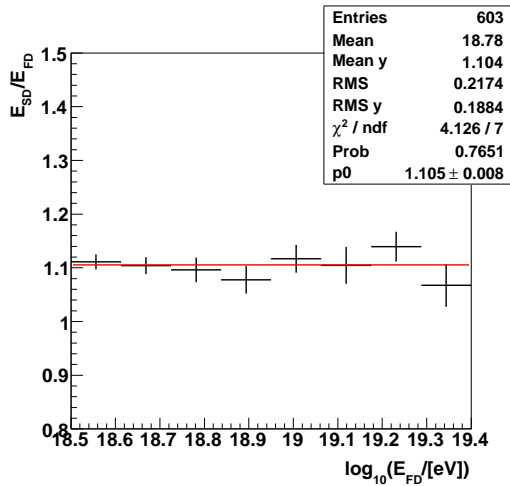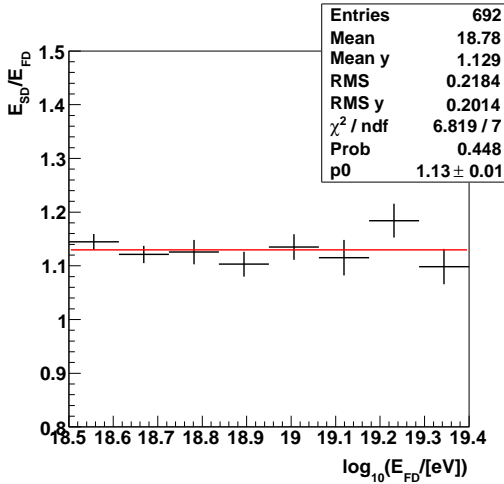


**Figure B.3:** Mean energy ratio $E_{SD}/E_{FD}$ as a function of $E_{FD}$, for period 3 (6T5 cut, *ICRC09* calibration). The profile has been fitted with a constant (red line). Error bars: RMS/$\sqrt{N}$.
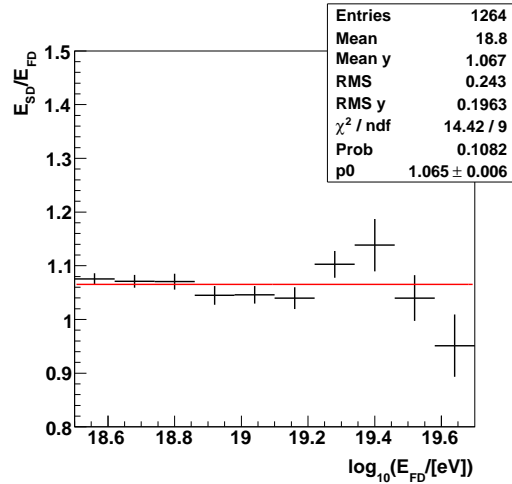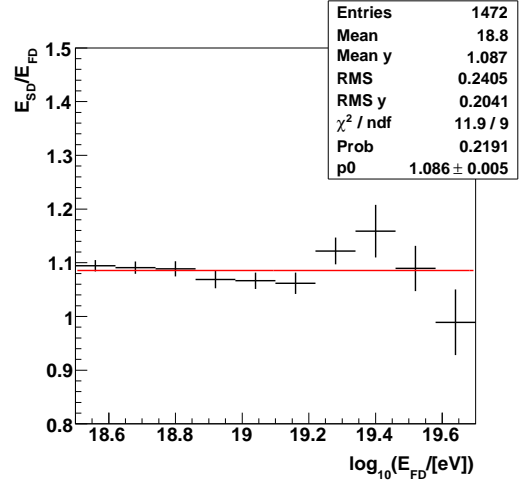


**Figure B.4:** Mean energy ratio $E_{SD}/E_{FD}$ as a function of $E_{FD}$, for the full period (6T5 cut, *ICRC09* calibration). The profile has been fitted with a constant (red line). Error bars: RMS/$\sqrt{N}$.

**Figure B.5:** Mean energy ratio $E_{\mathrm{SD}}/E_{\mathrm{FD}}$ as a function of $E_{\mathrm{FD}}$, for period 1 (5T5 cut, *PRL08* calibration). The profile has been fitted with a constant (red line). Error bars: RMS/$\sqrt{N}$.
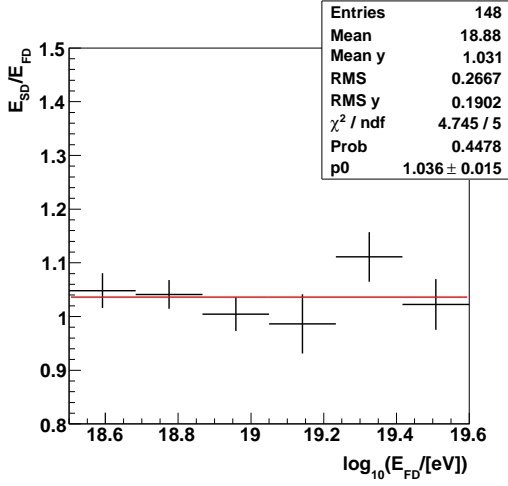


**Figure B.6:** Mean energy ratio $E_{\mathrm{SD}}/E_{\mathrm{FD}}$ as a function of $E_{\mathrm{FD}}$, for period 2 (5T5 cut, *PRL08* calibration). The profile has been fitted with a constant (red line). Error bars: RMS/$\sqrt{N}$.



**Figure B.7:** Mean energy ratio $E_{\mathrm{SD}}/E_{\mathrm{FD}}$ as a function of $E_{\mathrm{FD}}$, for period 3 (5T5 cut, *PRL08* calibration). The profile has been fitted with a constant (red line). Error bars: RMS/$\sqrt{N}$.



**Figure B.8:** Mean energy ratio $E_{\mathrm{SD}}/E_{\mathrm{FD}}$ as a function of $E_{\mathrm{FD}}$, for the full period (5T5 cut, *PRL08* calibration). The profile has been fitted with a constant (red line). Error bars: RMS/$\sqrt{N}$.

**Figure B.9:** Mean energy ratio $E_{\rm SD}/E_{\rm FD}$ as a function of $E_{\rm FD}$, for period 1 (*ICRC09* original dataset). The profile has been fitted with a constant (red line). Error bars: RMS/$\sqrt{N}$.
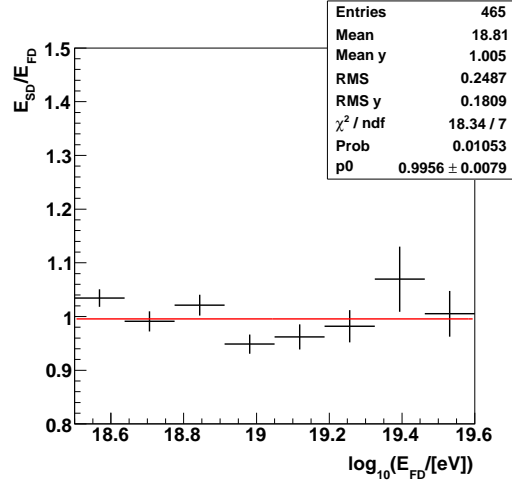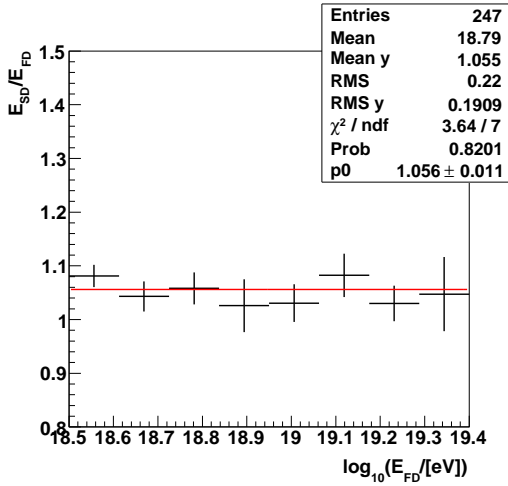


**Figure B.10:** Mean energy ratio $E_{\rm SD}/E_{\rm FD}$ as a function of $E_{\rm FD}$, for period 2 (*ICRC09* original dataset). The profile has been fitted with a constant (red line). Error bars: RMS/$\sqrt{N}$.
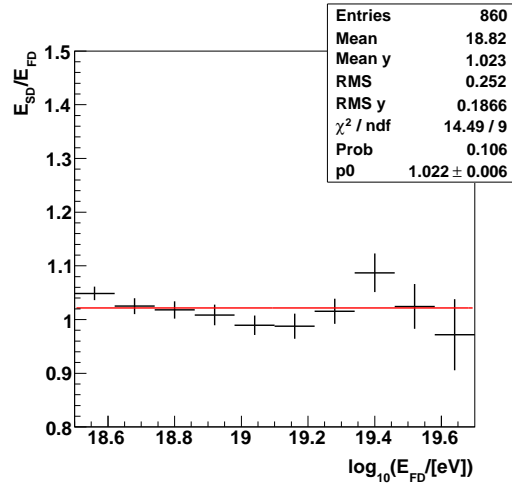


**Figure B.11:** Mean energy ratio $E_{\rm SD}/E_{\rm FD}$ as a function of $E_{\rm FD}$, for period 3 (*ICRC09* original dataset). The profile has been fitted with a constant (red line). Error bars: RMS/$\sqrt{N}$.



**Figure B.12:** Mean energy ratio $E_{\rm SD}/E_{\rm FD}$ as a function of $E_{\rm FD}$, for the full period (*ICRC09* original dataset). The profile has been fitted with a constant (red line). Error bars: RMS/$\sqrt{N}$.
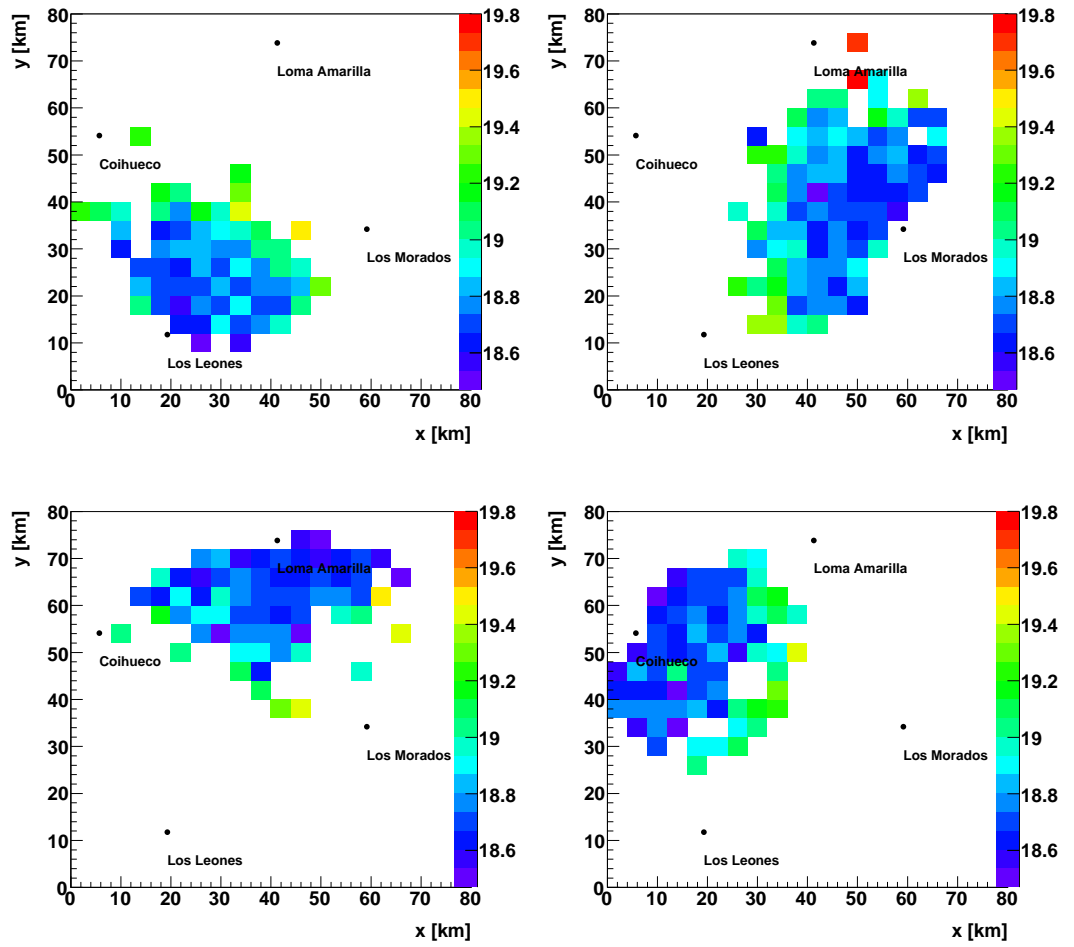
**Figure B.13:** Distributions of the FD energy on the detector array for each individual eye. The color gradient represents the logarithm of the average FD energy, $\log_{10}\left(\langle E_{\mathrm{FD}}\rangle/[\mathrm{eV}]\right)$.
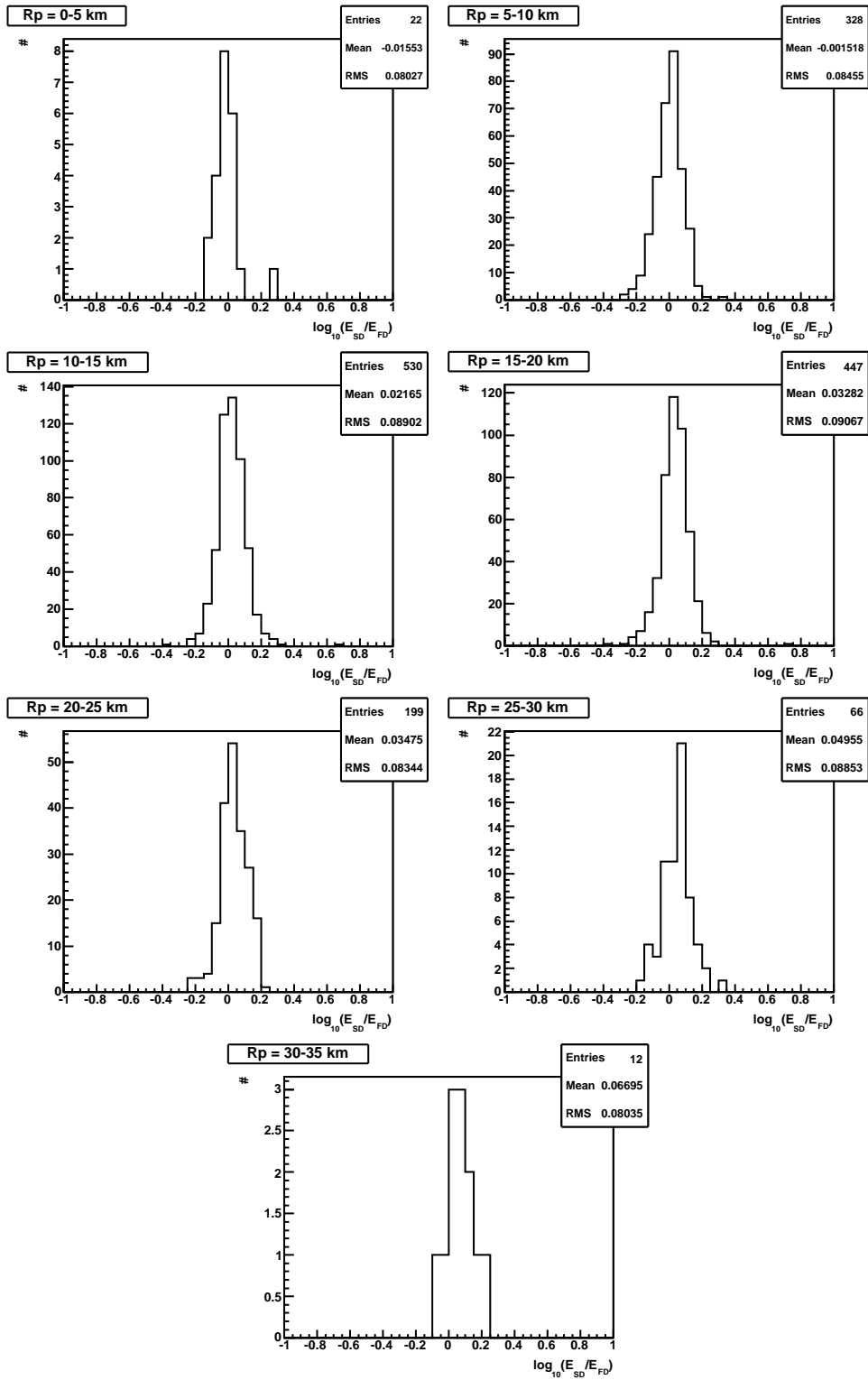
**Figure B.14:** Distribution of the logarithmic energy ratio, $\log_{10}(E_{SD}/E_{FD})$, within certain distance-intervals.

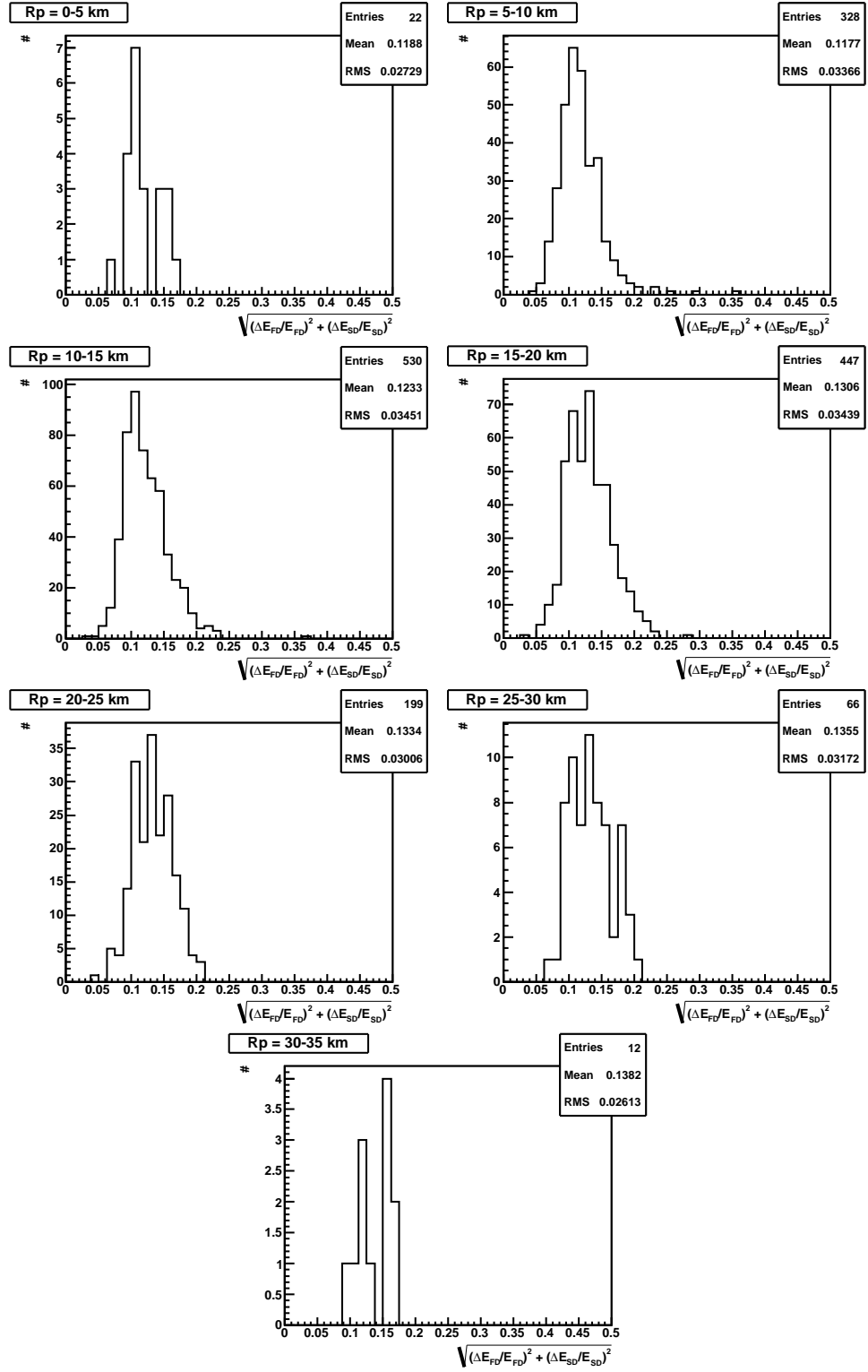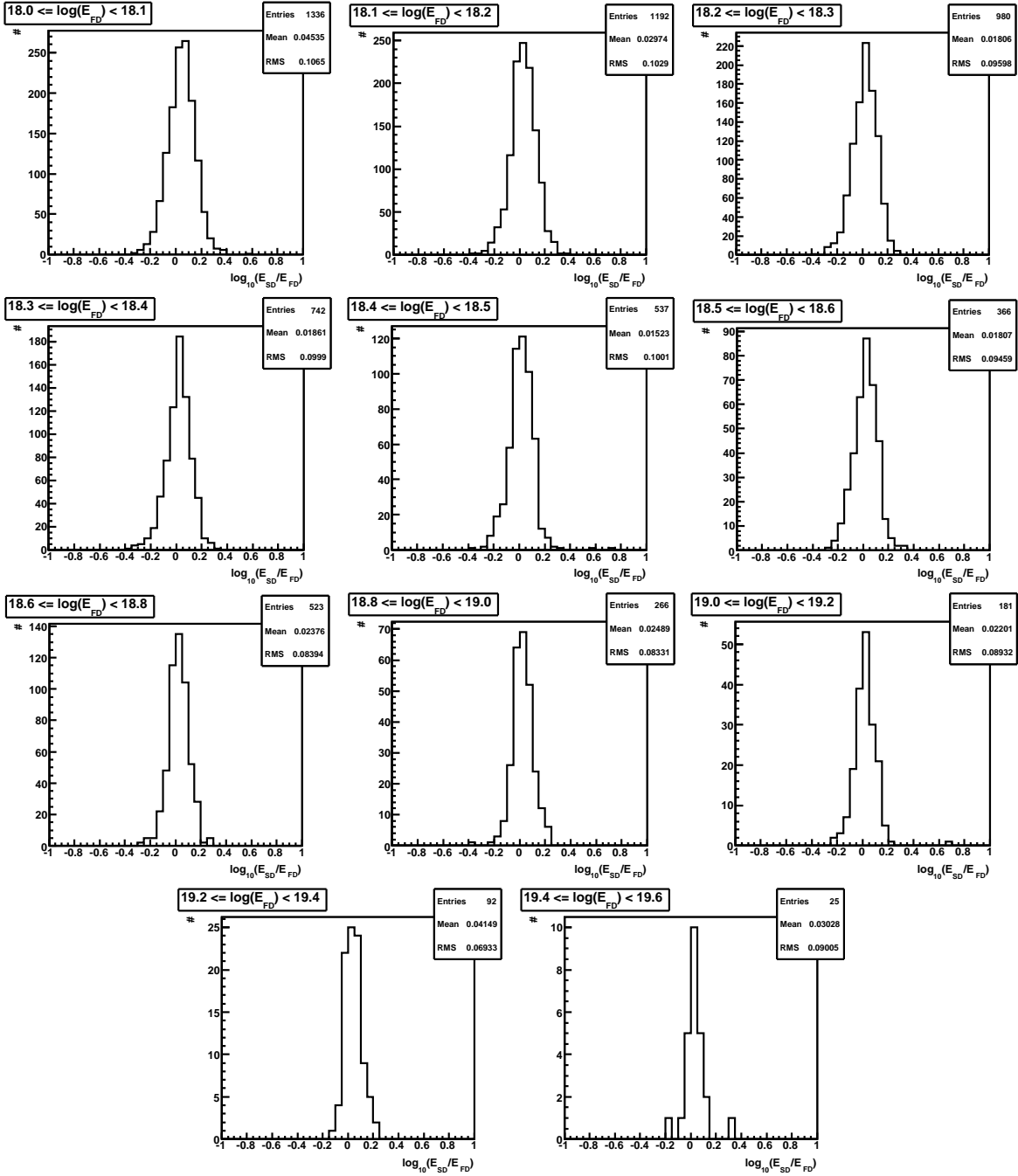**Figure B.15:** Distribution of the geometric mean of the particular energy resolutions, $\sqrt{(\Delta E_{\mathrm{FD}}/E_{\mathrm{FD}})^2 + (\Delta E_{\mathrm{SD}}/E_{\mathrm{SD}})^2}$, within certain distance-intervals.

**Figure B.16:** Distribution of the logarithmic energy ratio, $\log_{10}(E_{\mathrm{SD}}/E_{\mathrm{FD}})$, within certain energy-intervals.
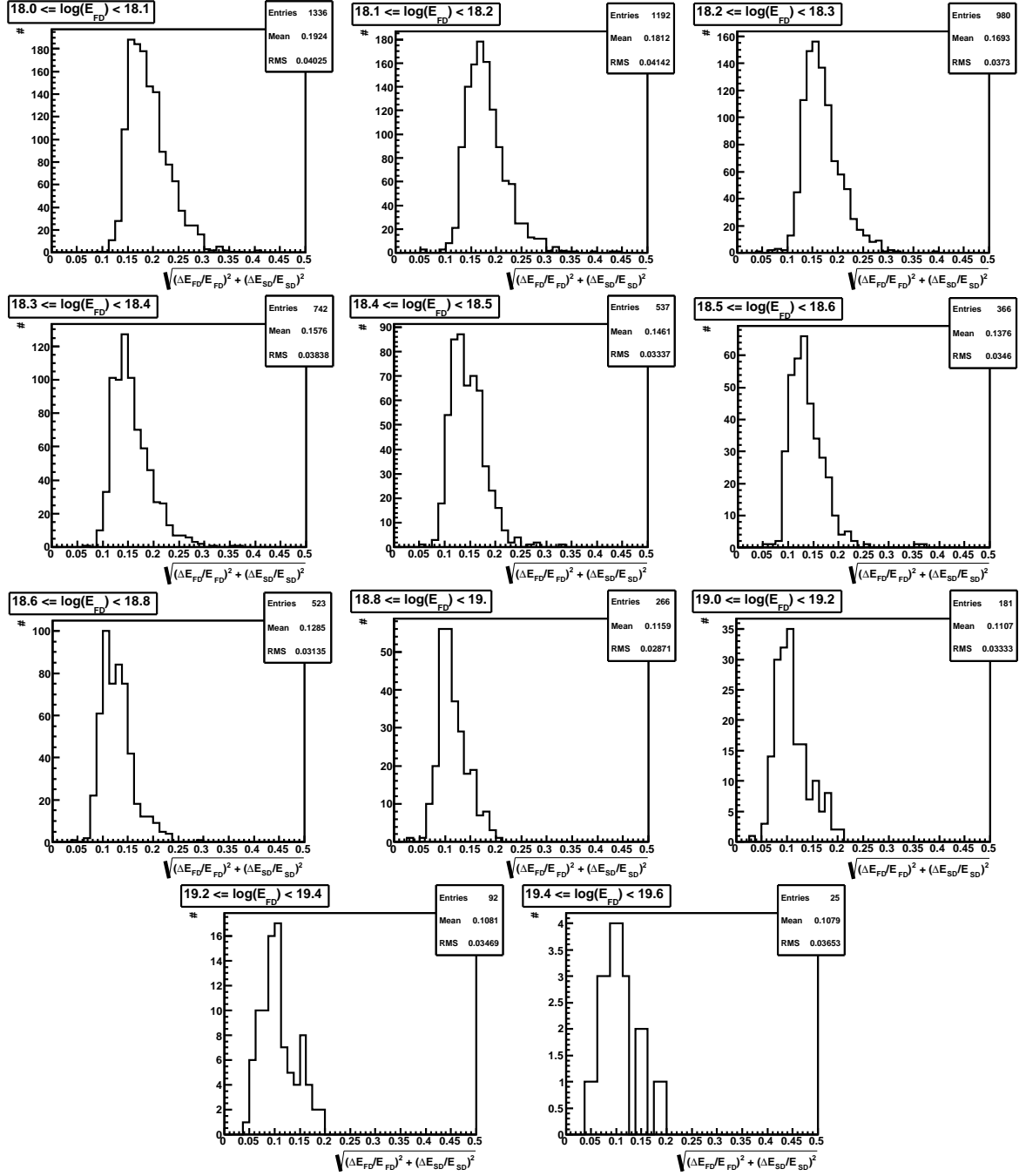
**Figure B.17:** Distribution of the geometric mean of the particular energy resolutions, $\sqrt{(\Delta E_{\mathrm{FD}}/E_{\mathrm{FD}})^2 + (\Delta E_{\mathrm{SD}}/E_{\mathrm{SD}})^2}$, within certain energy-intervals.
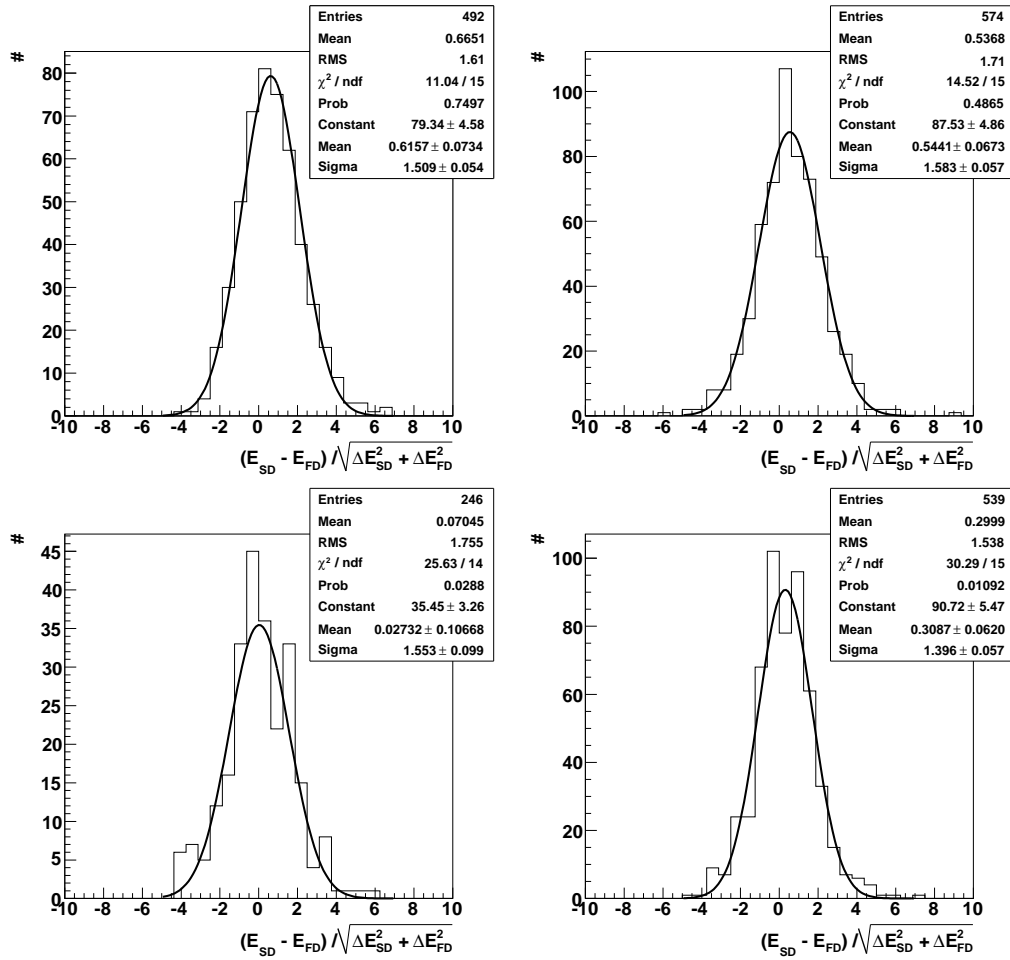
**Figure B.18:** Pull plots of the individual eyes regarding the energy error estimation, fitted with a Gaussian function. The fit results are given on each plot. Upper left: Los Leones, upper right: Los Morados, lower left: Loma Amarilla, lower right: Coihueco.

# Bibliography

[1] K.-H. Kampert, "Ultra High-Energy Cosmic Ray Observations", *J. Phys. Conf. Ser.* 120 (2008) 062002; arXiv:0801.1986v1 [astro-ph]

[2] J. Blümer, R. Engel and J.R. Hörandel, "Cosmic Rays from the Knee to the Highest Energies", *Prog. Part. Nucl. Phys.* (2009); arXiv:0904.0725v [astro-ph.HE]

[3] The Auger Collaboration, "The Pierre Auger Observatory Design Report", 2nd edition, (1997).

[4] T. Wulf, *Phys. Zeitschr.* 10, 997 (1909).

[5] V.F. Hess, "Über Beobachtungen der durchdringenden Strahlung bei sieben Ballonfahrten", *Phys. Zeitschr.* 13, 1084-1091 (1912).

[6] W. Kohlhörster, *Phys. Zeitschr.* 26, 654 (1925).

[7] W. Bothe and W. Kohlhörster, *Zeitschr. f. Physik* 56, 751 (1929).

[8] J. Clay, *Amsterdam Proc.* 33, p. 711 (1930).

[9] W. Kohlhörster *et al.*, *Naturw.* 26, 576 (1938).

[10] P. Auger *et al.*, *Comptes rendus* 206, 1721 (1938).

[11] M. Schein, W.P. Jesse and E.O. Wollan, *Phys. Rev.* 59, 615 (1941).

[12] H.L. Bradt and B. Peters, *Phys. Rev.* 74, 1828-1037 (1948).

[13] S. Swordy, *J. Phys.*, Conf. Ser. 60, 143-146 (2007).

[14] A.W. Strong, I.V. Moskalenko, V.S. Ptuskin, *Ann. Rev. Nucl. Part. Sci.* 57, 285-327 (2007); arXiv:astro-ph/0701517v1

[15] J. Linsley, *Phys. Rev. Lett.* 10, 146-148 (1963).

[16] C.J. Bell *et al.*, *J. Phys.* A 12, 990 (1974).

[17] D.M. Edge, A.C. Evans and H.J. Garmston, *J. Phys.* A 6, 1612 (1973).

[18] B.N. Afanasiev *et al.*, *Proc. Workshop on Techn. for the Study of EHECR, Tokyo, Japan*, ed. M. Nagano, 35 (2003).

[19] N. Chiba *et al.* (AGASA Collaboration), *Nucl. Instrum. Meth.* A311, 338-349 (1992).

[20] R.M. Baltrusaitis *et al.* (Fly's Eye Collaboration), *Nucl. Instrum. Meth.* A240, 410-428 (1985).

[21] G. Kulikov and G. Khristiansen, *JETP* 35, 635 (1958).

[22] J. Linsley, *Proc. 8th ICRC, Jaipur, India*, 77-99 (1963).

[23] K. Greisen, *Phys. Rev. Lett.* 16, 748 (1966) and G.T. Zatsepin and V.A. Kuz'min, *Sov. Phys. JETP Lett.* 4 (Engl. transl.), 78 (1966).

[24] J. Abraham *et al.* (Pierre Auger Collaboration), *Phys. Rev. Lett.* 101, 061101 (2008).

[25] M.P. Véron-Cetty, P. Véron, *Astron. Astrophys.* 22, 425 (1984).

[26] J. Alvarez-Muniz, R. Engel, T.K. Gaisser, J.A. Ortiz and T. Stanev, "Hybrid simulations of extensive air showers", *Phys. Rev.* D66, 033011 (2002)

[27] T.K. Gaisser and A.M. Hillas, "Reliability of the Method of Constant Intensity Cuts for Reconstructing the Average Development of Vertical Showers,", *Proc. 15th ICRC, Plovdiv, Bulgaria*, 353 (1977).

[28] W. Heitler, "The Quantum Theory of Radiation", *Oxford University Press*, (1944).

[29] J. Linsley, "Structure of Large Air Showers at Depth 834 G cm2 Applications", *Proc. 15th ICRC, Plovdiv, Bulgaria*, 89 (1977).

[30] J. Bellido *et al.* (Pierre Auger Collaboration), "Mass Composition Studies of the Highest Energy Cosmic Rays", *Proc. XXth Rencontres de Blois "Challenges in Particle Astrophysics"*, (2008); arXiv:0901.3389v1 [astro-ph.HE]

[31] A.A. Penzias, R.W. Wilson, *Astrophys.* J.142, 419-421 (1965).

[32] D. Harari, S. Mollerach and E. Roulet, *JCAP* 012, 611 (2006); arXiv:astro-ph/0609294v2

[33] M. Nagano *et al.*, *Astropart. Phys.* 22, 235 (2004).

[34] F. Kakimoto *et al.*, *Nucl. Instr. Meth.* A372, 527 (1996).

[35] M. Risse and P. Homola, "Search for ultra-high energy photons using air showers", *Mod. Phys. Lett.* A 22, 749 (2007); arXiv:astro-ph/0702632v1

[36] M. Unger *et al.* (Pierre Auger Collaboration), "Study of the Cosmic Ray Composition above 0.4 EeV using the Longitudinal Profiles of Showers observed at the Pierre Auger Observatory", *Proc. 30th ICRC, Merida, Mexico*, (2007); arXiv:0706.1495v1 [astro-ph]

[37] J. Abraham *et al.* (Pierre Auger Collaboration), *Astropart. Phys. 31*, 399-406 (2009); arXiv:0903.1127v2 [astro-ph.HE]

[38] J. Hörandel, "Models of the knee in the energy spectrum of comic rays", *Astroparticle Physics* 21, 241265 (2004).

[39] J. Blümer and K.-H. Kampert, "Die Suche nach den Quellen der kosmischen Strahlung", *Phys. Blätter* 3, 39 (2000).

[40] T. Stanev, "High Energy Cosmic Rays", 2nd ed. (2004), Springer-Verlag.

[41] J. Abraham *et al.* (Pierre Auger Collaboration), "Correlation of the highest-energy cosmic rays with the positions of nearby active galactic nuclei", *Astropart. Phys.* 29, 188-204 (2008); arXiv:0712.2843 [astro-ph]

[42] J. Abraham *et al.* (Pierre Auger Collaboration), "Operations of and Future Plans for the Pierre Auger Observatory", *Proc. 31st ICRC, Łódź, Poland*, (2009); arXiv:0906.2354v2 [astro-ph.IM]

[43] I. Allekotte *et al.*, "The Surface Detector System of the Pierre Auger Observatory". *Nucl. Instr. and Meth.* A 586, 409420 (2008); arXiv:0712.2832v1 [astro-ph]

[44] P. Billoir, O. Blanch Bigas and C. Bonifazi, "Can we recover events with a less strict T5?"; GAP-2008-163.

[45] J. Abraham *et al.* (Pierre Auger Collaboration), "The Fluorescence Detector of the Pierre Auger Observatory". *Subm. to Nucl. Instr. and Meth.* A (2009); arXiv:0907.4282v1 [astro-ph.IM]

[46] R. Cester *et al.*, "Atmospheric aerosol monitoring at the Pierre Auger Observatory". *29th ICRC, Pune, India* (2005).

[47] D. Veberič and M. Roth, "SD Reconstruction; Offline Reference Manual"; GAP-2005-035.

[48] I.C. Mariş, "Measurement of the Ultra High Energy Cosmic Ray Flux using Data of the Pierre Auger Observatory" (Dissertation); GAP-2008-026.

[49] K. Kamata and J. Nishimura, *Prog. Theoret. Phys. Suppl.* 6, 93 (1958);
K. Greisen, *Progress in Cosmic Ray Physics, Amsterdam, North-Holland* vol. 3 (1956).

[50] D. Kümpel, K.-H. Kampert, M. Risse, "Geometry reconstruction of fluorescence detectors revisited". *Astropart. Phys.* 30, 167-174 (2008); arXiv:0806.4523v2 [astro-ph]

[51] J. Hersil *et al.*, *Phys. Rev. Lett.* 6, 22 (1961).

[52] S. Argiro *et al.*, *Nucl. Inst. Meth.* A580, 1485-1496 (2007); arXiv:0707.1652v1 [astro-ph]

[53] S. Argiro *et al.* (Pierre Auger Collaboration), "The Offline Software Framework of the Pierre Auger Observatory"; arXiv:astro-ph/0601016 [astro-ph]

[54] I.C. Mariş, F. Schüssler, R. Ulrich and M. Unger, "Data Summary Trees and Shower Visualization for Reconstructed and Simulated Auger Events" (2006); based on GAP-2006-081.

[55] M. Settimo, L. Perrone and C. Bonifazi, "Hybrid angular resolution with Corsika showers and comparison to data" (2009); GAP-2009-063.

[56] M. Grigat, Th. Hebecker, "Angular Reconstruction Systematics" (2009); GAP-2009-094.

[57] Discussions within the angular resolution working group, available through the mailing list server.

[58] J. Abraham *et al.* (Pierre Auger Collaboration), "Astrophysical Sources of Cosmic Rays and Related Measurements with the Pierre Auger Observatory", *Proc. 31st ICRC, Łódź, Poland*, (2009); arXiv:0906.2357v2 [astro-ph.HE]

[59] C. Di Giulio *et al.* (Pierre Auger Collaboration), "Energy calibration of data recorded with the surface detectors of the Pierre Auger Observatory", *Proc. 31st ICRC, Lodz, Poland*, 14-17 (2009); arXiv:0906.2189v2 [astro-ph.HE]

[60] I.C. Mariş, J. Blümer, M. Roth, M. Unger and D. Verberič, "Reducing the influence of the threshold events on the surface detector energy calibration" (2007); GAP 2007-116.

[61] J. Abraham *et al.* (Pierre Auger Collaboration), "Observation of the suppression of the flux of cosmic rays above $4 \times 10^{19}$ eV", *Phys. Rev. Lett.* 101 (2008) 061101; arXiv:0806.4302v1 [astro-ph]

[62] R.J. Barlow, "Statistics - A Guide to the Use of Statistical Methods in the Physical Sciences", Wiley (1989);

[63] B. Dawson *et al.* (Pierre Auger Collaboration), "Hybrid Performance of the Pierre Auger Observatory", *Proc. 30th ICRC, Merida, Mexico*, (2007); arXiv:0906.2189v2 [astro-ph.HE]

[64] N. Nierstenhöfer, "Untersuchung systematischer Rekonstruktionsunsicherheiten der Fluoreszenzdetektoren des Pierre Auger Observatoriums anhand experimenteller Daten" (Diploma thesis).

Hiermit versichere ich, dass ich diese Arbeit selbstständig verfasst und keine anderen als die angegebenen Hilfsmittel und Quellen benutzt sowie Zitate kenntlich gemacht habe.

Wuppertal, den 15.12.2009

Nicole Krohm